ALMA MATER STUDIORUM - UNIVERSITÀ DI BOLOGNA

FACOLTÀ DI SCIENZE MATEMATICHE, FISICHE E NATURALI

DOTTORATO DI RICERCA
IN FISICA

Ciclo XXIII

Settore scientifico disciplinare di afferenza: FIS/04

Competition between evaporation and fragmentation in nuclear reactions at 15-20 AMeV beam energy

presentata da: Dott. Luca Morelli

Coordinatore Dottorato: **Prof. Fabio Ortolani**

Relatore: **Prof. Mauro Bruno**

Esame finale anno 2011

Contents

Chapter 1

Physics case

1.1 Heavy ions collisions

Heavy ions reactions are one of the most powerful way to study nuclear matter behaviour in extreme conditions of temperature and density. The heavy ions peculiarity is due to the fact that these reactions are the best way to produce nuclei with high excitation energy and angular momentum. In order to study the mechanisms of heavy ion reactions the main goal is to classify collisions according to some global features; allowing for the identification and the characterization of the source(s). The topology of each collision is, to a large extent, related both to the impact parameter of the collision and to a partial or total transformation of the available centre-of-mass kinetic energy of the relative motion between the two partners of the collisions into disordered motion (heat).

This dissipation process is governed by several important ingredients. One of them is the relative velocity between the initial partners of the reaction v_{AA}. The corresponding reduced relative wavelength associated with a nucleon-nucleon collision then reads

$$\lambda\!\!\!^{-} = \frac{\hbar}{m v_{AA}} \tag{1.1}$$

where m is the nucleon mass. According to equation 1.1, the following values (in the case of symmetrical systems) of $\lambda\!\!\!^{-}$ = 6.5, 2.1, 0.67, 0.24 fm are obtained for 1, 10,

100, 1000 AMeV beam energies, respectively. These values have to be compared with the mean nucleon-nucleon distance in a nucleus (typically 2 fm). If $\lambda\!\!\!^{-}$ exceeds this distance, a collective behaviour of nucleons during the collision is expected. In other words, mean field (one-body) effects overcome nucleon-nucleon collisions (two body) effects. The situation will be reversed if $\lambda\!\!\!^{-}$ is smaller than the mean nucleon-nucleon distance. According to this criterion, it turns out that mean field effects are expected to be dominant in the low-energy region (below 15 AMeV).

Furthermore, the different reaction mechanisms can be distinguished using the impact parameter b, i.e. the distance between the center of the ideal sphere corresponding to the target to the flight of the projectile, or the angular momentum ℓ correlated to this one. The impact parameter is the order parameter of any theoretical description of nuclear collisions, but it is not experimentally accessible. Estimations of b are obtained by measurable variables monotonically correlated with b. Referring to Fig. 1.1, one can identify these regions at low energy (E < 10 MeV/u) connected to different reaction mechanism:

- elastic scattering for $\ell > \ell_{gr}$, because the distance between projectile and target nucleus is to such that the nuclear force is completely negligible with respect to the Coulomb one;
- quasi-elastic scattering for $\ell_{DIC} < \ell < \ell_{gr}$ where the kinematics of the two nuclei is just slightly perturbed and only few nucleon transfer between projectile and target is possible;
- deep inelastic scattering (DIC) for $\ell_{crit} < \ell < \ell_{DIC}$, characterized by a strong interaction between the two nuclei with interchange of nucleons (from few nucleons transfer to highly dissipative processes);
- central collisions for $\ell < \ell_{crit}$, where the main process is the complete fusion with the creation of a Compound Nucleus (CN), defined as the complete thermalized

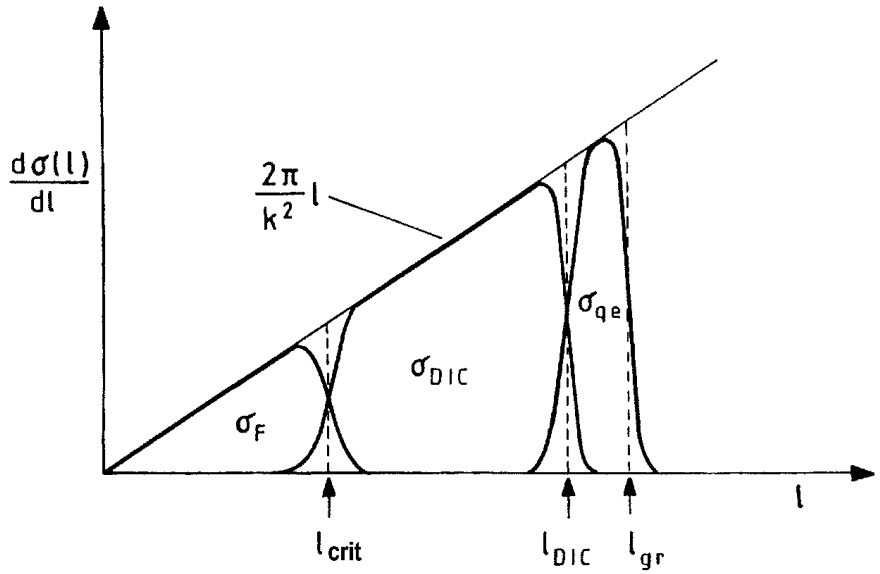

Figure 1.1: A schematic diagram of the partial wave decomposition of the reaction cross-section in low incident energy heavy-ion reactions: the abscissa refers to orbital angular momentum or to the impact parameter.

sum of the projectile and target nucleons without memory of the entrance reaction channel.

To create a CN a central collision with energy high enough to pass through Coulomb barrier is needed. In fact, the projectile and target are obviously charged with positive charge due to the presence of the protons, but if they arrive close enough, they can enter the range of the attractive nuclear strong forces. The process of merging the single nucleons from the two initial nuclei can be schematized like the mixing of two different gases with different temperatures inside a fixed volume.
Through subsequent nucleon-nucleon collisions, the nucleons from the projectile loose some energy giving it to the nucleons of the target, initially at zero energy. In this way the thermalization process start which means the equipartition of energy over all the nucleons, and a new system is formed, with mass and charge equal to the sum of the

two partners. On has a total dissipation of the initial available kinetic energy from the projectile into excitation energy, and consequently a non-zero temperature, for the whole system, assuming this as an equilibrated thermal system

1.1.1 Inelastic collision

In Heavy ions collision the elastic scattering is limited essentially to impact parameters which do no lead to a considerable overlap of projectile and target. For smaller impact parameters inelastic processes (excitation and transfer of nucleons) occur.
We refer as inelastic collisions to all the collisions where a certain amount of the initial kinetic energy is dissipated in internal degree of freedoms of the system, ranging from those in which a few nucleons are transferred from one ion to the other, with little loss of energy, to the so-called “strongly damped” or “deep inelastic” collisions in which the projectile lose a substantial fraction of its kinetic energy.
During the collision a composite system is formed, which preserves a di-nuclear feature: in the contact region a “window“ is formed between the two colliding nuclei. Through this window, more or less stretched, the energy dissipation takes place by nucleons exchange and angular momentum transfer.
The composite system does not reach complete statistical equilibrium, because there are a few degrees of freedom which relax very slowly, over times larger than or comparable with the contact time of the two fragments. These relaxation phenomena are connected with mass transfer, kinetic-energy loss and angular momentum dissipation. Afterward the system splits into two primary fragments, called Projectile and Target Like Fragments (PLF and TLF), or Quasi Projectile (QP) and Quasi Target (QT), which preserve memory of the entrance channel.

1.1.2 Complete and incomplete fusion

Central collisions are the key reactions which really probe matter in its extreme state since they correspond to the largest dissipated energies. In these conditions one has the largest compression because close collisions lead to a considerable overlap of the density distribution of the colliding nuclei. In these processes the interacting composite systems may break apart again preserving their di-nuclear feature, as we have seen in dissipative collisions, or form a fused system.

This latter phenomenon can be described as the result of a strong friction between the two participating nuclei which leads to a merging of all their nucleons. If the interaction time is long enough with respect to the thermalization time, i.e. when the impact parameter approaches zero, this dissipative process may eventually lead to the formation of a unique system which can reach thermodynamical equilibrium. In this way one can define a temperature of this equilibrated system. The reaction then proceed, according to Bohr's hypothesis [1], through the intermediate stage, known as Compound Nucleus which is formed by the absorption of the projectile by the target nucleus.

CN reactions between heavy ions are of particular interest because they provide the most efficient way of forming highly excited systems in high-spin states. Since many nucleons are involved, the total energy may be high but it is shared by all nucleons.

The CN is formed in an excited state and since the system is in equilibrium, it decays, after a time long compared with the transit time, by statistical processes, such as γ rays and/or particles emission (or eventually fission). The decay may be treated exploiting the nuclear thermodynamics, i.e. statistical models, which are essentially based on Bohr's CN picture. The particles emitted ("evaporated") by equilibrated system will accordingly have a distribution in energy that is typically of the order of the total energy of the system and independent of its mode of formation in the CN reference system one expects an isotropic angular distribution. The CN mass before any decay is the total initial mass of the system: this process is called complete fusion and dominates central collisions between heavy ions for projectile energies E$\approx$10 AMeV [2]. When the incident energy increases (E > 10 AMeV), the projectile and/or the target

may lose, in the early stage of the collision, nucleus or cluster of nucleons, emitted as light particles, which remove an appreciable part of the kinetic energy initially carried by the entire projectile. On a longer time scale the remnants of the two colliding nuclei fuse. Again a complete statistical equilibrium of the merging nucleons is achieved. In this process, commonly called incomplete fusion [2, 3], as a result, the mass of the "reduced" CN formed is less than the total mass of the system, the velocities of the evaporation residues and of the fission fragments are different from those of the fragments emitted subsequent to complete fusion. Moreover the "reduced" CN does not absorb the full linear momentum of projectile and target.

Later on we refer as compound nucleus to the system produced both in complete and incomplete fusion reactions since the properties of the system are very similar. With increasing projectile energy (E $\approx$ 20$\div$40 AMeV), incomplete fusion becomes preponderant with respect to complete fusion; the total fusion cross section diminishes progressively.

The way in which a CN is formed is a dynamical problem and it is connected with the problem of friction or viscosity, i.e. the transfer of energy from one degree of freedom (the relative motion) to the many degrees of freedom describing the compound nucleus.

We now consider the energy balance in nuclear fusion. The excitation energy U of the CN, at a given center-of-mass bombarding energy $E^{(CM)}$, can be written as:

$$U = E^{(CM)} + Q_{fu} = E^{(CM)} + (M_1 + M_2 - M_{1+2})c^2 \tag{1.2}$$

where Q_{fu} is the Q-value associated with the formation of the CN in its ground state and M_1, M_2 and M_{1+2} the mass of the projectile, target and CN respectively, at their ground state. This shows that CN formation represents the limit of a completely inelastic process, where the total relative kinetic energy in the incident channel is absorbed. Compound nucleus lifetimes can be deduced by statistical model calculations, which relate the lifetime of the CN to the effective number of open decay channels.

Typical lifetimes are of the order of 300 ÷ 3000 fm/c [1] for excitation energy around U~100MeV and are long with respect to thermalization times.

1.2 Decay mode

There are two big classes of nuclear excitations, depending on the type of states they lead to. The first class concerns excitations leading to specific states: this is typically the case of giant resonances which consist in collective modes of motion of the nucleus. In turn, these states may decay either in a specific way, following proper selection rules, or in a statistical way. In the second class of deexcitations, a large set of states become populated in a non-specific way. This is the situation typically encountered in hot nuclei, close to equilibrium (moderate excitation energies and little compression).

When an isolated state is populated, the reaction cross section have a typical resonant behaviour trend expressed by the Breit-Wigner formula [4]. Such situation concerns states at low excitation energy.

With the increase of the excitation energy the mean spacing between the nuclear levels is reduced and at the same time their width increases. This implies in the region of high excitation energy that many states of the compound nucleus are populated in the reaction, whose widths are superimposed, and a treatment based on the statistical physics is needed to describe the decay.

In particular the concept of level density ρ(E) becomes important. In this region, called continuum region, the statistical model (SM) allows to calculate the decay probabilities of the CN in each channel energetically accessible. In such contest the consistent treatment of the fusion-fission (FF) and fusion-evaporation (FE) decay channels can provide quantitative predictions of all relevant quantities of the decay products, such as the cross sections, the angular distributions and the energy spectra of the reaction products.

[1] $1\,fm/c = 3.3\dot{1}0^{-24}s$

The complete fusion cross section σ_{fus} can be obtained by measuring the fusion-evaporation σ_{FE} and fusion-fission σ_{FF} cross sections:

$$\sigma_{fus} = \sigma_{FE} + \sigma_{FF} \tag{1.3}$$

At low temperature as 1 or 2 MeV unexpected large values of σ_{FE} suggest that fission is a slow process, during which cooling, particularly via evaporation, may occur: evaporation and fission compete as dominant decay mode in the deexcitation of hot equilibrated systems.

The fragment emission or fission requires a description based not only on phase space considerations (as in evaporation theory) but also on the fact that such large amplitude motion may be strongly dissipative, as several experiments clearly indicate. The reason is that such processes lead to a large deformation of the system during which friction has time to act. Description using diffusion equations, such as Langevin [5] or Fokker-Planck formalisms [6], are typically well appropriated.

For reactions which are associated with compound nucleus excitation energies of less than 300 MeV, data are routinely compared to predictions of statistical model calculations. The choice of the parameters used in the model has to be done in order to successfully describe light particle emission. Studies of evaporated particle energy spectra yield therefore information about the main SM ingredients, the nuclear level density and barrier penetration probabilities.

Without entering in the detail of the statistical model, we just give an overview of the main concepts, remarking that the decay probability in a certain exit channel depends only on the width of the decaying resonance in a given exit channel [7].

1.2.1 Statistical model

The statistical model was originally introduced by N. Bohr [1], Bethe [8] and Weisskopf [9]. Wolfenstein [10] and Hauser and Feshbach [11] introduced the conservation of total angular momentum and afterwards the model was extended and generalized

by many authors. Actually it has a widespread use in nuclear physics and applied research.

Let us consider an excited nucleus of mass A, excitation energy U, charge Z and angular momentum J. The goal is to evaluate towards which states the system preferentially decays. The transition probability from an initial state i to a final state f is given by the Fermi Golden Rule [12, 14]:

$$\frac{dN_{i\to f}}{dt} \propto |M_{i\to f}|^2 \rho_f \tag{1.4}$$

where $M_{i\to f}$ is the transition matrix and ρ_f is the final density of states. The basic assumption of the statistical model is to consider that all transition matrix elements are equal, so that the probability of observing a given state is governed only by the density of final states.

The nucleus is an isolated system which may be properly described in a microcanonical approach. Let us apply the Fermi golden rule in a case where the final state 'f' corresponds to the emission by a parent nucleus 'i' (initial) of a particle 'b' of spin s, emitted with a kinetic energy between ϵ and $\epsilon + d\epsilon$. The corresponding emission (evaporation) probability per unit of time for the process $i \to b + f$ may be written as:

$$P_b(\epsilon)d\epsilon = C_0 \rho_f(E_f^*) dE_f^* (2s+1) \frac{4\pi p^2 dpV}{h^3} \tag{1.5}$$

where C_0 is a coefficient and can be obtained from the detailed balance principle [2]. The term $\rho_f(E_f^*)dE_f^*$ gives the number of states available for the excited E_f^* daughter nucleus and it is obtained by the product of the density of states $\rho_f(E_f^*)$ and the energy interval dE_f^* . The last term, $\frac{4\pi p^2 dpV}{h^3}$, indicates the number of states of the emitted particle with a linear momentum between p and p + dp; V is the volume of an imaginary box where the decay takes place. Evaluating eq.1.5 one finally obtains:

$$P_b(\epsilon)d\epsilon = \frac{\rho_f(E_f^*)}{\rho_i^{CN}(U)} (2s+1) \frac{4\pi p^2}{h^3} \sigma_c(\epsilon) d\epsilon \tag{1.6}$$

[2]the detailed balance principle assumes that the transition probability $W_{a\to b}$ of a system from an initial state a to a final stae b is related to the probability of the inverse transition: $\rho_a W_{a\to b} = \rho_b W_{b\to a}$, where ρ_a and ρ_b are the density of states a and b respectively and $W_{b\to a}$ indicates the transition probability "time-reversed" from b to a.

where $\sigma_c(\epsilon)$ is the capture (fusion) cross-section of the particle b by the final nucleus f [3]. A deexcitation channel will thus be the most favoured if the number of accessible states ($\propto \rho_f$) is large. To go beyond equation 1.6 it is necessary to express the ingredients of this formula, namely the densities of states and the inverse capture cross-section. The number of states available for a nucleus with an excitation energy between E^* and $E^* + \Delta E^*$ may be connected to the corresponding entropy S of the system (with Boltzmann constant k = 1)

$$S = ln(\rho(E^*)\Delta E^*) \tag{1.7}$$

and to its temperature, defined in the microcanonical approach as

$$\beta = \frac{1}{T} = \frac{dS}{dE^*} \approx \frac{\Delta ln\rho(E^*)}{\Delta E^*} \tag{1.8}$$

The density of states thus exhibits an exponential evolution with the excitation energy:

$$\rho(E^*) \propto e^{E^*/T} \tag{1.9}$$

which emphasizes the sensitivity of statistical models to this quantity. The capture cross-section in equation (1.6) may be written:

$$\sigma_c(\epsilon) = \sum_{l=0}^{\infty}(2l+1)\pi(\frac{\lambda}{2\pi})^2 T_l(\epsilon) \tag{1.10}$$

If the transmission coefficients T_l are set to unity, one obtains:

$$\sigma_c(\epsilon) = \pi R^2\left(1 - \frac{B_b^{Coul}}{\epsilon}\right), \quad \text{for} \quad \epsilon \geq B_b^{Coul} \tag{1.11}$$

and

$$\sigma_c(\epsilon) = 0 \quad \text{for} \quad \epsilon \leq B_b^{Coul} \tag{1.12}$$

where B_b^{Coul} is the Coulomb barrier associated with the emission of particle b. From all these equations, one finally obtains

$$P_b(\epsilon) = \frac{\epsilon - B_b^{Coul}}{T^2} e^{-(\epsilon - B_b^{Coul})/T} \quad \text{for} \quad \epsilon \geq B_b^{Coul} \tag{1.13}$$

[3] due to the detailed balance the capture reaction is directly related to the decay inverse reaction

In this expression $P_b(\epsilon)$ has been normalized to unity. The excitation energy E_f^* is expressed as a function of the kinetic energy ϵ : $E_f^* = E_{fmax}^* - \epsilon$. The exponential term of equation 1.13 comes from equation 1.9 used to express $\rho(E_f^*)$ as a function of ϵ. This means that the temperature T is the temperature of the final nucleus. It may be considered as independent of ϵ only for significant excitations. In other words, this statistical formalism is not valid for nuclei close to their ground state. This limitation is also required to derive simple expressions for the density of states.

The emission probability $P_b(\epsilon)$ exhibits a maxwellian shape which is typical of the decay of an equilibrated nucleus. It is worthwhile to remark that equation 1.13 has been obtained without the need of any nuclear model: the only ingredients which have been used are the microcanonical description of isolated systems, the density of states, the entropy and the temperature.

The competition between various channels (i.e. the emission probability for different particles) may be obtained from the integration of equation 1.13 before normalization. The total emission probability of a given particle b is essentially governed by the final density of states of the daughter nucleus:

$$P_b \propto \rho\left(E^* - Q_b - B_b^{Coul}\right). \tag{1.14}$$

In other words, for similar Q values, particles for which the Coulomb barrier is low, are preferentially emitted.

1.2.2 Level density

The nuclear level density (ρ) is an important quantity for the study of both thermal and decay properties of excited nuclei, for the determination of cross sections used in nuclear astrophysics calculations, like in neutron and proton capture processes, and in supernova dynamics. Moreover as stressed in paragraph 1.2.1 ρ is an essential ingredient in calculating the statistical decay of a compound nucleus (CN) by particle evaporation, gamma-ray emission, or fission in statistical models. The knowledge of the level density is thus highly needed in all regimes of excitation energies, compound

nucleus spins, and for the full range of Z and N from the β line of stability to the drip lines [4].

In statistical model calculations level density formulas are usually based on the work of Bethe [8], with the assumption that an energy independent density of single particle states g is present. Fermi-gas model approximation provides a useful reference to start with, even if other effects have to be included to get more realistic expression of the level density.

For a given energy E and particle number A, the density of states may formally be defined as

$$\rho(E,A) = \sum_{i,\ni} \delta(A - A_\ni)\delta(E - E_i(A_\ni)) \tag{1.15}$$

where the summation runs over all the states with $A_\ni$ particles and E_i energy. One usually uses an approximate expression when the nucleus can be described in a model of independent particles with single-particle energy levels ϵ_k, and for moderate excitation energies ($E^* = E - E_{gs}$)

$$\rho(E,A) \simeq \frac{1}{\sqrt{48}E^*} e^{2\sqrt{aE^*}} \tag{1.16}$$

where $'a'$ is the so-called level density parameter. At the same level of approximation, one can link the excitation energy to the temperature

$$E^* \simeq aT^2 \quad \text{with} \quad a = \frac{\pi^2}{6}\omega(\epsilon_F) \tag{1.17}$$

where the zero-temperature single-particle level density $\omega(\epsilon)$ reads:

$$\omega(\epsilon) + \sum_k \delta(\epsilon - \epsilon_k) \tag{1.18}$$

Note that the single-particle level density $\omega(\epsilon)$ counts here the number of single-particle levels per unit energy, while the density of states $\rho(E,A)$ counts the number of accessible states as a function of the total energy of the nucleus. Finally, one should keep in mind that equations 1.16 and 1.17 only hold for moderate temperatures

[4] On a chart of the nuclides, plotting proton number versus neutron number, the boundary beyond which neutron-rich nuclei are unstable against neutron emission.

($T \leq 3 - 4MeV$).

The Fermi energy ϵ_F plays a dominant role in the calculation of a and thus in the expression of $\rho(E, A)$. This reflects the fact that at low temperature the first levels to become empty are the least bound ones, namely the ones close to the Fermi energy. Elementary excitations which promote nucleons lying just below the Fermi level to just above it then become dominant.

Starting from an independent particle picture, which allows noticeable simplifications, the problem then occurs in the evaluation of the single-particle level density, and especially the level density parameter a. Realistic mean-field calculations do not allow the recovery of the experimental value of a. One has to take into account effects beyond the mean field, in order to reproduce the data. It is sufficient, here, to keep in mind the average experimental value $a \simeq A/8$ (up to shell effects)[13].

1.3 Evolution of decay mechanism: from evaporation to multifragmentation

We now consider the decay modes of hot nuclei when the excitation energy per nucleon E^* increases significantly above 1 MeV/u and may even reach values close to the binding energy per nucleon. In a somewhat arbitrary way, the transition from low-energy decay processes to high-energy processes is associated with the transition from evaporation/fission to fragmentation, namely the transition from a decay process in which two and only two massive fragments are emitted, to a process with at least three massive fragments in the final state.

A comparison of the two decay channels is made possible by counting the number of events in which two and only two massive fragments are observed and events in which at least three fragments have been emitted. In figure 1.2, the yield of three-body (Y3, fragmentation) versus two-body (Y2, binary decay) mechanisms is shown as a function of excitation energy per nucleon E^*: a sharp increase starts at about around 3 MeV/u. From this energy on, fragmentation begins to be a dominant process, although evap-

oration and fission are still present. It is worth noting that the ratio Y3/Y2 displayed in figure 1.2 is independent of the entrance channel (i.e. both of the projectile and the bombarding energy) and thus of the mechanism that led to the production of the hot nuclei considered in these experiments. This gives strong support to the fact that the transition is essentially governed by the excitation energy.

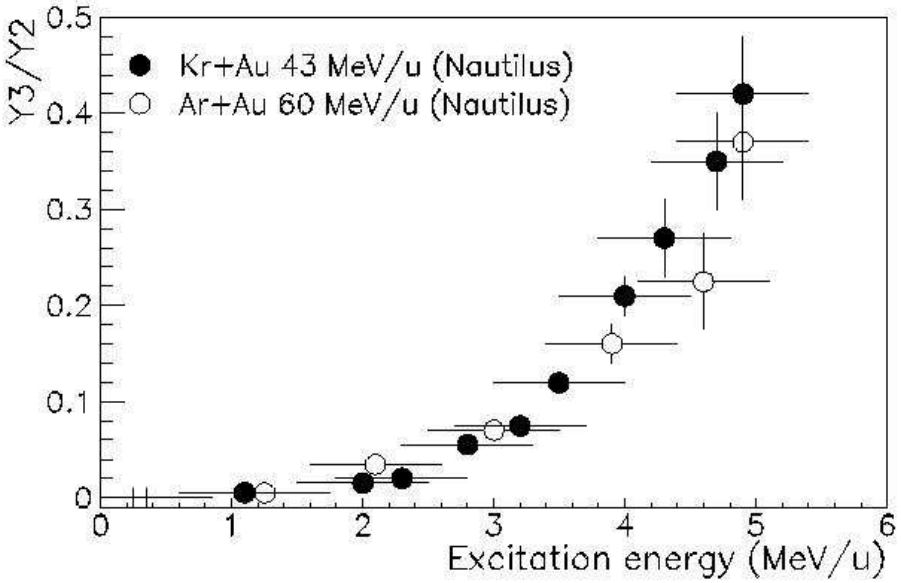

Figure 1.2: Evolution of the competition between two-body (Y2) and three-body (Y3) decay as a function of E^*.

The onset of multifragmentation, i.e. the simultaneus emission of at least three massive fragment takes place for excitation energies around 3 MeV/nucleon and the maximum for fragment production is found around 9 MeV/nucleon, i.e. close to the binding energy of nuclei. At higher excitation energy, due to the opening of the vaporization channel, the fragment production reduces.

On the other hand, average time intervals between successive emissions have been estimated by analysing space-time correlations between fragments, taking advantage of proximity effects induced by Coulomb repulsion.

A strong decrease of measured times with the increase of excitation energy is observed

up to around 5 MeV/nucleon. Then a saturation appears around 50-100 fm/c which reflects the limit of sensitivity of the method. For such short times fragments can be considered as emitted quasi simultaneously and fragment emissions can not be treated independently. Note that, sequential statistical models fail in reproducing the observed emission characteristics.

Chapter 2

The experimental apparatus

2.1 Introduction

In heavy ion reactions one has to deal with a very large range of energies and products. Often, going from the typical processes at low energy up to the most complex and dissipative phenomena at the higher energies, one can obtain the major information on a process, when dealing with the transition regions from a regime to another one. This is the case passing from the Compound Nucleus (CN) evaporation or Intermediate Mass Fragment sequential emission to the multi-fragmentation regime, and, again, going from the multi-fragmentation towards the vaporization regime etc.
The opportunity of studying the behaviour of the nuclear system which develops from one stage to another is very important: any modification in the nuclear matter characteristics (pressure, density, isospin etc), can be reflected in a variation of the experimental signatures, which carry important information.
To measure, disentangle and weight all decay channels of an excited CN it is necessary to detect and identify all the reaction products. Thus the use of GARFIELD detector, coupled with Ring Counter (RCo), is very well suited for such measurements.
The coupling of these two detectors allows to have an event by event nearly complete information on the residue, on light charged particles and on the intermediate mass

fragments. Moreover, since the coupled system covers ~4π of the total solid angle and has a high granularity, low energy thresholds, large dynamic ranges in energies and identification capabilities on an event by event basis, it allows for a complete reconstruction of the kinematics for each event.

2.2 The GARFIELD apparatus

The GARFIELD apparatus [15, 16] is particularly important: since it represents a powerful tool that can be used to study the evolution of the nuclear system from the low energy regime where mean field interactions are predominant to the intermediate energy regime where new open channels start to be present, due to the contribution of the nucleon-nucleon forces [14].

The mass and energy of reaction products can vary a lot: from light charged particles up to heavy fragments and from few KeV up to hundreds of MeV. The situation is, therefore, complex and it is very important to develop a detection system capable of detecting and identifying such a variety of reaction products [18]. The GARFIELD apparatus is based mainly on the ΔE-E technique, where the ΔE signal is given by the drift chamber where several microstrip anodes collect and amplify the primary electrons which were produced along the ionization track of the detected particle. Some CsI crystals, Thallium doped, are then used as stop detectors to get information on the residual energy. Fig. 2.1 shows a transversal section of the two drift chambers.

GARFIELD is made by two independent chambers, one for the forward angles and the other for the backward angles. In particular, with respect to the beam direction, they cover the range from $30^\circ < \theta < 85^\circ$ and from $95^\circ < t < 150^\circ$. For the azimutal angle φ, the forward camera covers $0^\circ < \varphi < 360^\circ$ and the backward chamber the part $0^\circ < \varphi < 70^\circ$ and $110^\circ < \varphi < 360^\circ$. The side opening in this chamber was designed to permit the positioning of possible ancillary detectors in this region.

One important parameter to be considered when designing a 4π apparatus is the possibility that 2 particles hit at the same time the same detector (double hit). To avoid this

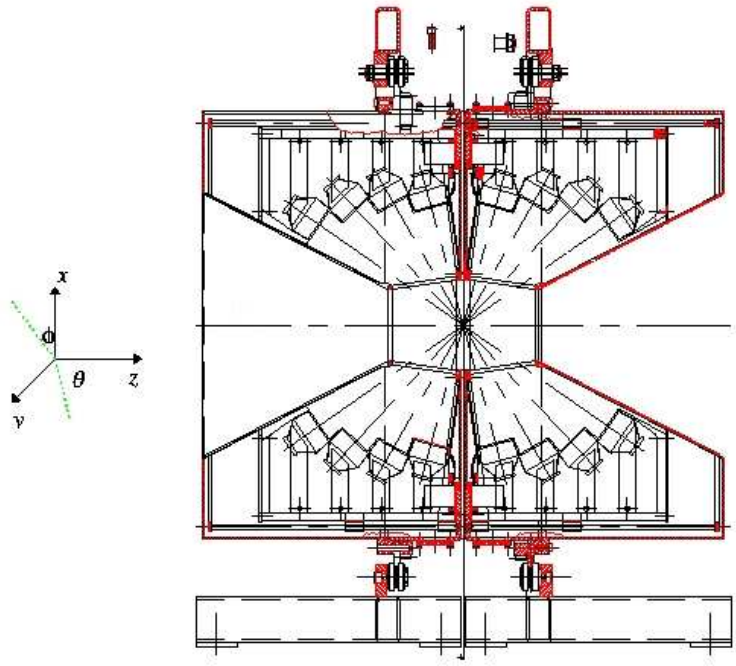

Figure 2.1: Trasversal section of the two chambers of Garfield

problem, it is important to have a high granularity. Normally a desired number of detectors is at least 10 times more than the maximum multiplicity expected for the product of interest. At relatively low energy, which is the range of interest for the physics to be studied with GARFIELD, maximum multiplicities around 15 for light particles plus 4-5 for heavy fragments (A> 4) are expected. We need, therefore, around 200 indipendent telescopes to perform a reasonable reconstruction of our events.

This granularity is obtained in the GARFIELD drift chambers dividing each of them in sectors of $\Delta\phi = 15°$. This means that the backward chamber is divided into 21 sectors, while the forward chamber into 24. Each sector contains 4 CsI(Tl) crystals positioned at different θ angles plus a microstrip pad (metallic strip photolithography on glass).

The microstrip pad is divided in the 4 collection regions up-right, up-left, down-right and down-left (see paragraph 2.2.2 for details). In figure 2.2, one can see the scheme of a drift sector.

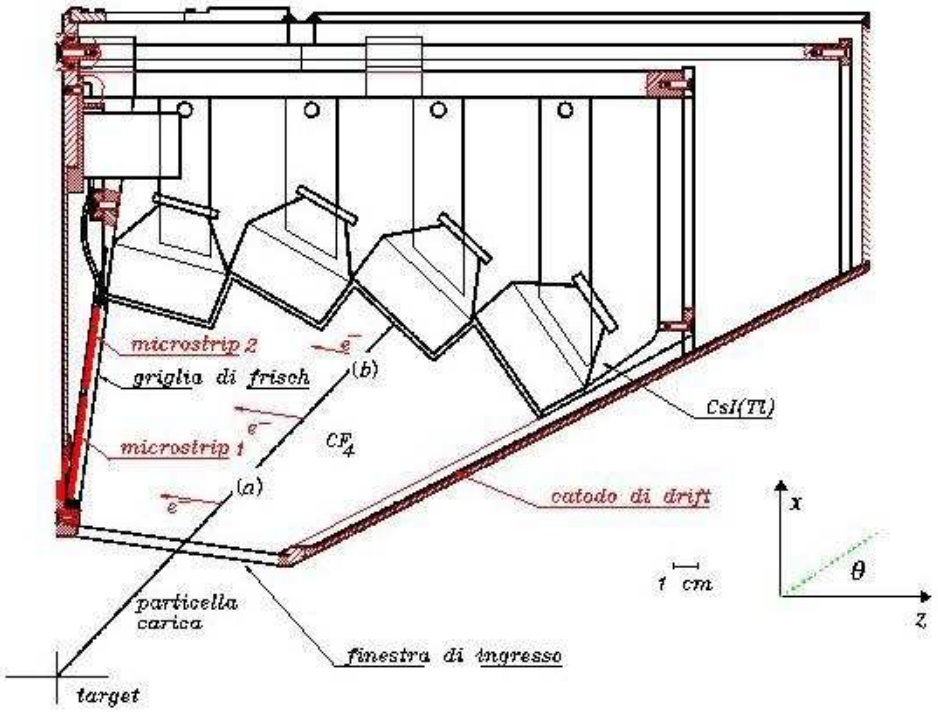

Figure 2.2: Scheme of a drift sector of GARFIELD

2.2.1 The CsI(Tl) crystals.

CsI(Tl) crystals have been chosen due to their excellent characteristics, like the high stopping power, the good energy resolution (close to 3% with 5.5 MeV α particles from 241Am source), the small sensitivity to the radiation damage, the relative small hygroscopy and the fact that they are quite easy to cut and machine in order to easily obtain the shape needed for the experiment. Moreover, the CsI(Tl) crystals are relativity cheep with respect to silicon detector.

In the GARFIELD apparatus there are 4 CsI(Tl) per sector, with a total number of 96 in the forward chamber and 84 in the backward chamber. The shapes are different as a function of the different θ angles where they are positioned. In fig. 2.3, one can see a drawing of the different dimensions of the crystals. Their shapes are designed so that

the front face is always perpendicular to the radial trajectory of the particle emitted from the target.

The shape of the backward part of the crystal is like a light guide to optimize the

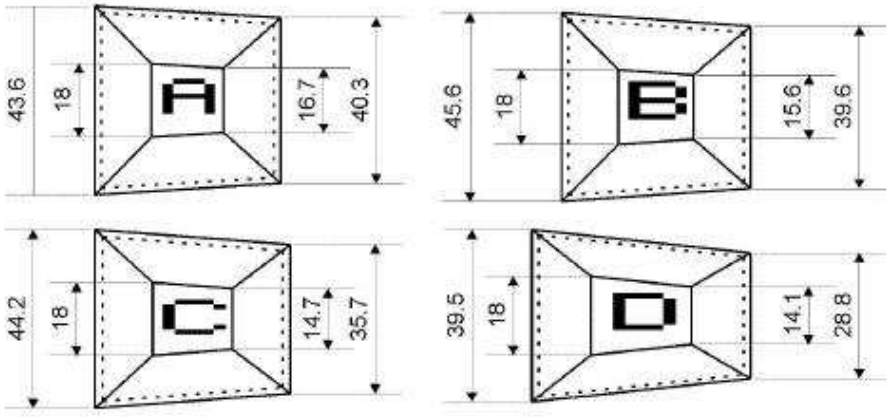

Figure 2.3: A drawing of the different shape of Garfield CsI(Tl) crystals. The A shape corresponds to the most near to the plane of micro (θ more big respect with to a beam line)

coupling with the photodiode S3204-05 produced by Hamamatsu (18 mm X 18 mm of dimension and 500 μm as depth). The use of photodiode instead of photomultiplier tubes is due to the good stability of the first and its smaller dimension which makes its mounting inside the gas volume much more feasible.

Before being mounted inside the apparatus, every crystal is tested using radioactive sources like the three peaks mixed α-source (^{241}Am (E=5.484 MeV), ^{239}Pu (E=5.155 MeV), ^{244}Cm (E=5.806 MeV)) and a γ source (like ^{60}Co which produces two lines at Eγ = 1.17 MeV and Eγ = 1.33 MeV) for investigation of the bulk. We calculated the resolution with the α-source using the average value of the FWHM (Full Width Half Maximum) of the 3 peaks.

The results obtained as resolution and light output from the α-source and from the γ-source are an indication on the crystal properties and on the gluing to the photodiode.

If the result is not satisfactory, i.e. larger than 4.5% for α-particles, we repeat at least one more time the procedure of preparation of the CsI crystal (cleaning with powder of diamond, gluing the photodiode, wrapping procedure).

2.2.2 The drift chamber

One of the most important requirements that a complete apparatus should fulfil, when used for studies of nuclear reaction mechanism with heavy ions, is the capability of identifying the reaction products with a low energy threshold, which permit to reconstruct the events where slow products are emitted.

The use of a gas detector is of great importance to fulfil these requirements, allow-

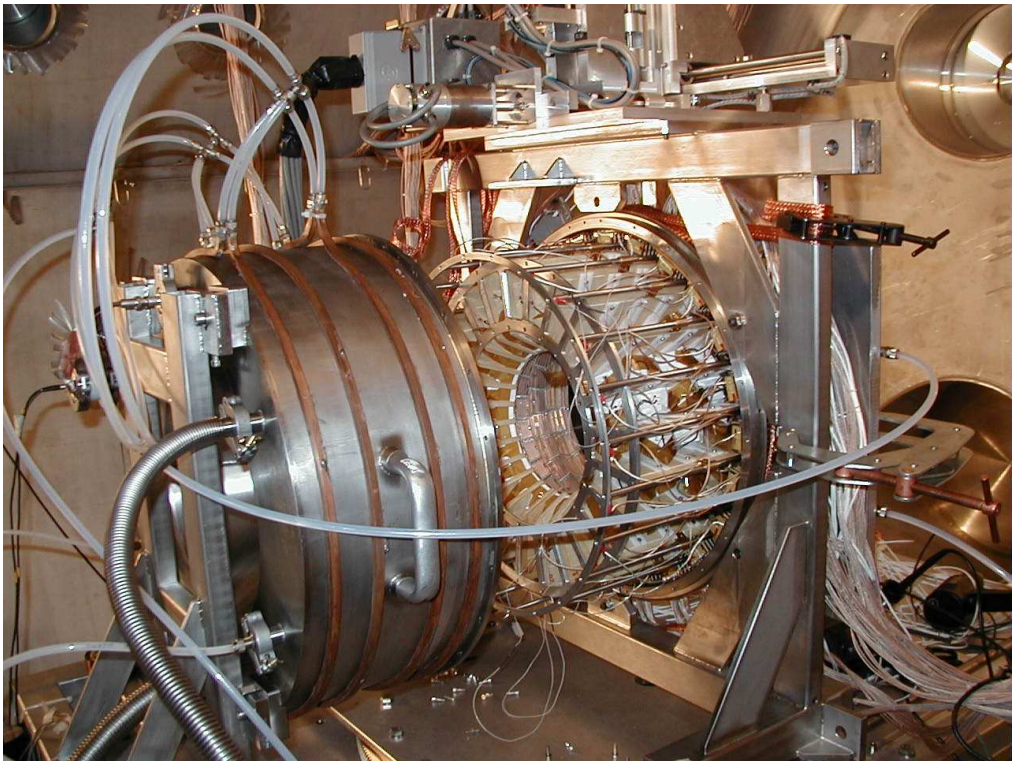

Figure 2.4: Ground of the cylinder of the Backward Camera. The microstrip plane can be seen.

ing an easy selection of the effective ΔE thickness, which is a compromise between a very low identification threshold and the necessity to handle large dynamical ranges of detected products. New possibilities for the gas ΔE section arose a few years ago with the development of micro-strip gas chambers (MSGC), initially designed to meet the severe needs of counting rate, high gain and position resolution of high energy physics. The originality of Garfield is in the use of this type of detector also in low energy physics ([19]). The advantages of using MSGC's are mainly due to the large dynamical range and to the signal-to noise ratio for the low ionizing ions, which is much higher as compared to ionization chambers. These two characteristics allow the simultaneous identification, with low energy threshold, of both light charged particles and heavy ions with an only two-stage telescope. In fact, the detector is characterized by a wide acceptance in Z, from 1 up to at least 28, with an identification threshold of about 0.8 MeV/A and a detection threshold much lower (of the order of 10-20 KeV/A). In fig. 2.5, one can see the drawing of the electric field inside a gas drift chamber of this kind. The drift lines are perpendicular to the microstrips plane and the intensity of the field is constant. After the Frish grid close to the microstrip plane, the field starts to have the dependence of 1/r, where r is the distance from the anodes, and the field intensity increases allowing an avalanche phenomena of multiplication of the primary electrons. In this way, we obtain a good electric signal which is still proportional to the initial ionization produced by the particle in the gas.

Each microstrip (fig. 2.6), as just told, is divided in 4 parts and it is made by hundreds of very small alternated metallic electrodes which are prepared through photolithography on glass. A very small distance (50 μm) between the single cathode and anode permits a fast collection of electrons and positive ions formed close to the microstrips plane, which results in a faster signal and a better reliability due to the fact that the electric field near the microstrips remains almost the same in time.

The anode strips, which are 10 μm large, are biased at $\approx$ 400 V and connected in 4 groups, while the cathode strips are connected all together and grounded. In this way we have only 4 signals from every microstrip. In fact, for our purposes, it is not needed

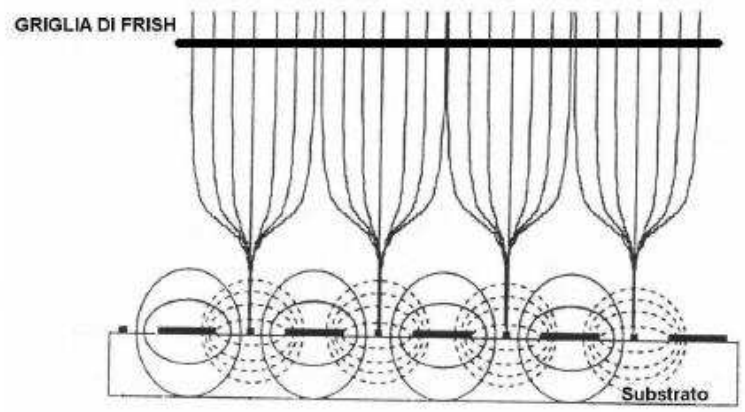

Figure 2.5: Drift line of the electric field inside a gas drift chamber with microstrip as collecting electrodes.

to read the single anode.

The angular resolution along the θ angle is given by the correlation with the different CsI(Tl) crystals, with a resolution of $\pm$ 7.5°. This resolution can be improved down to about 1° when the drift time information given from the microstrip electrons is used.

The ϕ resolution is fixed by the fact that a single microstrip is 15° and is divided longitudinally into two parts, so it can arrive down to 7.5°.

The gas inside the chamber is CF4, a gas characterized by a high stopping power and a high drift velocity (10 cm/μs at 1 V/cm.Torr) of the electrons produced in the ionization process. Due to this characteristic of the gas, the working pressure can be relativity low (50 $\div$ 200 mbar), with a great advantage for the safety of the entrance windows of the detector that can be thinner and for the field cage that can be maintained at lower voltage and have, therefore, less damage due to possible discharges.

In the GARFIELD apparatus, there is also a semi-automatic recycling gas system to circulate the CF4 inside the drift chamber. In this way we do not have problems connected to possible decrease of the gas quality.

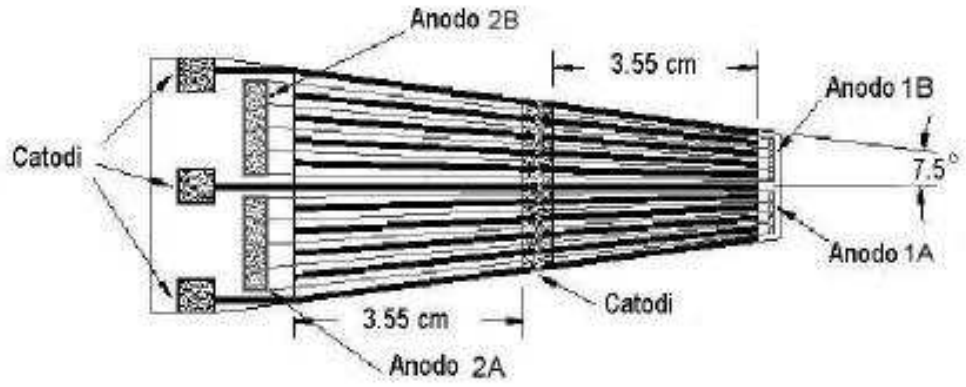

Figure 2.6: Scheme of a microstrip of Garfield.

2.3 Ring Counter

The Ring Counter (RCo) [20] is an annular detector designed to be centered at 0° with respect to the beam direction. It is an array of three-stage telescopes realized in a truncated cone shape. The first stage is an ionization chamber (IC), the second a strip silicon detector (Si) and the last stage a CsI(Tl) scintillator.

Each stage of the RCo is mounted on a low-mass aluminum support that is adjustable, for the relative alignment of all the active elements of the device. A picture of the whole apparatus is shown in Fig. 2.7.

The RCO is designed to operate in high vacuum (P$\approx 10^{-6}$ Torr) with minimal outgassing. The RCO has eight separate silicon detectors, pie shaped, each one segmented into eight independent annular strips on the front surface (junction side), thus increasing the granularity of the detector. The rear surface (ohmic side) consists of an unique electrode. Each strip has a bonding contact to a track in a Kapton ribbon ending with a multiple connector, allowing the connection to the preamplifiers. In front of each silicon detector there is a sector of a specially designed IC (see Section 2.3.1). Behind each silicon detector there are two 4.0 cm thick CsI(Tl) crystals (see Section 2.3.3), read out by photodiodes (PD). The geometrical shapes of the CsI crystals has been de-

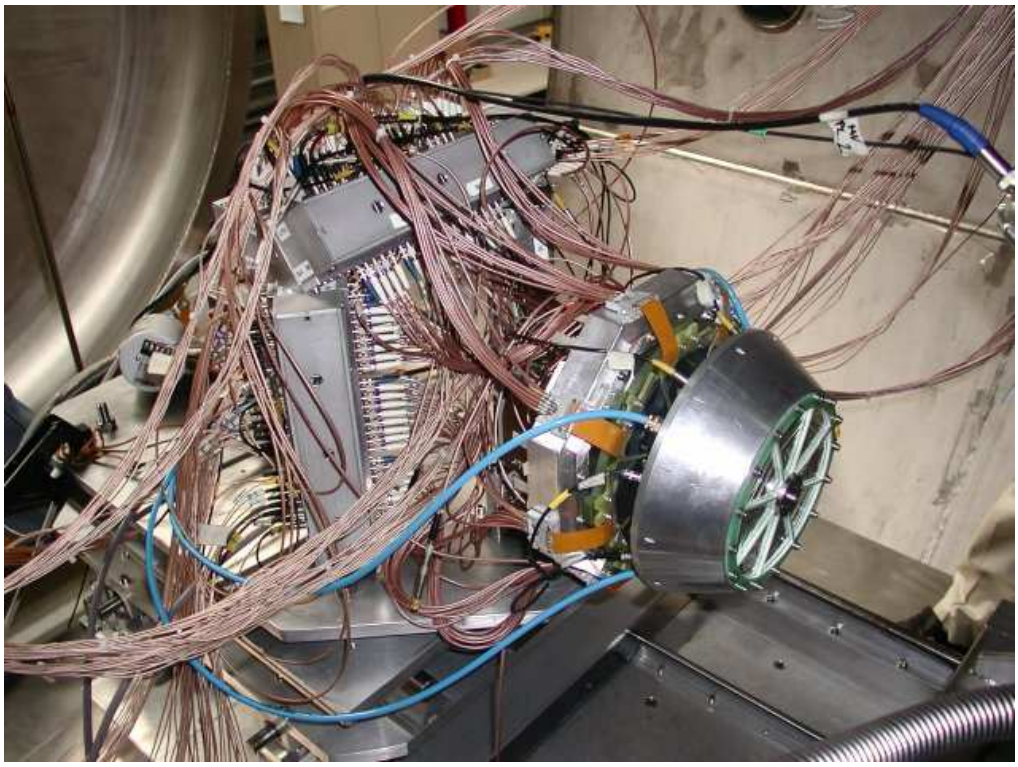

Figure 2.7: Ring Counter detector.

signed to cover the cone subtended by the IC. Each couple of crystals is related to one sector of the IC and in particular the CsI(Tl) closer to the beam axis covers the angular range of the four inner strips of the Si-detector, while the external CsI(Tl) covers the four outer strips.

The RCO is mounted on a sliding plate that can be moved forward and backward by means of a remote control. In the forward position the RCO is ready to operate, being inserted in the conical opening of the GARFIELD drift chambers. At the angles subtended by the RCo, silicon detectors can suffer rapid radiation damage by elastically scattered beams. Protecting the detector from the radiation damage is accomplished by inserting passive brass shields in front of the inner silicon strips, according to the grazing angle and the values of the cross-section of the considered reaction. With the sliding plate in the backward position it is also possible to insert a screen to avoid a

possible damage during the beam focusing.
In order to minimize the length and the capacitance of the cables and consequently the noise contribution, the preamplifiers are mounted inside the scattering chamber, on the same sliding plate of the RCO; they are placed in metallic boxes which shield them from external fields (see Fig. 2.7). The preamplifiers are thermally connected to the boxes which are cooled by a simple water cooling system (water temperature about 12°C), allowing for dispersion of the heat generated by the preamplifiers themselves.

2.3.1 The ionization chamber

The IC is divided in the azimuthal direction into eight equal detecting sectors. The IC, which is of the axial field type without Frish grid, has been especially designed to minimize the active area loss: its dead regions match the dead zones of the silicon detectors used as second telescope stage. The depth of the active gas region is 6 cm, the entrance and exit windows are aluminized mylar foils, 3 mm thick.
When the RCO is used as forward ring detector, coupled to the GARFIELD apparatus, the IC is very close to the external wall of the GARFIELD drift chamber. Therefore, it has been chosen to bias a middle electrode (1.5 mm thick doubly aluminized mylar) at a given voltage while keeping the entrance and exit windows grounded, in order to have the same electric field with one half of the potential needed for the whole thickness (about 150V at a pressure of 50mb of CF4). The CF4 gas, continuously flowing in the chamber, has been chosen because of its high density (0.19 mg/cm^3 at a pressure of 50 mbar and at a temperature of 20 °C) and high drift velocity (10 cm/ms at 1.25 V/cm/Torr). The latter parameter is important to reduce the electron collection time and the electron-positive ion recombination rate. The pressure inside the chamber is remotely controlled by a newly developed hardware and software system.
The gas enters the chamber through a filtering system for oxygen and water vapor suppression. The gas outlet is controlled by a dry root pump and by a valve whose opening is regulated by the control system in order to keep a constant pressure inside the chamber. Typical working pressures of the IC are in the range 50÷ 200 mbar,

depending on the measurements to be performed.

2.3.2 The silicon detectors

The eight silicon detectors [20, 21] have a trapezoidal shape (see Fig. 2.8) with dimensions which fit 18 of the total azimuthal angle and match the sectors of the IC.

Figure 2.8: One of the Si detectors of the RCo. Each one of the eight strips has a size of 8.55 mm. The full length of the silicon detector is 68.4mm (see Table 1).

The front surface (junction side) of each silicon detector is segmented into eight strips, which cover the polar angle regions quoted in Table 1, when the RCo is at the measuring position, at 270 mm from the target, corresponding to the minimal distance allowed by the mechanical structure of the Garfield chamber [15]. In Table 1 the internal and external radii of all the eight strips are also presented.
The covered polar angles run from 3.5° to 17.5° (see Table 1), corresponding to a solid angle of about 0.27 sr. The angular resolution of each strip is $\Delta\theta \sim \pm 0.9°$ and the geometrical coverage of the Si detector is about 90%.
The inactive area is due to the interstrip regions (about 220 μm wide), containing the guard rings all around the strips.
The guard rings have to be properly biased, in order to minimize the effects due to the

field distortion in the inter-strip region. This strongly reduces the charge split and the cross-talk between contiguous strips, keeping them to about 0.5 and therefore almost negligible. Another inactive area is the printed circuit board frame that holds each Silicon sector, which extends about 3.2mm beyond the physical dimension of the sector and provides the voltage supply and the extraction of the signals.
The thickness of the silicon detectors is around 300 mm, as stated by the manufacturer. Therefore the energy thresholds for particles punching through the detectors are about 6 MeV/A for protons and α-particles and 7-11 MeV/A for light fragments.

Strip	Int.radius (mm)	Ext.radius (mm)	Min.angle (deg)	Max.angle (deg)
1	77.9	85.0	15.3	16.7
2	70.8	77.8	14.0	15.3
3	63.7	70.7	12.6	14.0
4	56.6	63.6	11.3	12.6
5	49.4	56.4	9.9	11.3
6	42.3	49.3	8.5	9.9
7	35.2	42.2	7.1	8.5
8	26.2	35.1	5.3	7.1

Table 2.1: Radii and polar angle limits of RCo silicon strips

2.3.3 The CsI(Tl) scintillators

CsI(Tl) crystals [20] have been chosen as residual energy detectors because they have high density and therefore high stopping power for ions and light charged particles. In addition they are easily machined, not hygroscopic and can suffer without damage relatively strong mechanical shocks and also a relatively high radiation dose. Their density (4.51 g/cm3) makes them suitable to stop in few centimeters the ions to

be detected. The molar percentage of the Tl atoms in our CsI crystals is in the range of 1000-2000 ppm. The light emission is collected by PD and the optic coupling has been obtained by a two-component silicon glue. PDs have been chosen to read the light output because they require small space, have a good quantum efficiency for the CsI(TI) light emission spectrum, are insensitive to magnetic fields, have a good gain stability and require low bias voltages. However, the output signals are small, compared to those from a photomultiplier, thus requiring a careful signal treatment to optimize the energy resolution. We mounted Hamamatsu S320405 ($1.8\dot{1}.8 cm^2$) PDs, 500 μm thick, selected to have a dark current less than 15 nA.

2.3.4 Performances and operation

All the detectors of the RCo have been separately tested in the laboratory with collimated sources (1 mm in diameter) and the same electronic chain used for in-beam measurements. Fig. 2.9 shows the spectrum obtained for one of the Silicon strips with a ^{241}Am α-particle source. A three Gaussian fit is also shown where the three peaks correspond in energy and yield to the three decay lines at 5.486MeV (85.2%), 5.443MeV (12.6%) and 5.389MeV (1.3%). The resolution as obtained from the highest peak is about 0.5% FWHM. It should be noted that the strip resolution shown in Fig. 2.9 includes the electronic noise of the setup.

The CsI(Tl) crystals have been tested with a ^{60}Co γ-source in order to check the response in the bulk crystal (left panel of Fig. 5) and with a ^{239}Pu, ^{241}Am, ^{244}Cm α-particle source in order to measure the energy resolution (Fig. 2.10, right panel), which resulted in about 3-4% FWHM. Since it is well known that the light output of this kind of scintillators depends on the charge, mass and energy of the detected particles, a very careful energy calibration has been performed [22] at LNL with several beams at different energies, from protons to Ni. The FWHM energy resolution for the CsI(Tl) has been measured with several beams from ^{7}Li at 3-8 MeV/A to ^{58}Ni at 2-4 MeV/A directly impinging on the crystals during the CsI(Tl) calibration campaign [25]. We obtained resolutions (FWHM) ranging from 2.7% for ^{58}Ni at 239MeV to 3.3% for ^{7}Li

at 23.7MeV.

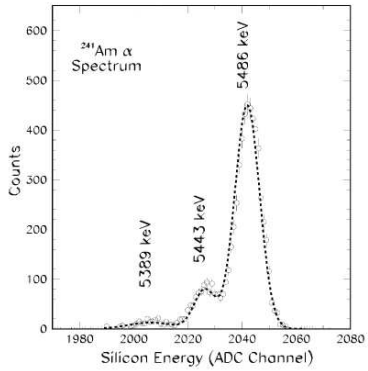

Figure 2.9: Energy spectrum of one of the strips of the silicon detectors, obtained with a collimated ^{241}Am α-source.

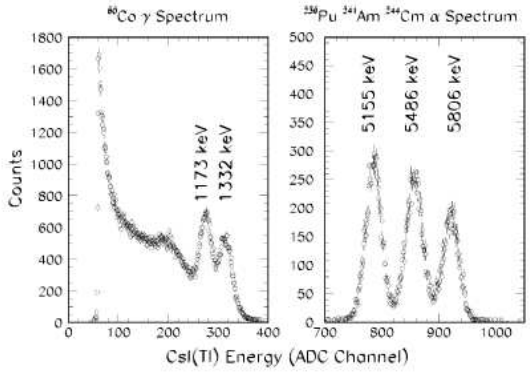

Figure 2.10: Energy spectrum of one of the CsI(Tl) crystals, obtained with a collimated 60Co γ-source (left) and a ^{239}Pu, ^{241}Am, ^{244}Cm collimated a-source (right).

A scatter plot of the energy loss in the IC as a function of the energy deposited in the Si detector is shown in Fig. 2.11 (left) for a telescope at 15° θ_{lab} . Energy calibration of the IC and Si signals were performed through calculated values of the energies released by scattered ^{32}S ions.

The energy resolutions for ^{32}S ions with elastic energies, stopped in the silicon detector, are 1.2% FWHM for the residual energy (Si) (Fig. 2.11 middle panel), including the kinematical spread due to angular extension of the strip and the energy straggling in the preceding IC and 11% FWHM for the energy loss in the IC (Fig. 2.11 right panel).

From Fig. 2.11, it appears that the overall resolution is good enough to obtain Z separation. The Z lines are clearly visible even beyond the projectile charge. When the

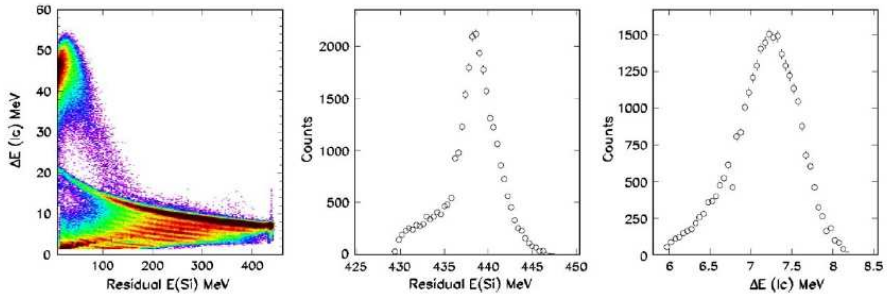

Figure 2.11: left: scatter plot of the IC energy loss versus the Si residual energy for the ^{32}S + ^{64}Ni reaction at 14.5 MeV/A, θ_{lab} = 9.8°; middle: residual energy spectrum of the scattered ^{32}S ions; right: energy loss spectrum of the scattered ^{32}S ions.

ions punch through the silicon detector, mass identification, at least for IMF charges up to Z=8, can be obtained from the correlation between the energy loss in the Si strip and the residual energy in the CsI scintillator (see Fig. 2.12). Very good identification starting from protons, deuterons, tritons up to the oxygen isotopes clearly appears from the figure.

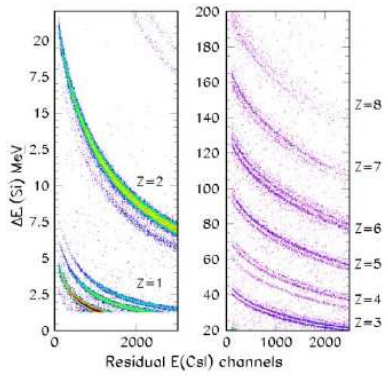

Figure 2.12: scatter plot of the Si energy loss vs. the CsI residual energy for $^{32}S + ^{64}Ni$ reaction for a strip at $\theta_{lab} = 9.8°$, summed over the entire experiment. The zoom in the left panel shows the resolution for Z=1 and Z=2 isotopes.

2.3.5 Improvements of the apparatus

To improve the granularity of the RCO and to have better performances we have:

1. replaced the 16 CsI(Tl) scintillators (two behind each silicon wafer) with 48 crystals (six behind each wafer). Indeed the granularity increases and the relative angle determination results more precise, greatly improving the measure of the relative momentum between isotopically identified fragments;

2. reverse mounted the silicon detectors. This would allow to exploit pulse shape analysis on GARFIELD's DSP-capable digital electronics [21].

In Fig. 2.13 a picture of the improved apparatus is shown.

The Ring Counter has been used for a series of measurements at the Tandem-ALPI complex of Legnaro Laboratories, aimed at checking the performances of the new combination of detectors of the Ring Counter.

The Z identification of particles stopped in Silicon was up to now performed via ΔE-E with analog signals from the IC and the Silicon detector. Since we have only one

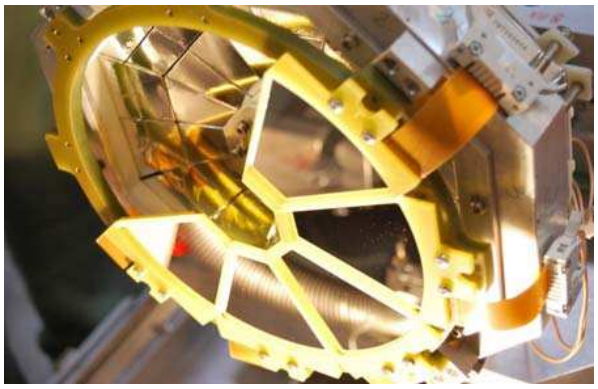

Figure 2.13: Picture of the new RCo. The Ionization Chamber (IC) and three sectors of the eight silicon detectors have been removed to show the new CsI(Tl) scintillators (six for each sector).

IC per sector the simultaneous Z identification by two methods will allow to recover double hits in the IC of fragments impinging in different strips. Moreover one has the hope of getting information not only on charges, but also on masses. The IC, mainly devoted to the detection of heavy residues and low-energy fragments, is still needed in order to keep the thresholds as low as possible.

Signals from RCo detector preamplifiers are now digitized and treated by the on-board DSPs of the custom electronics developed in the framework of NUCL-EX collaboration [23]. As already implemented for GARFIELD CsI(Tl) scintillators, the DSP extracts the energy information [23, 21] and other parameters of interest. In particular, CFD timing information is extracted for all signals, signal rise time and energy are calculated for Si detectors to perform pulse shape analysis on stopped ions, different filters are applied to CsI(Tl) signals to identify light charged particles.

Thanks to this feature, two new identification methods are now accessible, which were not possible with GARFIELD former electronics. The first is charge identification of particles stopped in the silicon detectors,exploiting the risetime vs. energy correlation (see fig. 2.14). The charge resolution is very good in the whole range, and mass can be extracted up to Z = 5÷6.

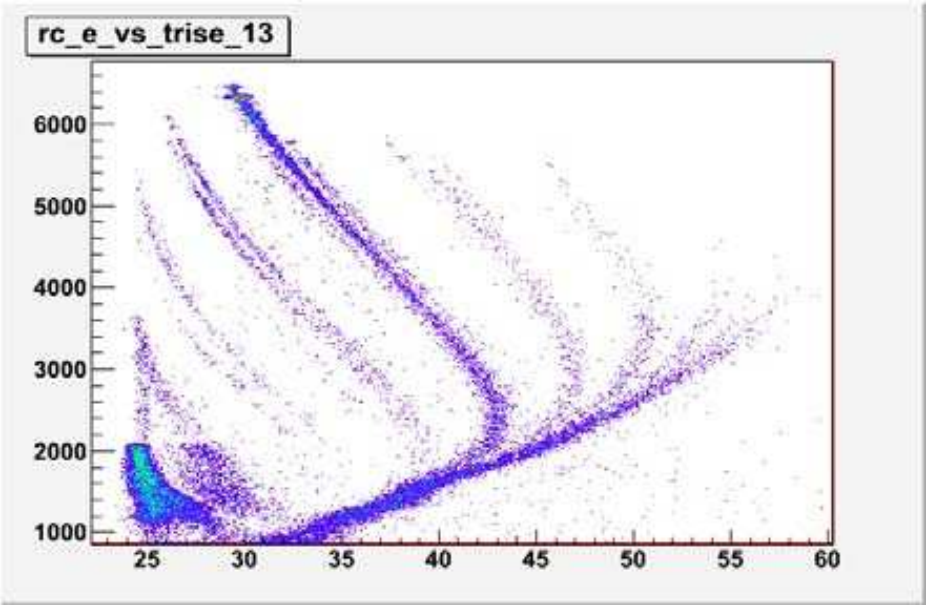

Figure 2.14: Energy-risetime plot for particles stopped in the silicon detector. Be, B and C isotopes can be disentangled.

The second is light charged particles identification from fast-slow correlations in the CsI(Tl) crystals, as shown in fig. 2.15: light products are clearly separated.In this way the thresholds of mass identification are lowered with respect to analog electronics.

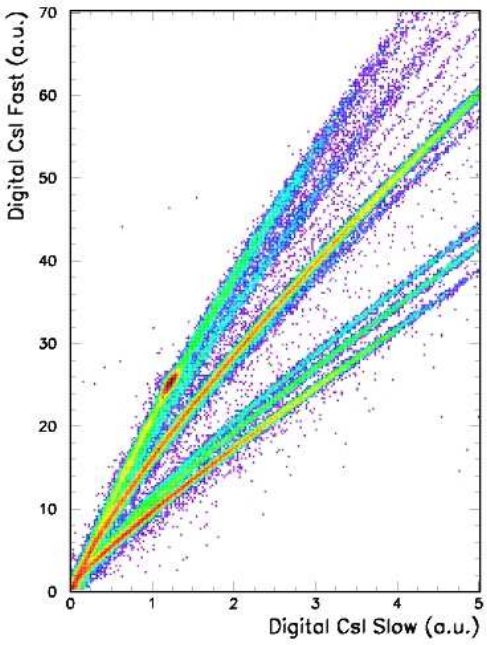

Figure 2.15: Pulse shape discrimination of light charged particles in CsI(Tl) performed by the on-board DSPs.

To the information obtained through the ΔE-E IC-Si or Si-CsI correlations, one can add charge and/or mass of the detected ions, exploiting the fast-slow correlation for CsI(Tl) and the risetime-energy correlation for the ions stopped in the silicon detector.

2.4 Analog electronic of GARFIELD apparatus

The analog electronic scheme of the Garfield apparatus can be explained referring to the sector modularity (Fig. 2.16). The 8 signals, 4 from the microstrips and 4 from the CsI, are processed by the pre-amplifiers placed inside the gas volume, very close to each detector. The pre-amplifiers work inside the drift chamber and therefore they have been designed to minimize the hot dissipation. A watercooling system to keep the temperature under control has been provided around the GARFIELD chambers.

The amplifier modules (CAEN N568B) are placed out of the scattering chamber, connected to the vacuum flange through 6 m of coaxial cables. They were opportunely designed for this apparatus.
Each module can have 16 channels, so it can analyze the signals coming from 4 sectors of CsI(Tl) crystals or 4 microstrips. Each entrance channel of the module is correlated to 3 output signals: one is fast and negative, the other two are slow and positive and different only for a gain factor. The two positive signals are the linear energy signals and they are fed into an ADC (Analogical-Digital Converter) and registered in the stored data.
The choice to have two different gains is due to the fact that the energetic range of particles detected in GARFIELD is quite large. The High Gain factor in the case of ΔE signal has been selected to better amplify signals of the light particles (Z = 1, 2) that loose a small quantity of energy in the gas.

The fast and negative signal from the amplifier is fed into a Constant Fraction Discriminator (CAEN C208). The CFD, which has 16 input channels, has got two ECL signals for every input. Besides that, an OR signal per module plus a sum signal are present. The sum signal can be chained in several CFD modules, so to obtain the final multiplicity signal. Different multiplicity trigger signals can be obtained by sending the multiplicity signal in a discriminator whose threshold can be set opportunely.
The fast signal of a CsI(Tl) crystal after being processed through the CFD is sent to form an OR with all the other CsI(Tl) signals so to have the main trigger of GARFIELD.
The fast signal of a microstrip detector is fed into some delay modules and then sent to the TDC to give the STOP signal. This signal is used for drift time measurement purposes. The START of the TDC is given by the main trigger, which is made by the general OR of all the trigger signals present in the experiment. To get the real time of reference, the START signal will be then corrected event by event through the Radiofrequency (RF) pulse, which has been registered event by event.

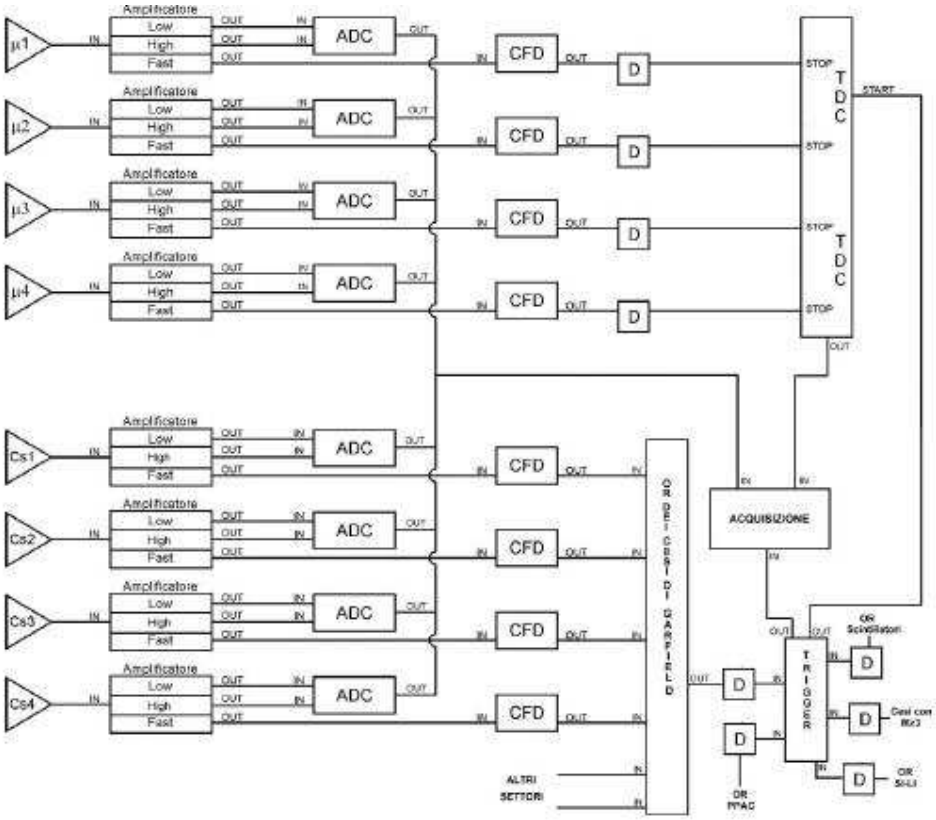

Figure 2.16: analog electronic scheme for GARFIELD apparatus.

2.5 Digital electronics

The identification of particles emitted in nuclear reactions in a wide range of kinetic energy, charge and, possibly, mass is an important feature requested to heavy ion experiments. The research in this field is mainly divided in two branches, not necessarily separated, one devoted to the development of new detectors, and the other concerning new methods of analysis.

Modern electronic sampling techniques (for example pipelining) have made it possible to design commercial high resolution fast sampling analog to digital converters (ADC) which permit to retain the high precision of the standard analog methods (for instance for the energy measurement), while the detailed information achievable with signal

sampling can be used in newly designed pulse shape discrimination applications. This may lead not only to better identification performances, but can also reduce the complexity of the electronics in high granularity 4π experiments like GARFIELD apparatus.

2.5.1 General description of the system and the algorithm structure

Fig. 2.17 shows a block diagram of a digitizing channel. Five sections can be identified: the analog input stage (programmable-gain amplifier and anti-aliasing filter), the digitizing section (ADC), the temporary storage section (FIFO memory), the processing section (DSP), the trigger section (programmable comparators and trigger logic).

The digitizing section exploits a 12-bit ADC operating at 125 MSamples/s and hav-

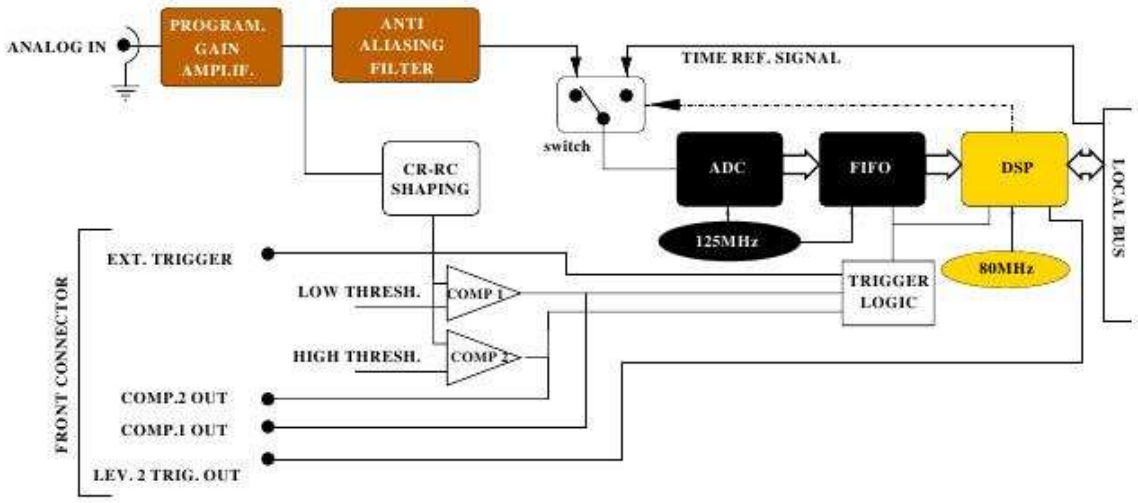

Figure 2.17: Digitizing channel block diagram.

ing an effective number of bits (ENOB) of about 10.7 [23]. In experimental tests we achieved satisfactory resolutions both in timing measurements and also featured good

particle identification capabilities over a wide dynamic range.

Typical characteristics of the digitizing channels, in this first version, are:

- 12-bit sampling at 125 MSamples/s.
- For channels with programmable input gain (like those employed at GARFIELD) 9.7ENOB are typical.

The ADC output values are continuously written to a First-In-First-Out (FIFO) memory which stores up to 8192 samples.
In many applications a good estimate of the signal baseline is mandatory [21]. In order to get this information, a suitable portion of the baseline preceding the particle signal must be sampled and collected. In our design, the first FIFO locations act as a circular buffer. They are continuously re-written while the channel is waiting for a trigger.
When a trigger signal is received, the trigger logic (see Fig. 2.17) enables the FIFO memory to be filled up so that the first samples of the stored signal will always correspond to a time interval preceding the trigger and can be used to calculate the current signal baseline.
The DSP reads sampled data from its I/O port, connected to the FIFO, and stores them in its internal data memory. The acquisition system loads the DSP program in DSP internal memory and starts the program execution through the DSP IDMA interface. The DSP controls the channel hardware, handles the validation logic of the event, performs signal analysis and prepares readout data in its internal memory. The acquisition system can read/write data from/to the DSP internal memory asynchronously through the DSP IDMA interface during program execution, for instance to read event data or to instruct the DSP to change gain, thresholds, etc.
The acquisition system can check the status of the digitizing channel (idle, analyzing, waiting for readout) by accessing the mother-board local bus and polling a few logic signals controlled by the DSP.
Signal storing in the FIFO and signal processing by the DSP are started by a trigger

signal coming either from an external device or from one of the two on-board comparators. The comparators thresholds are controlled by the DSP by means of a dedicated programmable digital-to-analog converter. The analog input signal is shaped by a CR-RC filter (t≈200 ns) before being sent to the comparators, as shown in Fig. 2.17.
The general structure of a DSP algorithm is shown in Fig. 2.18.

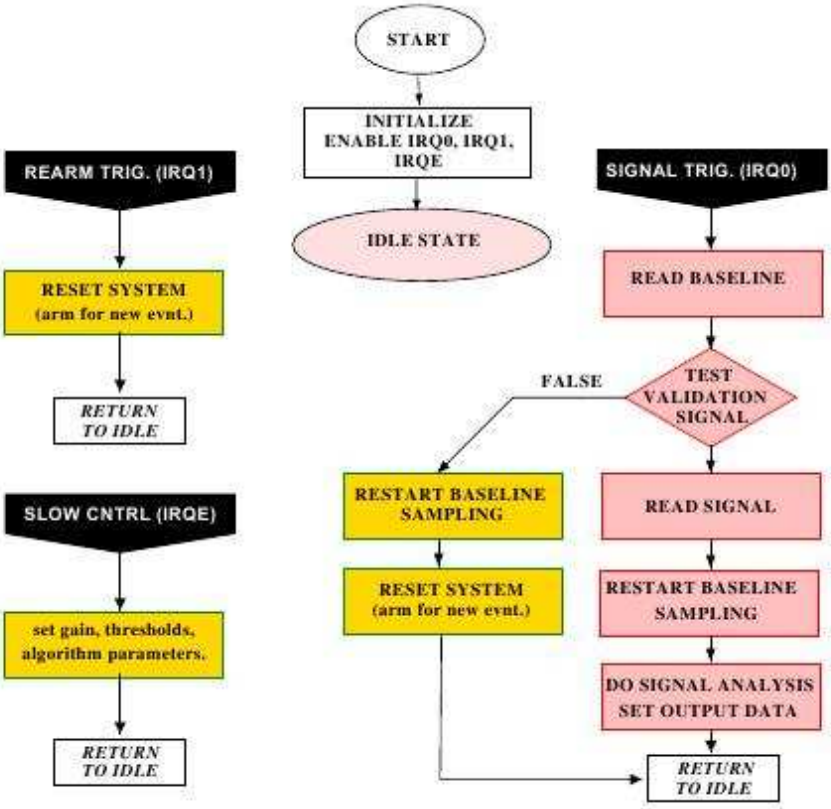

Figure 2.18: Flow chart of a DSP algorithm.

The DSP switches to an idle state after an initialization phase, performed once and for all at bootstrap time, where the DSP sets up its internal registers, channel gain and comparator thresholds, etc.
Upon receiving a signal trigger the DSP jumps to an interrupt service routine which spends a few microseconds reading samples from the FIFO, then checks a validation

signal.

In case of no validation, the DSP rearms the channel for a new trigger and returns to its idle state, otherwise it reads the remaining samples from the FIFO and restarts the circular buffer. The signal analysis phase follows. Since signal analysis lasts much longer than the buffer length expressed in ms, the buffer has been filled completely before a new trigger can be accepted.

After the analysis step, the DSP prepares the output data in its internal memory for readout and returns to its idle state. Readout takes place through the IDMA interface with no DSP intervention.

After all relevant data have been read, the acquisition system drives the DSP IRQ1 interrupt signal (one of the local bus signals on the mother-board) thus instructing the DSP to rearm the channel for a new trigger, as shown on the left side of Fig. 2.18.

Hardware settings and algorithm parameters can be accessed using a dedicated “slow control” interrupt routine associated to the IRQE interrupt signal.

2.5.2 Pulse Shape Discrimination in CsI(Tl)

The pulse shape discrimination algorithm mimics a wellknown analog method, sketched in the left part of Fig. 2.19. The detector signal is fed in parallel to two filters of different time constants, a ”fast” shaper and a ”slow” shaper. The analog chain at the left of Fig. 2.19 is replaced in our case by the much simpler chain sketched in the right half of the figure and the two filters are calculated by the DSP.

The calculated ”fast” shaper is a semi-Gaussian filter with t≈700 ns, the calculated ”slow” shaper is a filter with t≈2000 ns. The amplitudes of the filtered signals (A_f and A_s) are stored for the off-line analysis. A fast-slow correlation-actually Af vs. $A_s - f\dot{A}_f$ where f≈4 is shown in Fig. 2.20. Hydrogen and helium isotopes are clearly resolved.

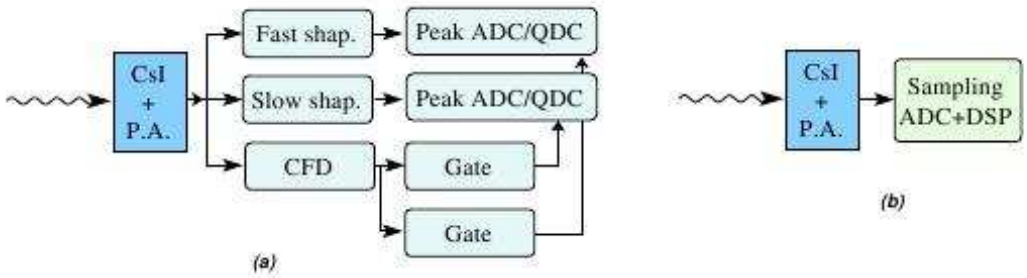

Figure 2.19: A typical analog chain for pulse shape discrimination (left) compared to the set-up described in this paper (right).

2.6 The acquisition system

The GARFIELD apparatus is complex: both the number of parameters that have to be recorded and the acquisition rate can be large, so the acquisition system has to be really powerful and flexible.
The system, based on FAIR front-end (Fast Advanced Interface Read-out) developed by the I.N.F.N. section of Napoli, is an ECL bus dedicated to the fast read-out of electronic acquisitions modules.

The velocity transmission of data on the bus is 1.25 Gbits/s and the architecture of the system is on two levels (Fig. 2.21):

- at low level, the single electronic modules (ADC e TDC) are grouped in segments. Every group is controlled by its own Segment Controller (SEGC). In the present experiment 4 segments have been used.

- at high level , every Segment Controller can communicate with the System Controller.

Due to the performances of the Segment Controller, it is possible to have an event by event identification of the trigger pattern. In fact, the main trigger is composed by an OR logical condition of several trigger signals, like it will be described in the

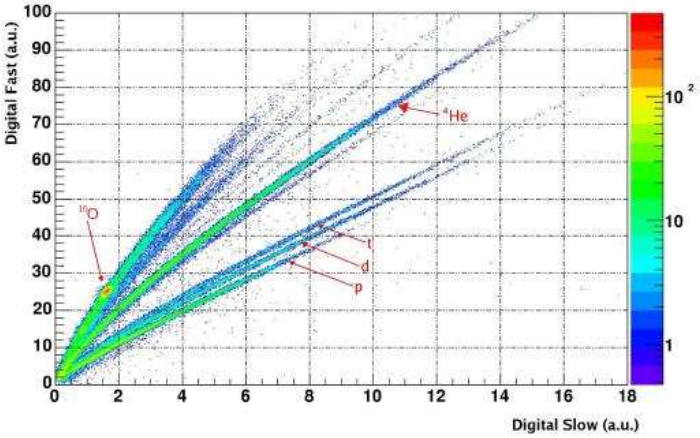

Figure 2.20: Pulse shape discrimination of light charged particles in CsI(Tl) performed by the on-board DSP.

following chapter.

Through the acquisition system it is possible to modify remotely the ADC and TDC set up (thresholds, ranges, etc..). We will explain better all these possibilities in the fourth chapter, where the present experiment will be discussed in detail.

In conclusion, this acquisition system can work up to 10^7 parameters, with 32 bit for each. All the operations needed are done without any software protocol, using an auto-configuration procedure, which is able to recognize directly the kind of module (ADC, TDC, delay etc.) and assign to each module a virtual station number (VSN) to make it recognizable in the off-line analysis.

The final data are written on the disks of a Personal Computer used like a storage. It is also possible to monitor the experimental spectra with a graphic interface of the acquisition system.

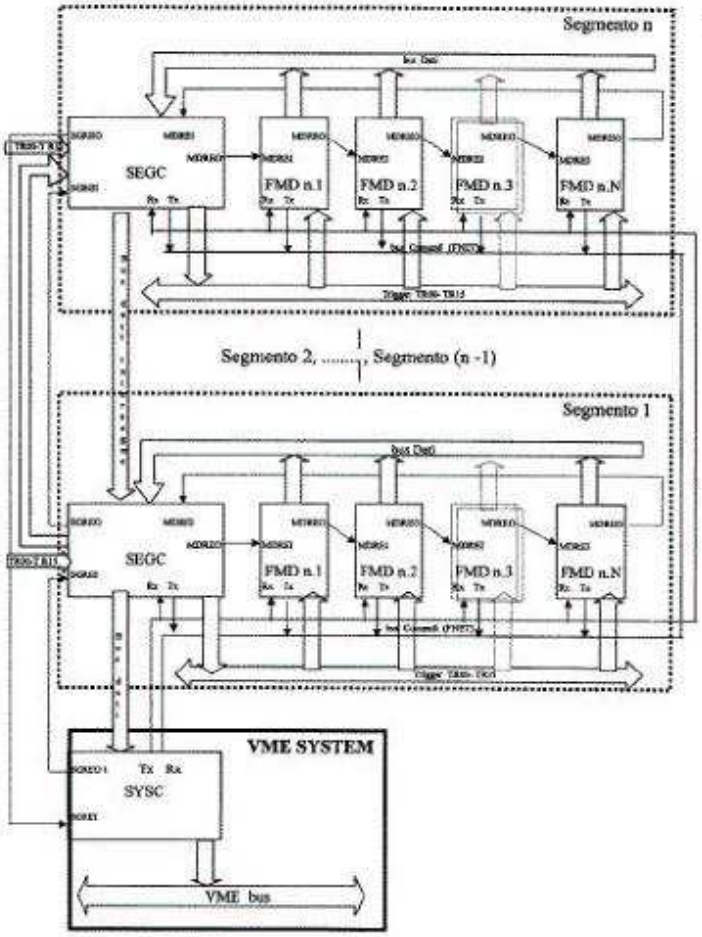
Segmento n
SEGC
FMD n.1
FMD n.2
FMD n.3
FMD n.N
Segmento 2, ..., Segmento (n -1)
Segmento 1
SEGC
FMD n.1
FMD n.2
FMD n.3
FMD n.N
VME SYSTEM
SYSC
VME bus

Figure 2.21:

Chapter 3

The experiment

The goal of the experiment analyzed in this thesis is the study of the de-exitaction properties of CN formed in collisions between ^{32}S and two different stable Ni isotopes at incident energies around 13 AMeV. The experiment is part of a wider study on dynamical and thermodynamical properties of the nuclear matter, undertaken by the NUCL-EX group [24].

3.1 Reaction

The experiment was performed at the INFN National Laboratory of Legnaro (LNL) using a beam from the Tandem XTU and the LINAC ALPI accelerators (Fig. 3.1). The ion beam time structure is pulsed. Each ion burst has, as a first approximation, a gaussian distribution with a Full Width Half Maximum (FWHM) of ~3 ns.

The beam arriving on the target is synchronized with the ion accelerating electric field radiofrequency (RF). The RF signal can be therefore used as reference for time measurement. The main beam characteristics are reported in tab.3.1. The analyzed reactions are reported in tab. 3.2.

The beam energy (~14.5 AMeV) is chosen following the criteria of reducing the preequilibrium effects and having sufficient recoil energy for nuclear charge identification of residues.

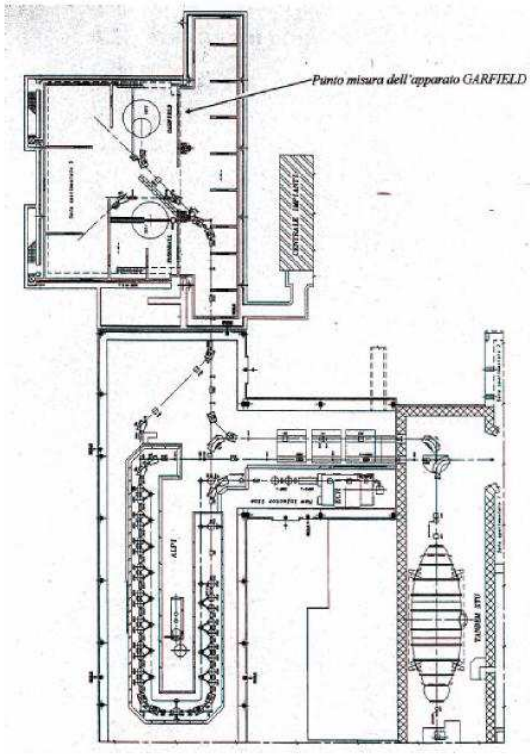

Figure 3.1: Scheme of the the Tandem XTU and the LINAC ALPI accelerators

Beam	I(pps)	$E_{beamAMeV}$	$\nu_{RF}(MHz)$
^{32}S	....	14.5	.....

At this incident energy complete and incomplete fusion reaction mechanisms are both present. Recoil energy criteria should allow to determine whether the observed reactions are mostly complete or incomplete fusion ones.

The target thickness of ... μg/cm2, leading to a mean energy loss of about ~...AMeV for the considered residue, had been chosen as compromise between a large enough number of events and a still sufficient residue velocity for identification.

Beam	E_{beam}	Target	dx ($\mu g/cm^2$)
^{32}S	14.5	^{58}Ni	150
^{32}S	14.5	^{64}Ni	150

3.2 Trigger configurations

The choice of the logic of the trigger is a crucial problem for every experiment because it is strictly connected to the selection of the reaction mechanism that you are going to study. Normally, more then one processes are of interest inside an experiment. Therefore, the main trigger is pratically obtained by performing logical condition of chosen signals coming from the different detectors.

This leads to a selection of events with a relevant meaning from the point of view of the physics. In the case of our experiment, the main process to select was the Compound Nucleus formation, which is the fusion of the projectile with the target into an equilibrated hot and thermalized system. During the following decay of this CN, we have a production of light particles and IMF that we want to study.

The main trigger is then obtained from the AND of different trigger signals of interest. In particular, we got the OR-GARFIELD (OR of all CsI(Tl)), which gives the “inclusive“ trigger for light charged particles and fragments, the OR-RCO which gives the ”inclusive” trigger of residue, fragments and light particles emitted in forward direction. When used alone, these trigger signals were opportunely reduced to diminish the counting rates.

The most important trigger for the experiment were coming from the coincidence between OR-GARFIELD with OR-RCO, without any reduction.

In Fig 3.2., one can see a scheme of the main trigger. The last two signals of Fig. 3.2. inserted in the main trigger were used only for particular tasks and were not switched on during the real data taking.

In particular, the pulser trigger is used to make routinely inside the experiment some control runs where the signals of electronics come from controlled and known pulser

input signals.

The use of a standard input source, like a pulser, is crucial in this experiment because it makes possible to check the stability of the electronics during the measurement and especially to compare experiment performed in different periods.

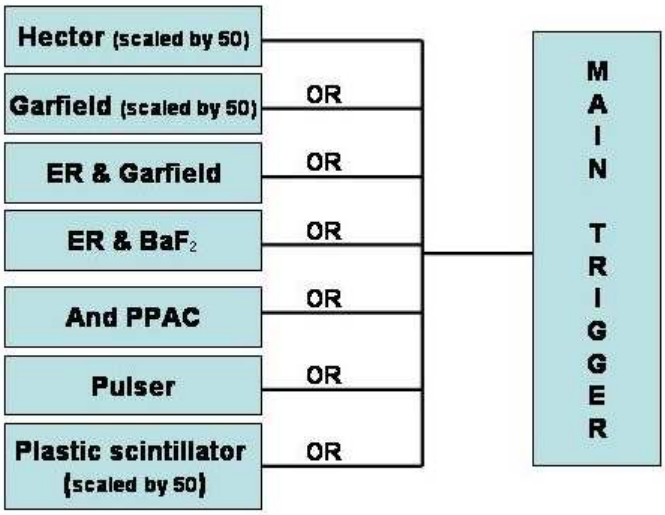

Figure 3.2: Scheme of the main trigger of the experiment

The last trigger is from plastic scintillator that were positioned all around the beam line at small angles. In this way, they could collect the elastic scattering and produce a time spectra from which it was possible to determine and keep under control the time resolution of the beam.

From time to time, a pure elastic scattering measurement (using a gold target) was performed to have a clear time of flight spectrum to control the beam time structure. A continuous monitoring was anyway performed during the whole measurement to take under control possible deterioration of the pulsed beam.

3.3 Online checks: GARFIELD monitor program

The monitor program provides a simple way for defining and thus visualizing an arbitrary number of 1D and 2D histograms, filled either with raw experimental data or with preprocessed variables (simple combinations of two or more experimental parameters, linear calibrations).

Histograms are displayed grouped into “pages”. At the time of this writing ~ 3000 histograms and ~ 250 pages are routinely used. Since such a number of histograms may not fit into a single computer memory, histograms are organized also in “categories”.

1D histograms can also be declared as “pedestal” histograms, i.e. histograms that can be used for a pedestal evaluation of standard ADC/QDC modules. During pedestal runs, the monitor program can recompute all pedestals on-demand and the result can be further manually adjusted using the GUI. Finally the pedestals are loaded by the acquisition system. In Fig. 3.3 a screenshot of the main window is shown.

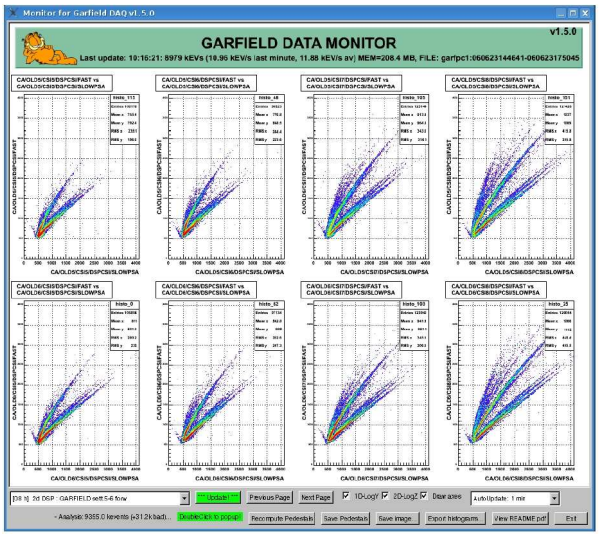

Figure 3.3: Screenshot of the main window of the monitor program. In the top part of the window some information about the analysis is given, whereas various functions can be accessed by using the buttons at the bottom.

By using the GUI it is possible to navigate thought the different pages and inspect the various histograms. An expanded view of each histogram can be obtained by double-clicking the corresponding window.
Any arbitrary selection of histograms can be exported into various formats (ROOT, ZEBRA, binary, text) for later replay with the user's favorite software.
The acquisition system stores data on a dedicated machine where a data dispatcher daemon is running. Clients can connect from any host and ask for a given run set, that is transmitted thought a TCP connection.

3.3.1 Dead time check

The dead time is the time interval during which the acquisition system acquires the measured parameters. During this time window the system is inhibited and all new events are lost.
The dead time is an important parameter to check during the experiment because it limits the counting rate. The dead time percentage has been monitored during the experiment and kept around 30% by adjusting the beam intensity.

3.3.2 Pressure controls

During all the measurements the gas pressure stability in the ionization chambers has been monitored, since a pressure variation requires a new energy calibration of the ionization chambers. The gas pressure in GARFIELD ionization chambers has been set in order to obtain a good charge resolution in $\Delta E - E$ spectra. Increasing the gas pressure, the resolution gets better, but simultaneously the energy threshold for particle punching through the ionization chamber increases.

3.4 Calibration runs

During the experiment several calibration runs have been performed:

Pulser runs: a pulser signal is sent to GARFIELD and RCO in order to get the mV/ch calibration factor.

Time calibrator runs: Time calibrator signals, with a known period, are sent to all the TDC used in the electronic chains. It allows to determine the ns/ch calibration factor for each TDC.

Chapter 4

Data reconstruction and Identification methods

4.1 Data reconstruction

A ”raw” event is a list of acquisition data parameters characterized by the same event number. The events reconstruction consists in the analysis of the acquired parameters in order to reconstruct physical particles, transforming list of hit detectors into list of particles. A reconstructed event is characterized by the event number and the particles multiplicity, while each particle is characterized by the identification number of the hit telescope and by the energy of each fired detector. The GARFIELD detector uses different techniques to measure energy and velocity of the detected particles and to identify them in charge and/or mass [25]. The, up to now, employed detection techniques are summarized in the following:

- The ΔE-E technique, using the signals coming from two layers of detection (es. Silicon and CsI(Tl) detectors), is employed for charge and mass identification:

    1. for GARFIELD apparatus the ΔE-E technique, using the signals coming from microstrip electrodes and scintillator (only charge identification);Fig.4.1.

2. for RCO detector there are two ΔE-E stage: the first step uses the signals coming from IC (ΔE) and silicon (E) detector (only charge identification), the second step use the signals coming from silicon (ΔE) and scintillator (E) detectors (charge and mass identification up to projectile-like nuclei);Fig.4.2.

- The Pulse Shape Discrimination technique, using the fast and slow component of CsI(Tl) signals, is used to identify the light charged particles; this method allows isotopic separation for particles with Z≤4 stopped in the CsI(Tl) scintillator;Fig.4.1.

- The Pulse Shape Discrimination technique in silicon detector, using energy and risetime signals, is used to identify the light charged particles anf IMF fragments stopped in silicon; this method allows isotopic separation for particles with Z≤14 stopped in the Si detector;Fig.4.2.

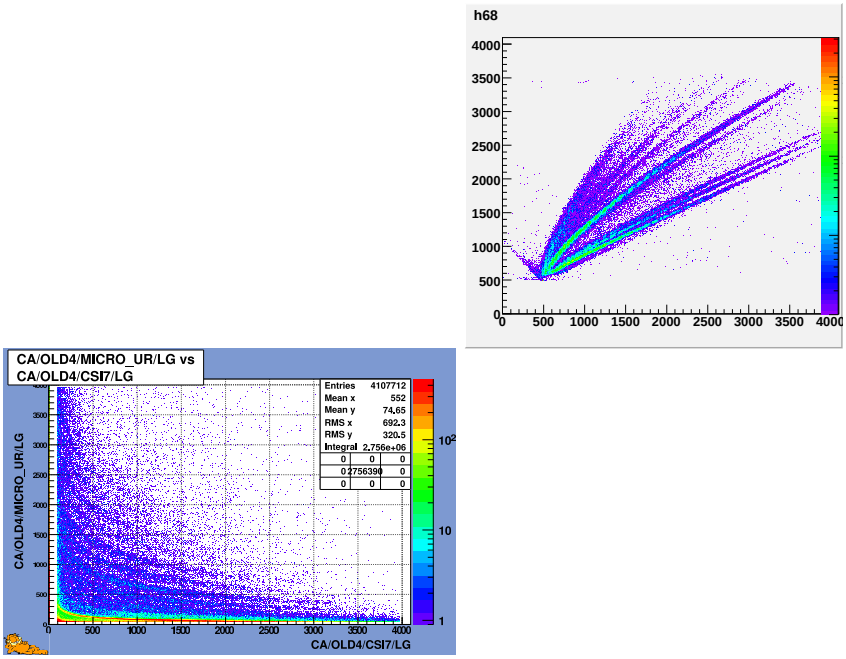

Figure 4.1: ΔE-E and Pulse Shape Discrimination technique for GARFIELD.

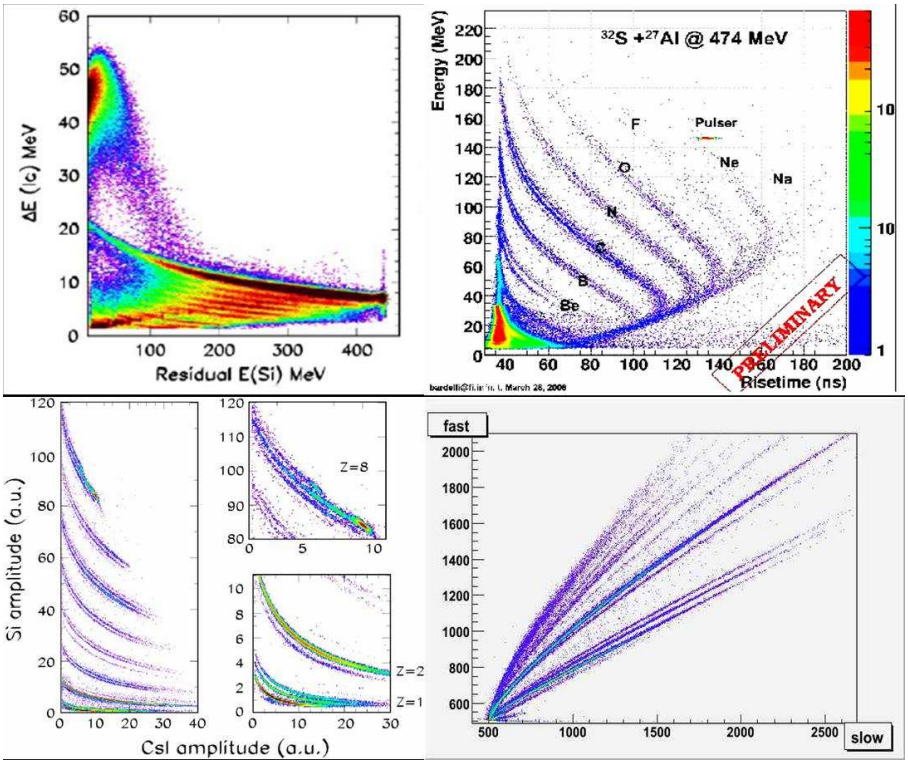

Figure 4.2: ΔE-E and Pulse Shape Discrimination technique for RCO.

4.2 ΔE-E method

The study of the N/Z dependence of level density parameter requires fragment and light particle mass and charge identifications over a wide energy range. GARFIELD multidetector, thanks to its structure constituted by telescopes, i.e. different detection layers, allows to perform the identification in mass A and charge Z of the detected particles through ΔE-E technique.

The ΔE-E method requires that the incident particle punches through at least the first detection layer.

The specific energy loss $(-dE/dx)$ for charged particles in a given absorber, with density ρ and charge and mass respectively Z_T and A_T , is described by the Bethe formula

[26]:

$$-\frac{dE}{dx} = 4\pi N_A r_e^2 \rho m_e c^2 \frac{Z_T}{A_T}\left(\frac{Z}{\beta}\right)^2\left[\ln\left(\frac{2m^e c^2\beta^2}{I\,(1-\beta^2)}\right)-\beta^2\right] \tag{4.1}$$

where $r_e = \frac{e^2}{4\pi\epsilon_0 m_e c^2}$ is the classical electron radii and m_e the electron rest mass. The parameter I represents the average excitation and ionization potential of the absorber. Z and β are the charge state and velocity of the incident ion, respectively. Eq.4.1 takes into account interactions between the incident ion and the electrons of the absorber, neglecting the interactions with the nuclei of the absorber, which are significant just at the end of the particle's track.

It is generally valid for different types of charged particles provided their velocity remains large compared with the velocity of the orbital electrons in the absorbing atoms. In non-relativistic limit ($\beta \to 0$), eq.4.1 becomes:

$$-\frac{dE}{dx} = C_1\frac{m_e Z^2}{\beta^2}\ln\left(C_2\frac{\beta^2}{m_e}\right) \tag{4.2}$$

and, neglecting the logarithmic β dependence,

$$-\frac{dE}{dx} \approx \frac{Z^2}{\beta^2} \propto \frac{Z^2}{f(E/A)} \tag{4.3}$$

where E is the incident particle kinetic energy and A its mass. The specific energy loss, for a given incident energy E, presents a relevant dependence from the incident particle charge Z and a lesser one from its mass A. Therefore a ΔE-E correlation presents the typical Z edges as shown in fig. 4.3, and, if the ΔE energy resolution is sufficiently good, also the A dependence can be pointed out.

4.2.1 Particle identification method for ΔE-E matrix

The necessary step before the data analysis is the calibration of the measured signals. However, due to the fact that different detectors (ionization chambers, microstrips, semiconductors, scintillators) can be used, due to the rich variety of nuclear

species produced in the reaction in a wide energy range and to the large number of telescopes covering the laboratory solid angle, this preliminary step is quite man-power and time consuming.
A fast and reliable method to assign the mass and charge of the detected ions is therefore highly desirable.
Analytical reductions [27] of expression 4.3 lead to

$$\Delta E + \left[E^{\mu+1} + (\mu+1)\, Z^2 A^{\mu} \Delta X\right]^{1/(\mu+1)} - E \tag{4.4}$$

in the case of particles detected in a ΔE-E telescope. ΔX is the thickness of the first detector, where the ion deposits an energy ΔE. In the second detector the ion is stopped and releases an energy E. To obtain Eq.4.4 from Eq.4.3 the hypothesis that $f(E/A)$ is a power-law $f(E/A) = (E/A)^{\mu}$ with exponent $\mu \approx 1$ has been made. Eq.4.4 is the basic formula to build particle identification functions (p.i.f.) for charge identification.
For instance, if we aim to identify the charge Z of a detected particle/fragment from the measured ΔE; E signals, we can calculate a not calibrated measure of Z (p.i.f.), which includes some unknown constants

$$p.i.f. = \left[(\Delta E + E)^{\mu+1} - E^{\mu+1}\right]^{1/(\mu+2)} \tag{4.5}$$

with the assumption A=2Z: However, it is experimentally well known that it is quite difficult, by managing the only parameter μ; to find a unique p.i.f. able to linearize the ΔE-E correlation of each used telescope, in the whole range of residual energies and for a wide range of charges, as usually observed in heavy-ion reactions.
Modifications to Eq. 4.4 are therefore needed, since data deviate from the expected behaviour for several reasons:

- when the residual energy becomes low, the atomic charge is no longer equal to Z;
- in experiments where the ion is stopped in a scintillator, the residual energy signal is not linear with the released energy;

- when ΔE is measured with a Silicon detector, the pulse height defect influences the Silicon detector response for high Z-values.

This formula performs a decoupling of the ΔE-E correlation at low, intermediate and high energies, by introducing some free parameters and a phenomenological term.

$$\Delta E = \left[gE^{\mu+\nu+1} + \left(\lambda Z^{\alpha} A^{\beta}\right)^{\mu+\nu+1} + \xi Z^2 A^{\mu} (gE)^{\nu} \right]^{1/(\mu+\nu+1)} - gE \tag{4.6}$$

where $\lambda, \alpha, \beta, \mu, \nu$ and $\xi$are free parameters, related to the characteristics and non-linear effects of the ΔE and E detectors, g accounts for the ratio of the electronic gains of the DE and E signals.

4.2.2 Identification procedure

The used identification procedure [28], consists of two steps:

- We sample on the ΔE-E scatter plot several points on the lines of well defined isotopes (He, Li, Be and B). In experiments, some isotopes can be easily recognized, due to their abundance (4He; 7Li; 11B) or separation from other masses (7Be; 9Be);Fig.4.3.

  The charge, mass, ΔE and E signals of the sampled points are put in a table. A minimization routine determines the parameters $g, \lambda, \alpha, \beta, \mu, \nu$ and ξ; giving the best agreement between the whole sample and the correlation provided for each A and Z by Eq. 4.6.

  The sum of the squared distances between the sampled and calculated values is minimized. This procedure is performed for each used telescope and a map is built containing the identification number of the telescope and its characteristic parameters $g, \lambda, \alpha, \beta, \mu, \nu$ and ξ

- We perform the event by event identification. In each event, each detected particle/ion is identified in mass and charge by a two-step process, by minimizing the distance of the measured ΔE and E signals with respect to the values provided

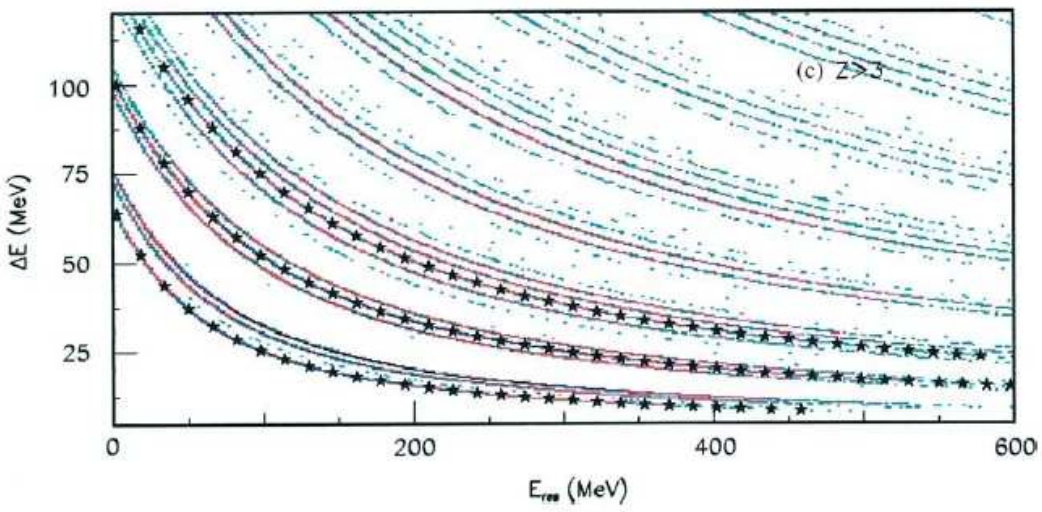

Figure 4.3: The sampled points used for the fitting procedure.

by Eq. 4.6 with the parameters $g, \lambda, \alpha, \beta, \mu, \nu$ and ξ read from the map built in the previous step. The two-dimensional vector (ΔE; E) is then replaced by the fourdimensional vector (ΔE;E;Z;A) for subsequent analyses.

To identify mass and charge of the detected charged products a two-step process is needed, since Eq. 4.6 is not analytically solvable. The first step is to find the charge Z (simply assuming A=2Z), by looking for the value of Z giving the shortest distance between the experimental ΔE and the energy loss given by Eq. 4.6 at the residual energy E. After the charge Z has been identified, the procedure is repeated, by solving Eq. 4.6 with respect to A (Fig.4.4.).

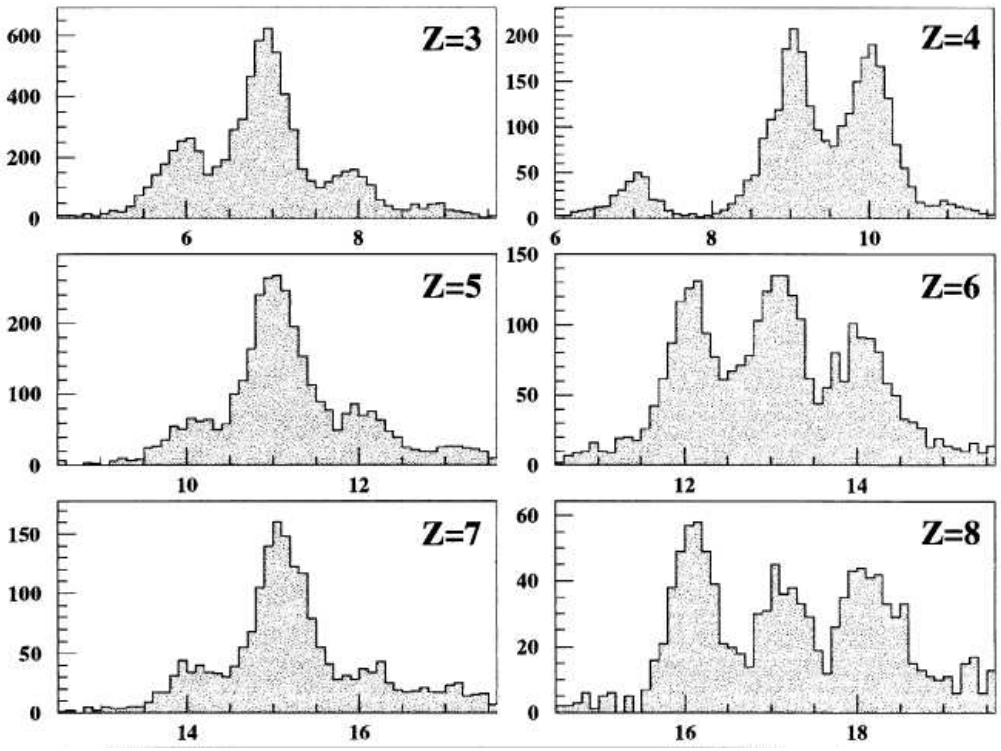

Figure 4.4: Experimental isotopic distributions obtained for charges 3-8.

4.3 LCP identification

CsI(Tl) scintillators are widely used to perfom Light Charged Particles (LCP) identification, as they emit light pulses whose shape varies as a function of the type of incident radiation. In fact, the CsI(Tl) crystal,when excited by an incident particle, produces light mainly in two different types of physical processes, resulting in two distinct light components (Fig.4.5),commonly named 'fast' and 'slow', reflecting energy deposited by the particle in the crystal, and also the particles species.
The light output of CsI(Tl) can be schematically described of two exponential components with different time constant:

$$L(t) = L_1 exp[\frac{-t}{\tau_f}] + L_2[\frac{-t}{\tau_s}] \tag{4.7}$$

where:

- L(t) the light pulse amplitude at time t;
- L_1, L_2 the light amplitude for the fast and slow components;
- τ_f, τ_s denote the decay time constant of the fast and slow components of the light pulse, respectively.

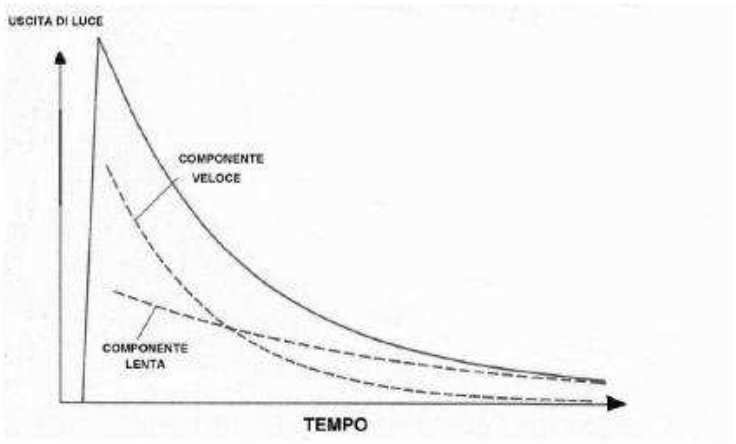

Figure 4.5: Pulse shape of charged particles in CsI(Tl)

This property of the CsI crystal is the basis of the pulse shape analysis. Knowing the combination of the two yield contained in the 'fast' and 'slow' components allows one to infer the species and the energy of the impimping particle.
Unfortunately, these yields cannot be measured directly, as the components in question overlap to a significant degree. However, their magnitudes can be reconstructed in a unique fashion, based on measured partial yields contained in characteristic 'time slices' of the scintillator signal. The identification scatter plot is then achieved by plotting the fast versus the slow component as shown in Fig.4.6.

4.3.1 Procedure

We recall hereafter the scheme of the usually employed procedures to identify (A,Z) isotopes, which do not rely on the brute force, even more time-consuming, ap-

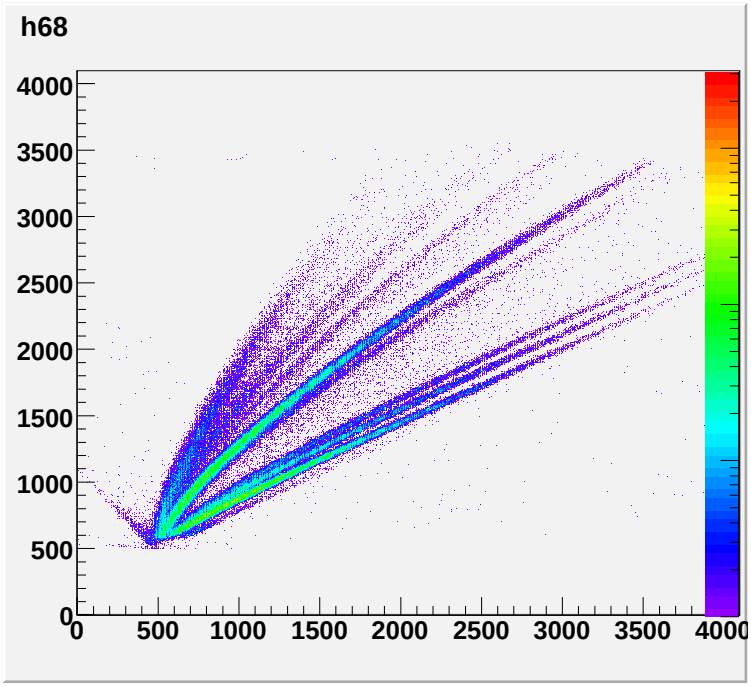

Figure 4.6: Pulse shape discrimination of light charged particles in CsI(Tl)

proach like graphical cuts. Two steps are normally necessary for each detector used in the experiment (for instance when the (A,Z) identification is performed through Fast-Slow [29] or via ΔE-E residual[28]):

- In a bidimensional scatter plot several points are by hand sampled on the ridges of well defined isotopes. Some isotopes can be easily identified by simple inspection, either due to their abundance (^{4}He) or their separation from other masses (^{1,2,3}H). Charge, mass and coordinates of the sampled points are organized in a table.

- The parameters characterizing the detector response to the charge (Z) and mass (A) are determined by fitting the coordinates of the previously sampled points. If an analytical[28], even empirical [22] function, describing one of the two variables as a function of the other does not exist, the set of points for a given isotope (A,Z) are fitted one by one via polynomial functions. The fit parameters are

stored in a table.

Clearly, in the case of a large number of detectors/telescopes, the most time consuming step of the identification procedure is the first one, because of the accurate sampling of a huge number of points on each isotope branch needed to obtain in the second step a reliable set of parameters. However, even the efforts to analytically link the employed variables are of great importance, to make it possible to identify isotopes which cannot be sampled, because of their low statistics (e.g. in backward-angle detectors). We show in Fig.4.7. the Fast-Slow bidimensional plots for one of the 24 azimuthal sectors of GARFIELD, as shown on-line by the Garfield data monitor [30].

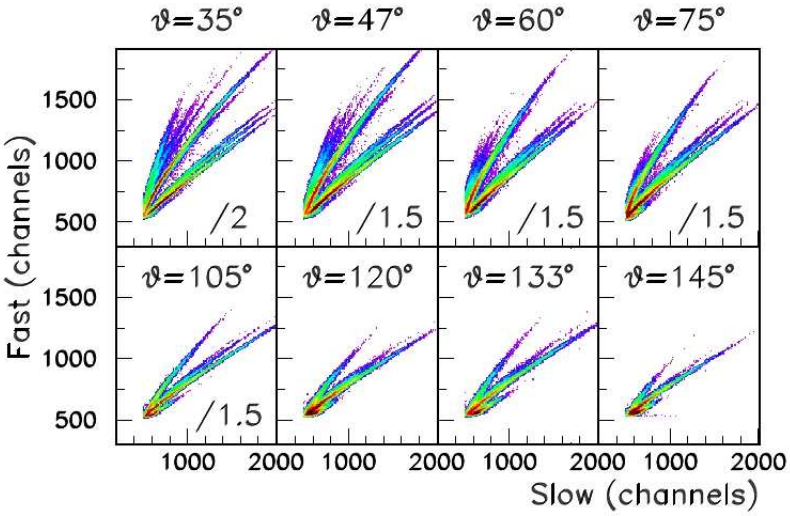

Figure 4.7: Fast-Slow bidimensional plots of a GARFIELD sector for the reaction ^{32}S + ^{58}Ni 16.5 AMeV incident energy.

In Fig.4.8 the 2-dimensional Fast-Slow histogram is show, lines visible in the histogram correspond to particles with different A and Z values. The ridge sequence of γ, p, d, 3H, 3He and α-particles can be easily distinguished, while other, more dispersed, ridges need to be more carefully studied.

The left-most, significantly wide correlations at small Slow values are due to the superpositions of heavy fragments, induced by the decrease of the decay time of the Fast signal [31].

With dedicated measurements of Li and C elastically scattered beams on Au target (superimposed as contours in the zoomed region) we have established that, in our energy regime, Li fragments, not isotopically resolved, are still distinguishable from the "cloud".

The ridge of Fig.4.8 between α-particles and Li fragments can be attributed to 2 α-particles impinging on the same detector.

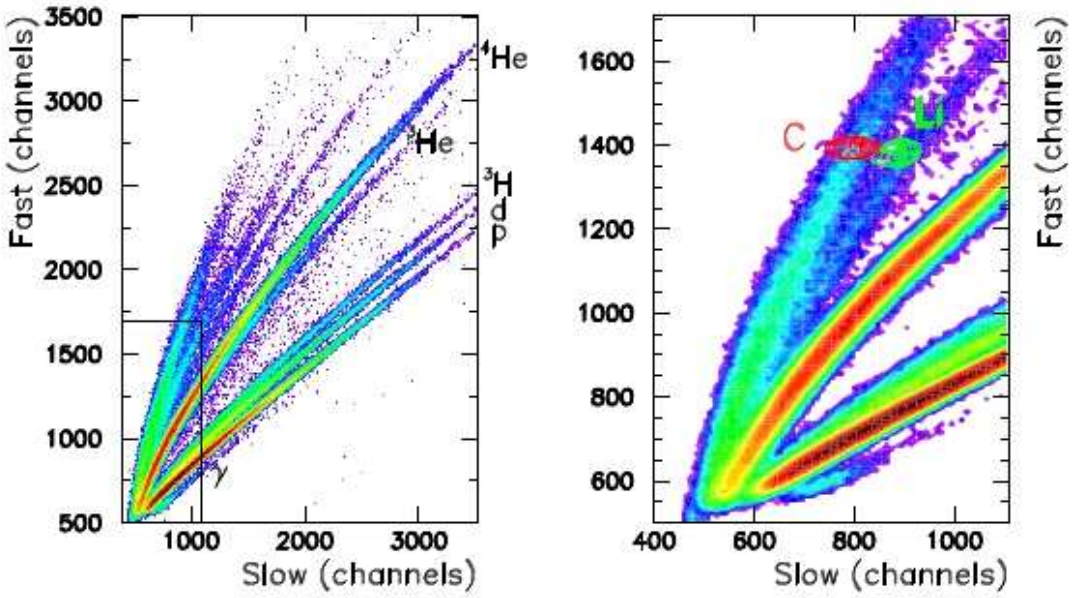

Figure 4.8: Fast-Slow 2d-histogram of a GARFIELD crystal placed at θ= 35°. In the right panel an expanded view is shown, corresponding to the rectangle of left panel.

A new “semi-automatic“ procedure have been therefore studied in order to make the identification of particles faster. The first step of procedure is the determination, within the ROOT environment, of representative sample points along the various ridges. Due to the structure of isotope ridges, which can be interpreted as successive monodimensional Gaussian distributions, very close to each other. Therefore we used the ROOT method Projection and the TSpectrum Class, to perform the peak search firstly along the X (Fig.4.9.) axis, then along the Y axis.

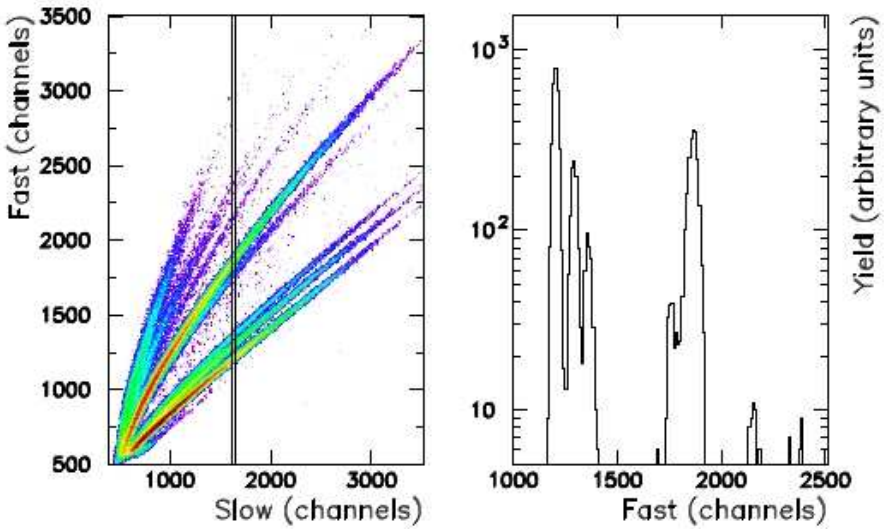

Figure 4.9: Fast-Slow bidimensional plot (left) and its Y-projection on Fast component (right) for the narrow channel window shown in the left panel.

Finally a peak observed on the Y projection is validated only if a peak in the X projection falls in the same cell of the bidimensional plot. This gives a series of coincident peaks, lying on the isotope ridges (Fig.4.10.).

At this stage coincident peaks falling on the isotope ridges need to be connected. A (A,Z) label has also to be assigned to each collection of connected peaks, from now on called a cluster. To do this, a tracking method has been used which automatically connects the peaks along each (A, Z) ridge. Tracking is essentially a local method of pattern recognition[32], here split in three components:

1. a method to generate track seeds (Fig.2 right panel), which are the starting points for the propagation procedure. The nature (A,Z) of these points is es- tablished at this step,

2. a parametric track model, which connects points of an isotopic ridge with a set of track parameters; in this case it is assumed a local linear equation between each pair of points along the ridge,

3. a quality criterion, which allows to distinguish good track candidates from ghosts. When several points are possible candidates to propagate a trajec- tory, the method selects the point giving the minimum change of the angular coefficient of the straight line connecting the previous two points belonging to the ridge.

This procedure is continued until the end of the tracking area has been reached, or no further suitable points can be found. Seeds are automatically chosen as the leftmost coincident peaks, allowing to connect all the other coincident peaks of a given isotope through the parametric track model.

To build an empirical, but analytical, function, we started from the consideration that a power law relation can been employed [34] for the total light output of a crystal as a function of the energy. In our case, due to the almost linear correlation between Fast and Long, we expect a power-law behaviour for both the Fast and the Slow variables as a function of the energy. This also implies a power-law relationship between the Fast and the Slow.

$$Slow(Fast, A, Z) = a_1 Fast^{a^2} (a_1, a_2 \geq 0) \tag{4.8}$$

To reach our goal of obtaining only one analytical function for all the observed isotopic species, we incorporated in Eq. 1 the exponential behaviors of a1 and a2:

$$\begin{aligned} a_1 &= [d_1 + d_2 \exp(-d_3 Z_{eff})] exp(-d_4 Z_{eff}) \\ a^2 &= [d_5 - d_6 \exp(-d_7 Z_{eff})] (d_i \geq 0, i = 1, 7) \end{aligned} \tag{4.9}$$

with $Zeff = (AZ^2)^{1/3}$, which represents the most effective way, within our approach, to take into account the charge and the mass of the analyzed isotope ridges.

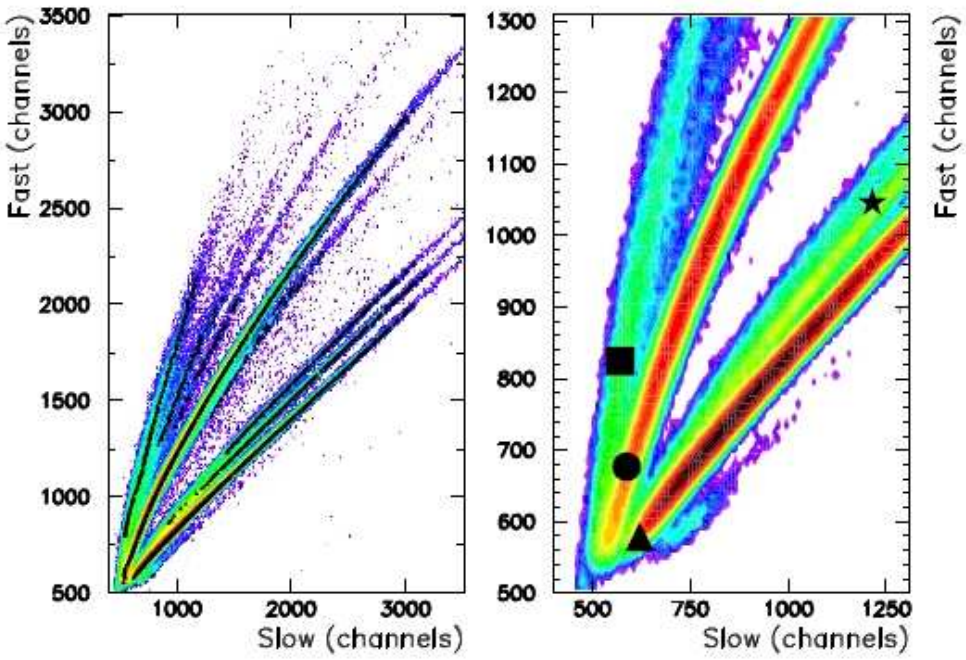

Figure 4.10: Left: Points along the various ridges, determined through the Projec- tion and TSpectrum procedure. Right: Seeds for protons, deuteron's, α-particles and IMFs (triangle, star, circle, square, respectively).

The last step of the analysis is the event by event identification procedure. By using the table of fit parameters of all the crystals, for each detected LCP the program estimates the distance of the experimental point (Slow,Fast) from the curve Slow(Fast,A, Z) of Eq. 1 for all the possible (A,Z) values. The shortest distance between the (Slow,Fast) point and each curve determines the appropriate assignment of Z (integer) and A (real) (Fig.4.12.).

The advantages obtained with the automatic calibration procedure may be summarized in the following points.

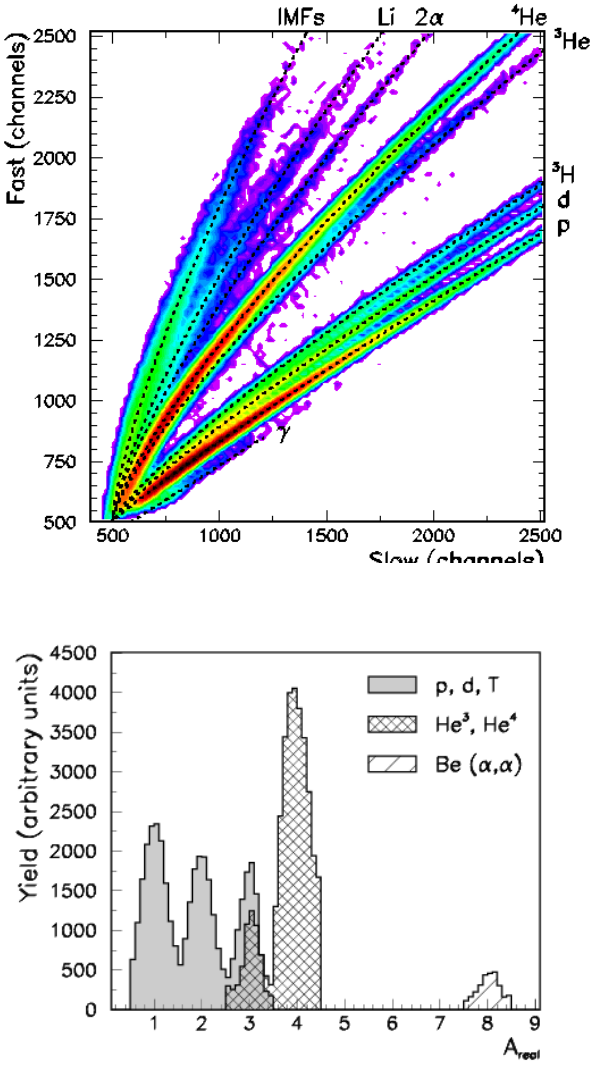

Figure 4.12: mass distribution

- The time dedicated to offline calibration is greatly reduced.
- The use of an analytical form of the Fast-Slow correlation Eq. 4.8 makes it possible the extrapolation to A-regions where graphical cuts are not easy to make, due to low statistics.

4.3.2 LCP energy calibration

The analytical function used to fit the sampled tracks has been derived starting from a power law relation suggested in Ref.[27] for the total light output as a function of the energy.

This is shown in Fig.4.13. where the signals obtained in a previous measurement for a "reference crystal" [22] are plotted as a function of the energy for ions identified through a ΔE-E technique, exploiting a silicon detector in front of the crystal as ΔE. Fig. 4.13 shows also the elastically scattered ^{7}Li and 12^{C} on Au targets.

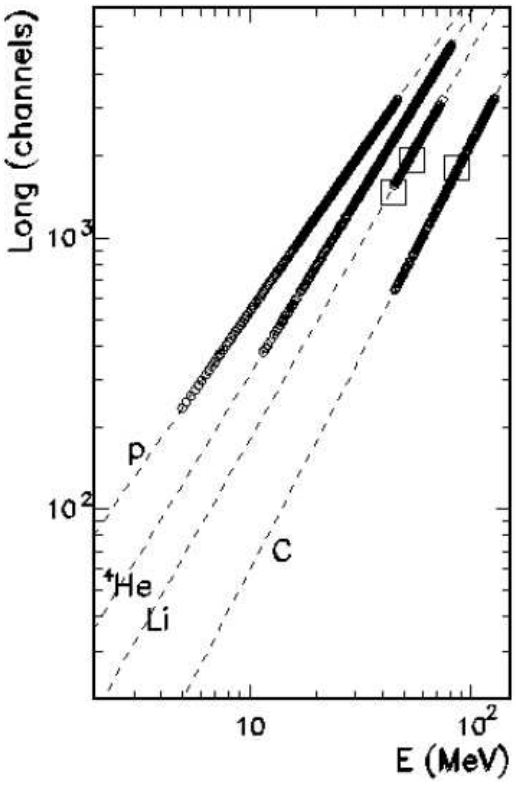

Figure 4.13: Light output as a function of the energy for p, d, 4He, 7Li and 12C isotopes of a reference crystal The center of the squares correspond to elastically scattered beams of ^{7}Li and 12^{C} on Au targets, measured with the GARFIELD crystal of these measurements.

The behavior is well described as a power law, though some deviations are present at low energies. It is easy to show that also the slow component can be assumed as dependent on the fast through a power law and this is verified in Fig.4.13 where the slow component is plotted against the fast in a double logarithm scale.
We have therefore used the energy calibration obtained as a consequence of the fit of the light output to get energy distribution of light particles emitted in a $^{32}S + ^{58}Ni$ measurement at 16.4 AMeV.
The results are shown in Fig. 4.14 and the obtained distributions are typical of a statistical decay (so called maxwellians).

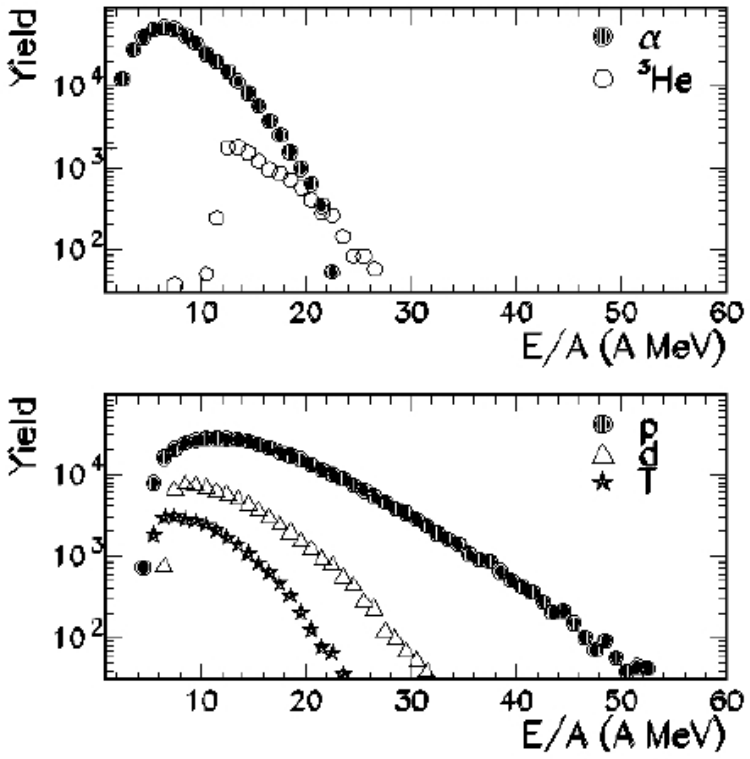

Figure 4.14: Energy distributions for Z = 2 isotopes (top panel) and Z = 1 isotopes (bottom panel).

4.4 Global Experimental Observables

A basic global variable is the event charged particle multiplicity (Nc). The multiplicity represents the number of particles emitted in each event and could be related to the violence of the collision (centrality of the collision). From the experimental point o view the total detected multiplicity depends on the angular coverage of the apparatus. Another global variable that characterizes the events is the charge distribution of the reaction products i.e. the relative yield of the different charges emitted in the reaction. The charge distribution can give qualitative information on the reaction mechanism. An important quantity, related to the charge of the fragments, is the sum of the detected charges (Z_{tot}), which gives information on the efficiency of the apparatus. In fact, as the sum of the charges in the entrance channel is known ($Z_{tot} = Z_{Projectile} + Z_{Target}$), it is interesting to study the response of the apparatus with respect to the collection of the emitted charged particles, i.e. to the reconstruction of the event. In general, global variables reflect the efficiency of the apparatus so that particles with an energy lower than the detector thresholds or emitted in an angular polar range not in the apparatus geometrical acceptance, cannot be included in the considered global variables (multiplicity, total charge, etc). Another particle multiplicity can be constructed taking into account only the intermediate mass fragments (IMF), i.e. fragments with a charge $Z \geq 3$. A further global variable that can be built in order to get information on the centrality of the collision is the transverse energy. This is defined as the kinetic energy calculated considering only the component of the velocity perpendicular to the beam axis. The sharing of the incident kinetic energy of the projectiles in a perpendicular direction is frequently interpreted as an indication of the centrality, or dissipation, of the collision. In fact, the more central is the collision, the higher the transverse energy, inducing to define the transverse energy as an indicator of the loss of the entrance channel memory. In addition, for low values, the transverse energy can be considered a linear function of the impact parameter, thus allowing an impact parameter selection.

The total transverse energy is thus defined as

$$E_{trans} = sum_{i=1}^{Ntot} \frac{(\vec{p_i} \cdot \vec{k_i})^2}{2m_i} = \sum_{i=1}^{Ntot} E_i sin^2\theta_i \tag{4.10}$$

where p_i, m_i, E_i represent respectively the momentum, the mass and the kinetic energy of a reaction product, θ_i the emission polar angle and k_i the beam direction. The sum is extended to all products emitted in each event.

The total impulse along the beam axis (qz) and the velocity of the biggest fragments (V_{Zbig}) are other observables that are correlated with the impact parameter. For example qz, in the central collisions, has values around the velocity of the center of mass of the system, while for peripheral collisions qz is approximately close the velocity of the beam.

To sort the measured events as a function of the centrality, we adopted the method of the "shape analysis" [36], common to other intermediate and high energy experiments performed with $\simeq 4\pi$ detectors [37, 38].

To investigate the fragment emission patterns one has to build the momentum tensor[36]:

$$T_{ij} = \Sigma \frac{p_i^{(n)} \cdot p_j^{(n)}}{p^{(n)}} \quad (i, j = 1, 2, 3) \tag{4.11}$$

where $p_i^{(n)}, p_j^{(n)}$ are the $i-th$ and $j-th$ Cartesian projections of the momentum $\vec{p}^{(n)}$ of the $n-th$ fragment in the center of mass frame. The sum runs over the number of charged products with ($Z \geq 2$) detected in each event. The diagonalization of this tensor gives three eigen-values λ_i and three eigen-vectors $\vec{e_i}$. The event shape is an oriented ellipsoid with the principal axes parallel to the eigen-vectors.

The flow angle θ_{flow} is defined as the angle between the eigenvector $\vec{e_1}$ for the largest eigenvalue λ_1 and the beam axis $\hat{u}_3$:

$$cos(\theta_{flow}) = \vec{e_1} \cdot \hat{u}_3 \tag{4.12}$$

In order to perform the shape analysis it is necessary to select events where a considerable amount of the incoming momentum has been detected. Then the inspection

of the correlation between the total detected charge and the flow angle will allow to separate central and peripheral events. The flow angle is indeed a variable sensitive to the the dynamics of the fragmentation process. Specifically, the emission of fragments from a unique source should be on the average isotropic in momentum space and the flow angle should have a flat distribution. Conversely in peripheral reactions the forward-backward emission of fragments from the spectator-like sources should lead to an event shape elongated along the beam axis and a flow angle peaked in the forward direction.

Chapter 5

Data selection and HIPSE event generator

One of the most difficult issues in the study of the heavy ions collisions around the Fermi energy domain is related to the fact that this energy region is a transition region. Indeed one has to deal with a mean-field dominated dynamics (much below the Fermi energy) and a high-energy regime where individual nucleonic degrees of freedom and associated two-body effects become predominant [12].

This competition between mean-field effects and in-medium nucleon-nucleon interactions is a long-standing problem in heavy ion reactions around the Fermi energy and has led to two classes of models. The first one starts from the mean field and extends this latter to account perturbatively for the residual two-body interaction, while in the second class of models, the two body interaction is treated exactly and mean-field effects play a secondary role.

Intra-nuclear collision and molecular dynamics models are the prototypes of this second class. For heavy-ion collisions, it has been shown that the transition between mean-field and nucleon nucleon degrees of freedom is smooth and both should be accounted for at the same time to properly reproduce experimental data. Special attention should thus be paid to the interplay between preequilibrium and postequilibrium

effects.

5.1 Heavy-Ion Phase-Space Exploration model

The Heavy-Ion Phase-Space Exploration model is a dynamical model to account for light as well as massive cluster emission during the reaction. This model naturally accounts for the transition between nucleonic and mean-field effects. It properly connects the preequilibrium stage with the deexcitation phase, introducing the important notion of phase-space exploration during the reaction.

Let us take multifragmentation, defined as the emission in a very short time scale of several species of atomic number larger than 2 [39] as compared to other decay mechanisms such as the formation of heavy residues or fission. Such a phenomenon is expected to be the ideal tool to study the transition from a liquid-like state (nuclei at normal density) toward a gas-like state associated with the vaporization of the system. The quest for the signals of a nuclear phase transition of the liquid-gas type has led to rather sophisticated analyses.

The experimental analysis based on nuclear calorimetry has claimed evidence for a liquid-gas phase transition through the study of various signals. Some of the analyses make extensive use of the thermal multifragmentation statistical models to prove the existence of thermal equilibrium. There are however some uncertainties in using statistical models. This is due to the lack of knowledge of dynamical effects, in particular, of the fast early processes which could lead to the formation of equilibrated systems. In particular, the phase space explored during the collision is expected to be sensitive to the initial conditions of the reaction. Such a point is addressed in microscopic transport models.

These models provide a suitable framework for the description of nuclear collisions at intermediate energies and are able to describe dynamical effects. Unfortunately, although nucleon nucleon collisions are included, one can not determine if the system has reached a complete thermal equilibrium.

Moreover, there is not a direct link in such approaches between the outputs of the simulations and the thermodynamical properties of the excited species produced in the reaction. As a consequence, these models do not give unambiguously important quantities required for statistical model calculations. For instance, internal excitation energies of the created fragments cannot be easily obtained in current microscopic calculations.
The HIPSE model [40] has been developed to find a link between the two extreme approaches, described above, namely the statistical approach based on the reduction of the reaction to a few important parameters and the microscopic approach based on the transport theory.

5.1.1 Main characteristics of the HIPSE model

This model consists in three main steps. In the first step, namely approaching phase, the two partners (Projectile and Target) of the reactions are at maximum overlap. This phase is considered by solving the classical equation of motion of the two partners in their mutual interaction potential.
The difficulty met in microscopic theories is that the potential part of the energy does not separate from the possible internal excitation or from the kinetic part in the collective space. The difficulty can be removed in two limiting approximations:

- in the frozen density approximation, it is supposed that the collision is sufficiently fast so that the internal degrees of freedom do not have time to "reorganize" themselves. In that case, the concept of di-nuclear system persists even in the limit of overlapping target and projectile densities. It thus neglects the Pauli principle as well as the saturation properties.

- the adiabatic approximation limit assumes in an opposite way that internal degrees of freedom reorganize much faster than the collective degrees of freedom.

In that case, the notion of two separate densities looses its meaning and one should treat instead a single entity that undergoes a transition from large deformation toward a compact shape.

For a given beam energy E_B, a classical two-body dynamics during the phase of approach of the collision is assumed. Noting $V_{A_TA_P}$ ($r = |r_T - r_P|$) the interaction potential between the target and the projectile, we consider the evolution associated with the Hamiltonian $E_0 = p^2/2\mu + V_{A_TA_P}(r)$,where $E_0 = [A_T/(A_T + A_P)]E_B$ is the available energy in the center of mass while **p** is the relative momentum and $\mu = m_T m_P/M$ is the reduced mass with m_T and m_P the target and projectile mass, respectively. The concept of nuclear potential is rather unambiguously defined when the two nuclei are well separated. When the relevant observable is reduced to the minimal geometric information on the two nuclei in interaction (i.e. their nuclear radius only), the proximity potential is used

The energy dependence of potential can be understood by considering the two limiting approximations used to describe the nucleus-nucleus potential in fusion reactions: the adiabatic and the sudden approximations (see [41]).

At very high relative energy, neglecting the influence of two-body collisions, the internal degrees of freedom have no time to reorganize and the system has a strong memory of the initial conditions. As the beam energy increases, the internal degrees of freedom have less time to reorganize and the potential is expected to be sharper. The possible energy dependence of the potential has been included in a phenomenological way. Hipse model use a simple approximation for the construction of the potential. First, it is assumed that $V_{A_TA_P}$ depends on r uniquely even for small relative distances. In order to obtain the potential for $r < R_T + R_P$, we interpolate the potential between $r = 0$ and $r = R_T - R_P$ using a third-order polynomial and assuming continuity of the derivative of the potential at each point. The value retained at r = 0 is conveniently expressed as

$$V(r = 0) = \alpha_a V^{Froz}_{A_TA_P}(r = 0) \tag{5.1}$$

where α_a is a parameter to be fixed by comparison with experimental data.
$V^{Froz}_{A_T A_P}$ is the energy of the system assuming that the two densities of the system overlap completely in the frozen density approximation.
The second step in the model is the partition formation phase which corresponds to the rearrangement of the nucleons into several clusters and light particles (this rearrangements is hereafter called the partition) according to the impact parameter of the reaction. The partition is built following coalescence rules in momentum and position spaces.
The main consequence of this approximation is that the characteristics of the species produced in highly fragmented collisions will exhibit kinetic energy and angular distributions keeping a strong memory of the entrance channel.
The last phase is the exit channel and after-burner phase up to the detectors: the partition is propagated taking into account explicitly reaggregation effects due to the strong nuclear and Coulomb interactions among the various species of the partition. Since these latter are produced in excited states, secondary decays are taken into account by means of an evaporation code.

5.2 Comparison with experimental data

The model described above is now compared with experimental data taken by NUCLEX Collaboration at the LNL facility (see chapter 2.3).
In order to test the model is necessary to perform a first data selection. To sort the measured events as a function of the centrality, we adopted the method of the "shape analysis" [36], common to other intermediate and high energy experiments performed with $\simeq 4\pi$ detectors [37, 38].
To do this it is necessary to select events where a considerable amount of the incoming charge and momentum has been detected (most complete events).

A first selection of events is presented in Fig. 5.1. Asking that at least 50% of

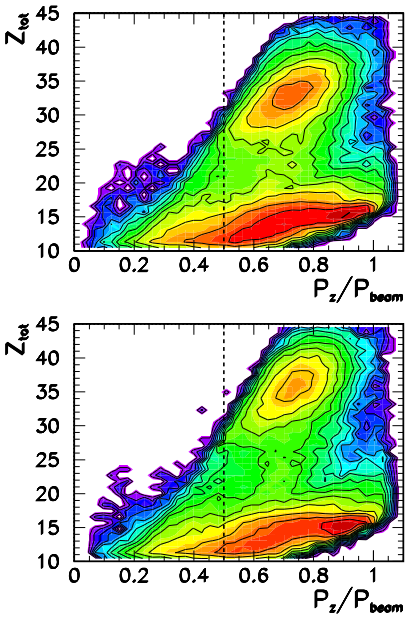

50

Figure 5.1: Total detected charge as a function of the total longitudinal momentum normalized to the projectile momentum for $^{32}S + ^{58}Ni$ (upper part) and $^{32}S + ^{64}Ni$ (lower part).

the total incoming parallel momentum is collected (dashed lines) allows to keep events with two distinct values of the total detected charge: the higher bump corresponds to an average detected charge about 80% of the total charge, the lower one corresponds to the detection of the quasi projectile ($Z = 16$), being the quasi-target and its products non detected because of the energy thresholds. On the left of the dashed line corresponding to our first selection, lie events poorly detected from the point of view of the total detected charge and total detected linear momentum. In the following we analyze events under the condition $P_z \geq 0.5 \cdot P_{beam}$.

A convenient observable to address the kinematics and the topology of the reaction is the bidimensional correlation between the atomic number and the parallel velocity of

all emitted fragments as displayed in Fig. 5.2. The general trends of the experimental data are reproduced by the simulation.

Fragments with atomic numbers close to the projectile exhibit velocities close to the beam velocity as expected.

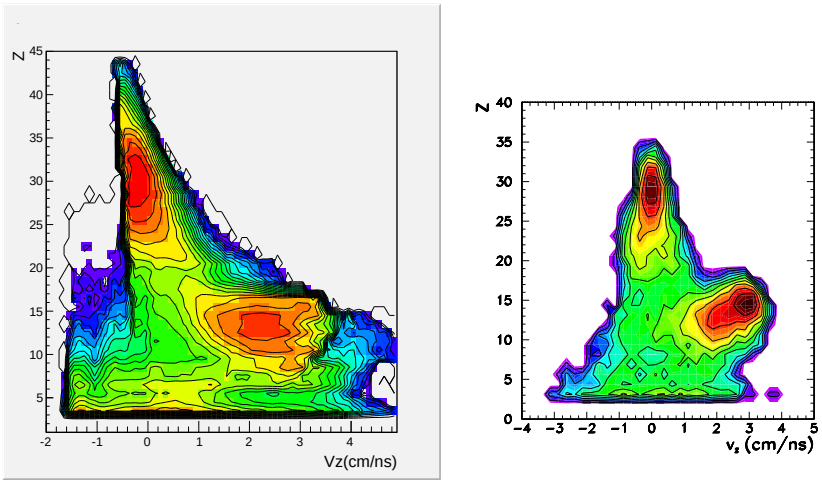

Figure 5.2: Three-dimensional plots (in log scale) $v_{//}-Z$. Left panel is for experimental data while right panel is for simulated data. Only fragments with atomic numbers larger than or equal to three are included in the figure

By examining now the behaviour of the total detected charge as a function of the "flow angle" (see section 4.4), corresponding to different sphericity of the events, we observe [panel a) of Fig. 5.3] that peripheral events keep a strong memory of the entrance channel and are therefore restricted to low values of the flow angle and a total detected charge close to the projectile charge. The average calorimetric energy for these events is 1.5 AMeV.

Higher values of the total charge are distributed over the whole range of θ_{flow} with nearly constant statistics, which implies a nearly flat distribution of $cos(\theta_{flow})$, as expected for spherical events.

Hereafter we will define "'central"' events with the condition of a total detected charge $Z_{tot} \geq 70\% \cdot Z_{S+Ni}$, and "'peripheral"' events by $Z_{tot} \leq 25$ and $\theta_{flow} \leq 40^o$.

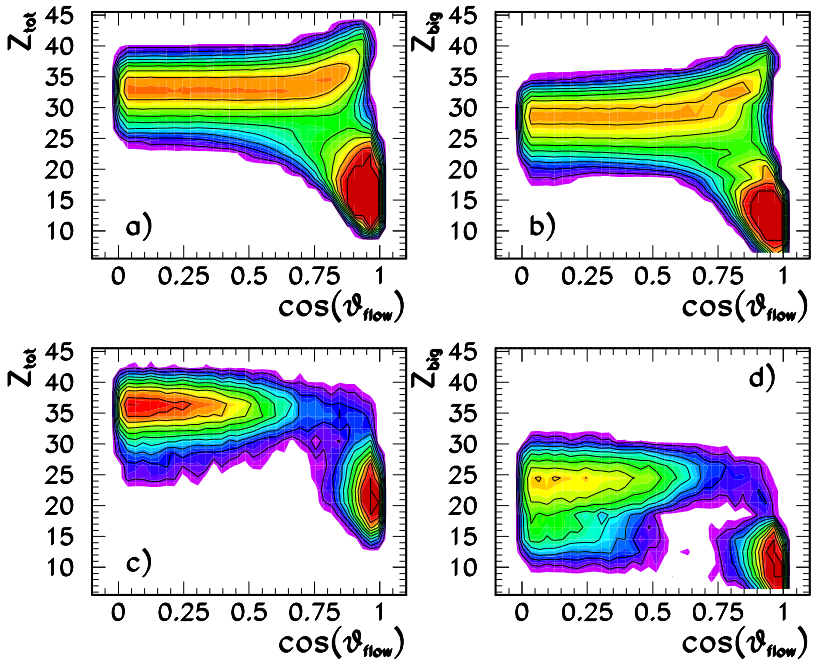

Figure 5.3: Total detected charge and charge of the largest fragment as a function of the cosinus of the flow angle for ^{32}S +^{64} Ni under the condition: $P_z/Pbeam \geq 0.5$. Upper part (panels a), b)): all events. Lower part (panels c),d)): events with at least three detected IMF's.

A first glimpse on the topology of the events can be inferred from panel b) of Fig. 5.3, which displays the correlation between the flow angle and the heaviest cluster measured in each event. We can see that for $\theta_{flow} \leq 30^o$ the largest cluster has a charge close to the total charge, as expected from an evaporation residue. For increasing θ_{flow}, we observe a decrease of the size of the largest fragment.

The lower part of Fig. 5.3 shows that the evaporation phenomenon coexists with multifragmentation for the most dissipative collisions characterized by values of the "flow angle" larger than about 60^o [37]: a non-negligible fraction of well measured events corresponds to nearly equal-size 3-fragments ($Z \geq 3$) events. The average calorimetric excitation energy for the events with $\theta_{flow} \geq 60^o$ is 3 A MeV, very close to the total centre of mass available energy. Calculations performed for our reactions with the dynamical code Hipse[40] confirm (Fig. 5.4) that the sorting of events in intervals of θ_{flow} correspond to a classification in terms of impact parameter, due to the monotonic relationship between these two quantities.

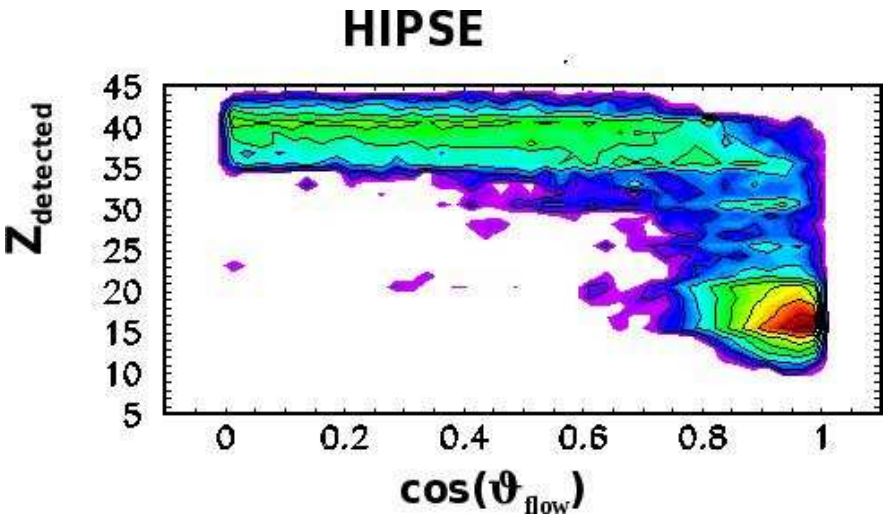

Figure 5.4: Simulated data. Total detected charge and charge of the largest fragment as a function of the cosinus of the flow angle for $^{32}S + ^{64}Ni$.

Some three fragment events are also associated to peripheral binary collisions, where the deposited energy does not allow to overcome the multifragmentation threshold. The fact that the distribution of the largest fragment is not sensitively affected by the IMF multiplicity indicates that fragments emitted by the target, possibly in a dynamical neck-like rupture, are detected sometimes together with the quasi-projectile source[42].

Chapter 6

Data analysis

6.1 Charge distribution and odd-even effects

In the previous chapter we have divided the events into two classes: central and pheripheral events. In the first case the evaporation phenomenon coexists with multifragmentation for the most dissipative collisions; the average calorimetric excitation energy for the events with $\theta_{flow} \leq 60^{\circ}$ (see section 4.4) is 3 A MeV.
The peripheral events keep a strong memory of the entrance channel and are therefore restricted to low value of the θ_{flow} angle and a total detected charge close to the projectile charge. The average calorimetric energy for these events is 1.5 A MeV.

Figure 6.1 shows the charge distributions measured for the two reactions in peripheral (right part) and central (left part) events. The superposition of the two peripheral data sets corresponding to the different targets ^{58}Ni and $64Ni$ shows that our selection on peripheral events is effective in isolating the contribution of the quasi-projectile; a different behavior is observed in central collision, where the charge distribution does not scale with the size of the system and a clear isospin effect can be seen: the source with the higher N/Z ratio (open symbols) leads to a more prominent U-shape charge distribution. This can be intuitively understood considering that a high N/Z ratio of the

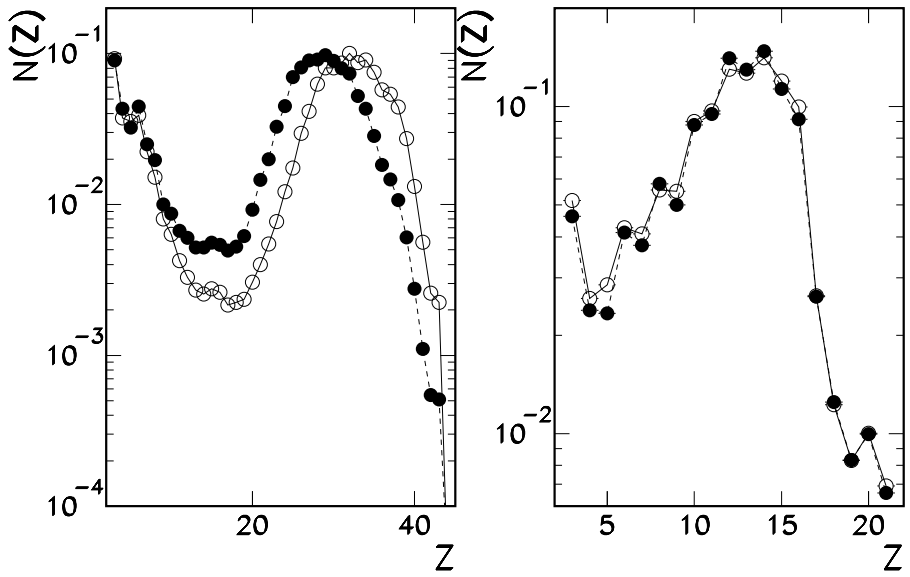

Figure 6.1: Elemental fragment (Z>2) distribution for $^{32}S + ^{58}Ni$ (full symbols) and $^{32}S + 64^{N}i$ (open symbols). Left: all central events, without selection on the multiplicity. Middle: central events with at least three IMF (Z>2) detected. Right: peripheral collisions.

source favors the production of large clusters, since such clusters are in average more neutron rich. Therefore partitions consisting of a large heavy residue dominate. When the N/Z ratio is low (full symbols), the probability for a large cluster to survive is small and the system can decay into IMFs, which are typically symmetric in N/Z.

6.1.1 Staggering

Odd-even effects have been studied since a long time and never quantitatively understood. The odd-even anomaly was reported in the literature [45, 43] to be more pronounced in reactions involving Ni projectile and targets, in particular in n-poor sys-

tems, while in experiments involving Ca projectile and targets it was not observed up to the advent of experimental devices with very good accuracy of Z-identification [44].

As far as staggering is concerned, we can see that for both reactions a well pronounced odd-even effect is seen in the charge distribution of peripheral collisions, while almost no staggering is apparent neither in the IMF yield (coming mainly from fusion-multifragmentation) nor in the residue region (coming from fusion-evaporation) for central collisions, where only the extra-production of Carbon fragments is evident. This behavior has already been observed in many other reactions at low and intermediate incident energies, for central collisions [46, 47, 48, 49]. In almost all the experiments quoted in Ref.s [45, 43] the experimental samples correspond mostly to peripheral collisions or to fission-fragment charge distributions. To our knowledge, no staggering has been directly observed in charge distributions for carefully selected central collisions. Evidence of the staggering in central collisions comes out by looking at the ratio of the charge distribution of the neutron-poor reaction by the neutron-rich one [47]. In this way, however, the absolute value of the even-odd staggering for each reaction is lost.

The difference between central and peripheral collisions indicates that the most important variable governing the staggering is either the isotopic ratio of the evaporating source, which is sensibly more neutron rich for the fused sources than for the quasi-projectile, or the excitation energy, which corresponds to 3 A.MeV in average in the central sample and less than half of this value for the peripheral sample, which can produce fragments with a different mechanism. To clarify these ipotheses, we build the fragment charge distribution for events out of the central sample, characterized by only two detected fragments and a small θ_{flow} range ($< 30^o$). In agreement with other experimental results [50, 51] the even-odd staggering is apparent, slightly more pronounced in the neutron-poor reaction (see Fig. 6.2). To deeply inspect the yield oscillations in peripheral and central events, we calculated the ratio of the elemental charge distribu-

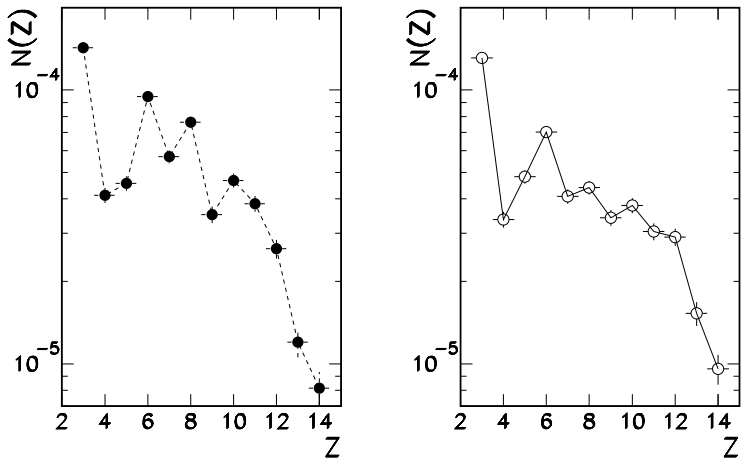

Figure 6.2: Elemental fragment ($Z \geq 3$) distribution of the lightest fragment for central events with fragment multiplicity equal to 2. $^{32}S + ^{58}Ni$ (left) and $^{32}S + ^{64}Ni$ (right). Lines are drawn to guide the eye.

tions by the smoothed ones, obtained by a parabolic smoothing of 5 consecutive points of Fig. 6.1. By looking at Fig. 6.3 it is evident that the staggering is present also in central collisions with amplitudes similar to the peripheral ones. Some differences are apparent in this representation: the extra-production of the Carbon with respect to oscillations of neighboring charges is larger in central collisions and the amplitude of the ratios decreases for increasing fragment charge, at difference with peripheral events, where it remains almost constant.

In both cases the different isospin of the entrance channel plays a minor role, enforcing the idea that a different kind of decay is the origin of the observed fragments.

A possible way of discriminating between these two hypothesis would be to analyze data in excitation energy bins, but the statistics of the present data-set is not sufficient. However we will have insights on this issue from model calculations in the next chapter.

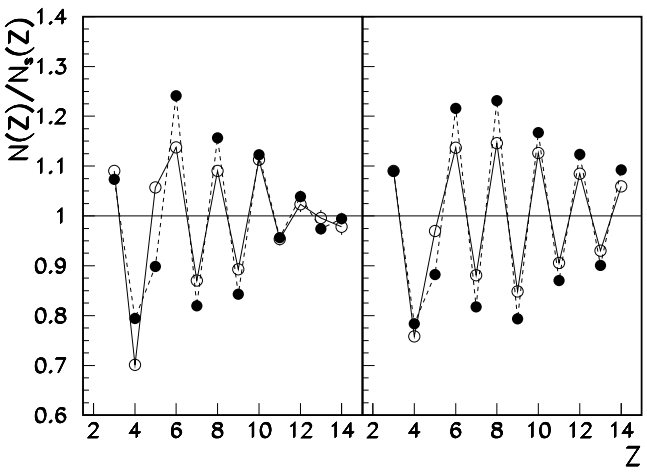

Figure 6.3: Top panels: Ratio of the elemental fragment ($Z \geq 3$) distribution of Fig.6.1 for $^{32}S + ^{58}Ni$ (full symbols connected by dashed lines) and $^{32}S + ^{64}Ni$ (open symbols connected by full lines) by the smoothed distributions. Left: central events. Right: peripheral collisions. Lines are drawn to guide the eye.

Before coming to more complex analyses, let us look at some preliminary observations on the behavior of staggering. The elemental distribution is displayed in different isotopic chains in Fig. 6.4.

A clear odd-even effect is only apparent in the case $N = Z$ and $N = Z - 1$, where some odd-even fluctuations appear superposed to a global trend which is largely determined by the non-monotonic behavior of the inclusive mass distribution, as shown in Fig. 6.1. To disentangle the two effects and better evidence the isotopic behavior, it may be useful to normalize the measured yield of each isotope to the total detected yield for the considered element. This normalized distribution, defined as:

$$P(A) = \frac{Yield(A,Z)}{\sum_A Yield(A,Z)} \tag{6.1}$$

is presented in the left panels of Fig. 6.5 for the two reactions.

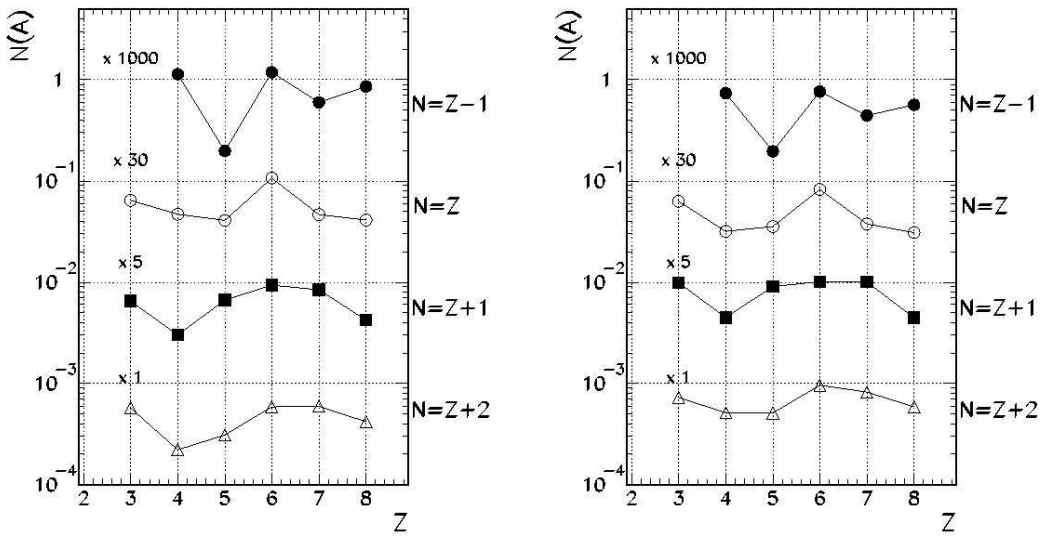

Figure 6.4: Elemental distribution of IMFs for $^{32}S + ^{58}Ni$ (left) and $^{32}S + ^{64}Ni$ (right) for peripheral collisions corresponding to different isotopic chains.

The behavior of the $N = Z$ yields is not modified by this procedure, while odd-even effects appear more clearly for the other isotopic chains, that correspond to lower cross sections and are therefore more affected by the U-shape of the inclusive size distribution.

As proposed by Ricciardi et al.[43], the observed trend is qualitatively compared to the behavior of the lowest particle emission threshold, i.e. the lowest between the proton and neutron separation energies of the final daughter nucleus. In agreement with FRS data, the behavior of the isotopic distributions is qualitatively similar to the behavior of the lowest separation energy, suggesting that the last (neutron or proton) evaporation step is indeed at the origin of the observed staggering. An exception is given by the $N = Z + 2$ isotopic chain, which shows an inverse staggering with respect to the interpretation based on separation energies.

This interpretation moreover requires that the last evaporation step is completely

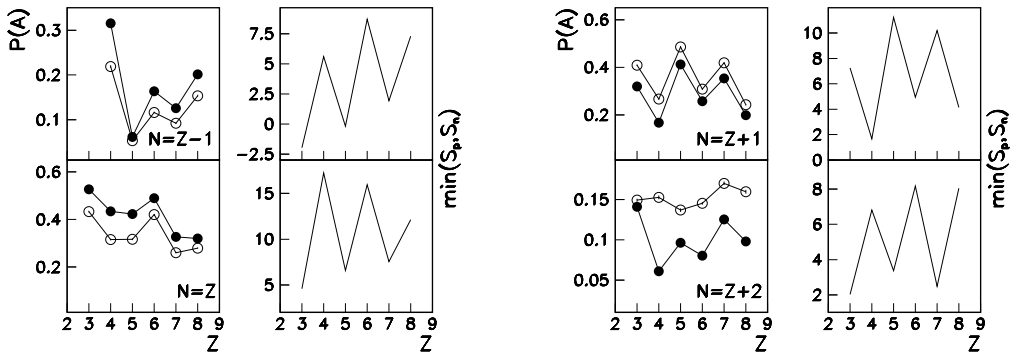

Figure 6.5: Normalized distribution of IMFs for $^{32}S+^{58}Ni$ (full symbols) and $^{32}S+^{64}Ni$ (open symbols) for peripheral collisions corresponding to different isotopic chains. For each reaction, the panels on the right show the corresponding behavior of the fragment lowest nucleon emission threshold (see text).

dominated by the competition between proton and neutron emission. This is clearly not the case for the ^{8}Be yield, which has been reconstructed through $\alpha-\alpha$ correlations, and the same may be true for other isotopes. To have a more global view of the issue, Fig. 6.6 displays the Q-values for neutron, proton and alpha decay for the different isotopic chains.

From this figure we can see that the lowest Q-value for the $N = Z$ chain always corresponds to α-decay (with the only exception of ^{14}N), and this quantity does not show any oscillating trend as a function of Z for all the other considered isotopes. The position of the first particle-unstable excited level of the parent nucleus is also shown in Fig. 6.6, and nicely coincides with the lowest Q-value.

Looking at the position of the first excited level for $N = Z + 1$ nuclei we can formulate another interesting consideration: in this case even-Z nuclei in their first excited level decay by n emission, and the corresponding daughter are even-Z $N = Z$ isotopes, while odd-Z nuclei decay mainly by α emission (with the exception of ^{15}N),

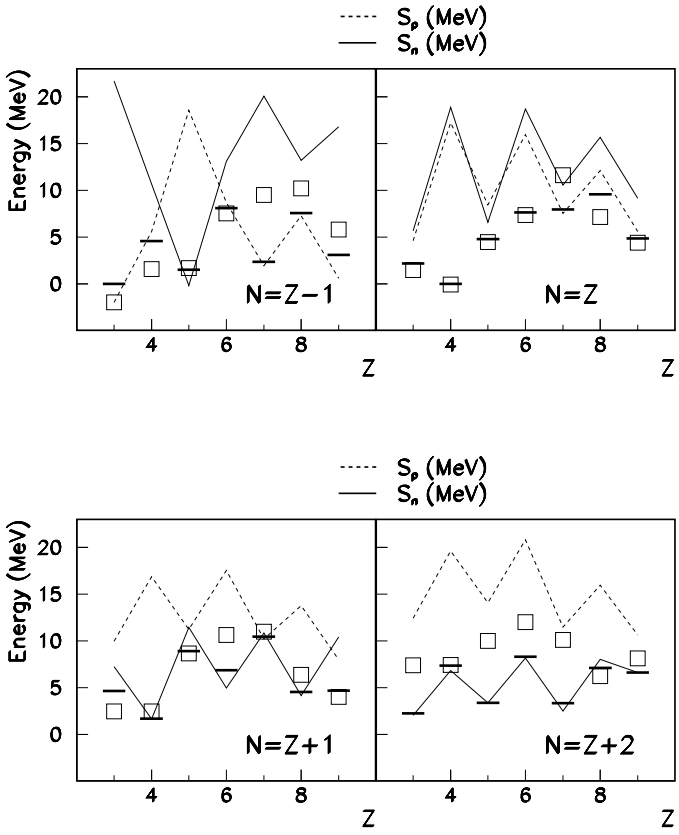

Figure 6.6: Comparison of the energy of the lowest unstable state (thick lines) decaying in a given daughter isotope, with the Q-value for alpha decay (open squares) and the neutron (S_n) and proton (S_p) separation energies

corresponding to daughters with odd-Z and of the same $N = Z + 1$ class. Moreover, since the first excited level for even-Z nuclei lies at a lower energy with respect to the first level of odd-Z ones, we could say that even-Z nuclei are produced in their excited levels with a higher probability. Being the decay from this level decided in a quasi-deterministic way by energy thresholds, the higher probability for the excitation of the first level in ^{9}Be, ^{13}C and ^{17}O as parent nuclei translates into an increased yields for ^{8}Be, ^{12}C and ^{16}O daughter, which is seen in the data.

In the case of $N = Z + 2$ parent nuclei the energy position of the first excited level follows exactly the trend of $min(S\,n; S\,p)$, and, with the exception of 18^{O}, all the levels are unstable against n-emission. This means that, considering parent nuclei of the type $N = Z + 2$, their daughters would be all $N = Z + 1$ nuclei. Moreover, since the levels of even-Z nuclei lie higher in energy with respect to the odd-Z ones, we expect an increase in the yield of odd-Z $N = Z + 1$ nuclei, which is seen in the data. As far as $N = Z + 2$ daughter nuclei in the final yields are concerned, the interpretation of Fig. 6.6 is not so straightforward. Nuclei of this kind could come for instance from the proton decay of $N = Z + 1$ nuclei with excitation energies higher than the one corresponding to the first excited state. In this case the proton separation energies for $N = Z + 1$ show an oscillation coherent with the oscillation of the measured $N = Z + 2$ yields, under the hypothesis of a lower probability for an excitation at an higher energy. But $N = Z + 2$ nuclei could also come from the α-decay of nuclei of the same $N = Z + 2$ class: in this case no oscillating trend is observed for the Q-value for α-decay, but the alpha-decay threshold for Z = 6 is higher than the one for the neighbouring nuclei, suggesting an underproduction of Z = 6 nuclei of the class $N = Z + 2$. The same holds if we consider $N = Z + 2$ nuclei as daughter of the neutron decay of $N = Z + 3$ parents.

Finally, the case $N = Z - 1$ of Fig. 6.6 shows that the lowest Q-value for the first particle-unstable excited level of parent nuclei corresponds to α-decay, with the exceptions of ^{13}N and ^{15}O, which decay by emission of a proton and a daughter fragment with $N = Z$, increasing the yield of $N = Z$ nuclei, observed in the data.

Concluding, the presence of staggering in the final measured yields can be linked

to the population of the parent nuclei at the previous steps of the decay chain and can not be fully explained by the behavior of the lowest particle emission threshold of the final daughter nuclei. This is the reason why we propose to study correlation functions of isotopically resolved pairs, which allows us, at least in some selected cases, to reconstruct the primary yields of decaying nuclei.

To clarify the situation, it would be highly desirable to understand how during the evaporation chain staggering effects are generated, and in particular if they are already present at finite temperature, i.e. is at the last-but-one evaporation step. In order to gather model independent experimental information on the relative isotopic population at finite excitation energy, we will extract in the next section the excited states population through correlation functions.

6.2 Particle Correlations

Intensity interferometry via particle correlations was first studied in astrophysics [52]. This idea has later been generalized to correlations in nuclear physics involving various types of particles. The early example such as proton-proton [53] correlations involve identical fermions. These have been widely used for studying the properties of the sources of particles emitted in heavy ion reactions. Subsequently, non-identical particle correlations such as d-alpha correlations and correlations involving heavier fragments (up to Carbon) have also been studied; these studies have provided insight regarding the freeze-out conditions for multifragmentation processes where the nuclear interaction vanishes [54, 55] and have contributed to determine the populations of excited states of emitted fragments [56].
In this section we propose a back-tracing technique based on correlation functions of the relative kinetic energy of isotope pairs, to address the problem of quantitatively understanding odd-even effects and hopefully gather information on pairing and symmetry properties of the nuclear level density.

If we concentrate on light nuclei (IMF), their discrete spectrum is typically so much extended that the last evaportion step takes place typically from a discrete resonance, which can at least in principle be recognized as a peak in a relative kinetic energy two-body correlation function. Because of the limited statistics, we analyze peripheral events as a whole, which corresponds to a distribution of sources in A and E*. To really reconstruct the last-but-one evaporation step one should have measured also n-IMF correlations functions, out this is not possible with present apparatus in this energy range. Because of these problems, we cannot extract quantitative information on the temperature dependence of the pairing. However one can experimentally assess how much the yield of fragments which are dominated by a last p or α evaporation step is influenced by this last decay. This will give us important information on how much important is this last step in the production of the odd-even effect.
The correlation functions are interpreted within the Koonin-Pratt formalism [53] and within the assumption of thermal equilibrium.

6.2.1 Koonin-Pratt Formalism and Equilibrium Correlation Approximation

Experimentally the two particle correlation function may be defined as follows,

$$\sum Y_{12}(\vec{p_1}, \vec{p_2}) = C(1 + R(q)) \sum [Y_1(\vec{p_1}) Y_2(\vec{p_2})] \tag{6.2}$$

where Y_{12} is the two particle coincidence yield of a given pair of particles with their individual momenta $\vec{p_1}$ and $\vec{p_2}$, respectively, and the $Y_i(\vec{p_i})$ are the single particle yields for the two particles not measured in the same event. The summations on both sides of the equation run over pairs of momenta $\vec{p_1}$ and $\vec{p_2}$ corresponding to the same bin in relative momentum q.
The correlation function describes how the correlation between coincidence particles measured in the same event differs from the underlying correlation dictated largely by phase space and modelled by mixing the single particle distributions of particles from two different events (the so-called event-mixed yield). The correlation constant C is

typically chosen to ensure that $R(q) = 0$ at large relative energies where the correlations due to final state interactions and quantum statistics can be neglected.

If the summation in Eq. 6.2 does not involve strong constraints on the emission angles of particles 1 and 2, the appropriate comparison is to the angle-averaged Koonin-Pratt equation [53]

$$C(q) \equiv 1 + R(q) = 1 + 4\pi \int dr r^2 K(q, r) S(r) \tag{6.3}$$

where the source function S(r) is defined as the probability distribution for emitting a pair of particles with relative distance r at the time when the second particle is emitted. The angle-averaged kernel, K(q, r), is obtained from the radial part of the antisymmetrized two-proton relative wave function as follows [57],

$$K(q, r) = |\Phi_q(r)|^2 - 1 \tag{6.4}$$

where the wave function $\Phi_q(r)$ describes the propagation of the pair from a separation r out to the detector at infinity, where relative momentum q is reached. Correlation functions have been analyzed using Eq. 6.3 for a variety of correlations involving hydrogen and helium isotopes [58]. One of the factors limiting the extension of the Koonin-Pratt equation to heavier particles is the care needed to construct the Kernel K(q,r). Essentially, one must search for a set of attractive nuclear potentials that can reproduce the experimental phase shifts. Right now, we have only the necessary potentials for the p-p and d-α correlation functions. To rapidly extend the correlation function to heavier particles and to facilitate the comparison to statistical models, we use here a formalism for calculating the correlation function within equilibrium theory [60].

The starting point for this development is the consideration of elements needed for the equilibrium description. First, one needs to have a compact method for incorporating both the long range Coulomb and short range nuclear interactions. Second, one must address the volume that is occupied by other particles. We choose to address the second issue by invoking the excluded volume approximation. This essentially amounts to counting as particles only those that are isolated, a procedure that is consistent with most of the equilibrium multifragmentation approaches [59]. Equilibrium correlation

function expressions are derived by considering how the two particle phase space is modified by interactions. For simplicity, we consider the simplified geometry where the center of mass of the pair of spinless particles with charges Z_1 and Z_2 is at the center of a volume V . To calculate how the phase space of relative motion is modified by the Coulomb interaction, we follow semi-classical theory which states that the phase space density is given as a function of the relative spatial separation $\overrightarrow{r}$ and relative momentum $\overrightarrow{q}$ by

$$\frac{dn}{d^3\overrightarrow{r}\,d^3\overrightarrow{q}_L} = \frac{1}{h^3} \tag{6.5}$$

where $\overrightarrow{q}_L$ is the local momentum given in terms of q, the reduced mass $\mu = M_1M_2/(M_1+M_2)$ and the Coulomb potential by:

$$q_L = \sqrt{q^2 - \frac{2\mu Z_1 Z_2 e^2}{r}} \tag{6.6}$$

Re-expressing Eq. 6.5 in terms of the momentum $\overrightarrow{q}$ at large distances where the Coulomb interaction can be neglected, we have

$$\frac{dn}{d^3\overrightarrow{r}\,d^3\overrightarrow{q}_L}|_{Coulomb} = \frac{dn}{d^3\overrightarrow{r}\,d^3\overrightarrow{q}_L}\frac{d^3\overrightarrow{q}_L}{d^3\overrightarrow{q}} = \frac{1}{h^3}\sqrt{1 - \frac{2\mu Z_1 Z_2 e^2}{rq^2}} \tag{6.7}$$

If the above equation is integrated over a volume V and divided by the corresponding integral of the relative phase space density of two free particles, $dn/d^3\overrightarrow{q} = V/h^3$, an expression for the Coulomb correlation function $1 + R_{Coul}$ may be obtained as follows,

$$1 + R_{Coul}(q) = \frac{1}{V}\int_V d^3r\sqrt{1 - \frac{2\mu Z_1 Z_2 e^2}{rq^2}} \tag{6.8}$$

One begins by imagining that two interacting particles are placed in a spherical container centered about their common center of mass. The appropriate boundary condition assumes the wavefunction of relative motion vanishing at the container walls. In the asymptotic region, the radial wavefunction is of the form

$$\Psi \propto \frac{sin[qr/\hbar - \eta ln(2qr/\hbar) - l\pi/2 + \delta_l(q)]}{qr}Y_{\lambda\mu} \tag{6.9}$$

The boundary condition therefore requires $qr/\hbar - \eta ln(2qr/\hbar) - l\pi/2 + \delta_l(q) = m\pi$, where $\eta = Z_1 Z_2 e^2/\hbar v$ is the Coulomb parameter. Separating the phase shift into Coulomb σ_l and strong interaction $\delta_l^{'}$ components, the density of states is

$$\frac{dn}{dq} = (2l+1)\frac{dm}{dq} = \frac{1}{\pi}\sum(2l+1)\left\{\frac{R}{\hbar} + \frac{d}{dq}[\eta ln(2qR/\hbar) + \sigma_l(q)]\right\} + \frac{1}{\pi}\sum(2l+1)\left\{\frac{d\delta_l^{'}}{dq}\right\} \quad (6.10)$$

In Eq. 6.10, the first term represents the density of states for the pure Coulomb problem and the second term is the density of states due to the strong interaction. Since the first term is difficult and unwieldy to use, one can use the semiclassical expression in Eq. 6.8 or some similar shape for the Coulomb density of states. We will use the second term for the strong interaction effects. Taking the spin of the particles and resonances into account, the two particle phase space of relative motion becomes

$$\frac{dn_{12}}{d^3\overrightarrow{q}} = \frac{(2S_1+1)(2S_2+1)}{h^3}\frac{V_f}{V}\int_V d^3\overrightarrow{r}\sqrt{1 - \frac{2\mu Z_1 Z_2 e^2}{rq^2}} + \frac{1}{4\pi^2 q^2}\sum_{J,l}(2l+1)\frac{d\delta_{Jl}^{'}}{dq} \quad (6.11)$$

where V_f and V are the free (unoccupied) and total (including occupied) volumes of the system, respectively. Given this relationship, the correlation function as a function of relative momentum becomes

$$1 + R(q) = 1 + R_{Coul}(q) + R_{nucl}(q) = \frac{1}{V}\int_V d^3\overrightarrow{r}\sqrt{1 - \frac{2\mu Z_1 Z_2 e^2}{rq^2}} + \frac{h^3}{4\pi^2 q^2 V_f (2S_1+1)(2S_2+1)}\sum_{J,l}(2l+1)\frac{d\delta_{Jl}^{'}}{dq} \quad (6.12)$$

and as a function of relative energy E_{rel} becomes

$$1 + R(E_{rel}) = 1 + R_{Coul}(E_{rel}) + R_{nucl}(E_{rel}) = \frac{1}{V}\int_V d^3\overrightarrow{r}\sqrt{1 - \frac{Z_1 Z_2 e^2}{rE_{rel}}} + \frac{h^3}{4\pi^2 V_f (2S_1+1)(2S_2+1)\mu\sqrt{2\mu E_{rel}}}\sum_{J,l}(2l+1)\frac{d\delta_{Jl}^{'}}{dE_{rel}} \quad (6.13)$$

To extend correlation function analyses to heavier particles we can at the present time only apply the equilibrium correlation approximation. This approximation is equivalent in many respects to the Koonin-Pratt formalism. The integral of the first term

in Eq. (6.12) over the distribution of relative separations for the two decay products within the source displays a minimum at small relative energy, whose width depends on the source size. The detailed distribution over the source volume may depend on particle type. If these distributions are not at the focus of interest, it is more straightforward to parameterize this background contribution by an empirical expression

$$1 + R_{Coul} = 1 - exp[-(E_{rel}/E_C)^{\alpha}] \tag{6.14}$$

which vanishes at zero relative energy and reaches unity at large relative energy. We will use this expression in the following analysis. When the derivative of the nuclear phase shift is given in a Breit-Wigner form

$$\frac{d\delta'_{Jl}}{dq} \approx \frac{\Gamma_i/2}{(E_{rel} - E_i^*)^2 + \Gamma_i^2/4}(B.R.) \tag{6.15}$$

the nuclear correlation function in Eq. 6.12 becomes

$$R_{nucl}(E_{rel}) = \frac{h^3}{4\pi V_f (2S_1+1)(2S_2+1)\mu\sqrt{2\mu E_{rel}}} e^{-E_{rel}/T_{eff}} \times \frac{1}{\pi}\sum_i (2J_i+1)\frac{\Gamma_i/2}{(E_{rel} - E_i^*)^2 + \Gamma_i^2/4}(B.R.) \tag{6.16}$$

where S_1 and S_2 are the spins of the considered particles, μ is their reduced mass, V_f is the freeze-out volume of the system, T_{eff} is the effective temperature, J_i, E_i^*, Γ_i are the spin, excitation energy, width of the level *i*, B.R. is the branching ratio for decay to the measured channel. Examples of typical correlation functions and resulting fits via Eq. 6.16 are shown in Figs. 6.7 and 6.8. In d-alpha correlation function, we can see clearly, in the relative energy spectra, the peaks related to the resonance states of ^6Li: the 3^+ state at 2.186 MeV ($E_{rel} + Q_{value}$) and the 2+ state at 4.31 MeV. Also shown by the solid line in the figure is Coulomb correlation function calculated by Eq. 6.14. In the case of the alpha-alpha correlation as shown in Figure 6.8, the ground state 0^+ of ^8Be and its first excited state 2^+ at 3.04 MeV are illustrated. In this example the identical particle effect is observed. That is, the phase space of the two identical particles is reduced by a factor 2 and consequently the resonance correlation R_{nuc} becomes twice as large as in Eq. 6.16.

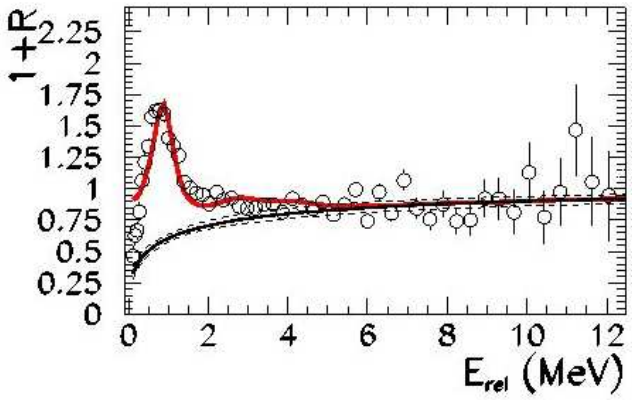

Figure 6.7: Relative kinetic energy correlation function (symbols) of $\alpha - d$ pairs, measured in peripheral $^{32}S + ^{58}Ni$ collisions and fit through Eq.6.16 (line).

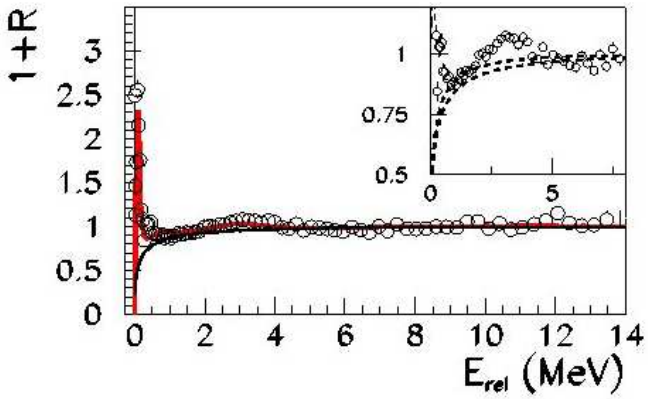

Figure 6.8: Relative kinetic energy correlation function (symbols) of $\alpha-$pairs, measured in peripheral $^{32}S + ^{58}Ni$ collisions and fit through Eq.6.16 (line).

6.3 Efficiency of the apparatus for the measured correlation functions

Since we would like to recover information on the yields of pre-fragments, we have calculated the efficiency of the employed apparatus for the measured correlation functions, following the procedure of Ref.s [56, 61]. The efficiency function of the apparatus for the decay of "'warm"' fragments in the observed channels was determined by Monte Carlo calculations, taking into account the geometry of the detectors, the energy resolution, energy thresholds and the granularity of the telescopes. The energy spectra and the angular distribution of excited parents have the same shape as those observed for stable fragments. For parent nuclei with particle unstable ground state energy distribution of neighboring stable nuclei were used to calculate the boost in the laboratory frame for the produced pair of daughters.

The decay of parent nucleus is isotropic in its rest frame. Only the angular range covered by the forward detector ($\theta = 5.3^o - 17.5^o$), where detected particles and fragments are isotopically resolved, was considered for efficiency calculations. The integral efficiency for each decay channel was defined [56] as the ratio between the yield of detected pairs and the number of generated pairs for each bin of relative energy.

For a generated flat distribution of excitation energy of the parent nucleus (flat distribution of relative energy of the daughter particles) the integral efficiency shows an increasing trend in the first MeV of relative energy, starting from 0 at 0 relative energy, 80% below 0.5 MeV. From about 1 MeV of relative energy it remains constant at about 90%, similarly to the case of other experimental devices with spherical arrangement of the detectors [62] around the beam axis. The reduced efficiency at small relative energies is due to the finite granularity and the rejection of double hits in the same telescope. At high relative energies the efficiency results smaller when pairs of light particles or fragments are considered, as for instance $p, d, ^{3,4}He$ and $^{6,7}Li$, while the kinematics favors an higher efficiency in the case one of the two partners is heavier, as for instance a Be, B or C.

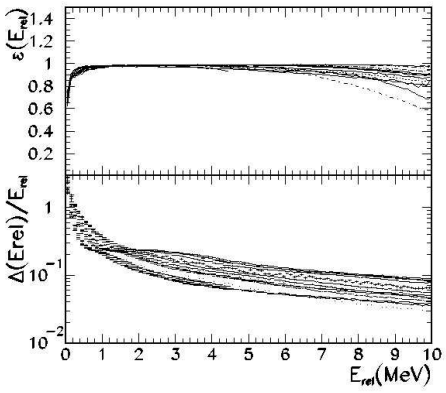

Figure 6.9: Integral efficiency (top panel) and percentual deviation (bottom panel) between the generated and detected relative energy as a function of the relative energy of detected particles for all the measured correlation functions.

To give some specific examples, the integral efficiency factors are found to be 79% and 95% for the $^8Be_{g.s.}$ and the 3.04 MeV excited state, respectively. In the case of the first excited state of ^6Li (2.186 MeV excitation energy) the integral efficiency resulted 88%.

The distortions of the widths of excited states, due to the finite opening angles of the individual telescopes, to the limited granularity of the experimental device and to low energy cuts in the relative kinetic energy distribution was evaluated by comparing the generated and filtered relative energy spectra. We show in the bottom panel of Fig. 6.9 the percent deviation between the relative energies before and after the filtering procedure.

We have also considered specific cases and we have evaluated the modifications of the rms of the relative energy distribution. For the 3.04 MeV excited state of ^8Be it resulted a detected rms of 0.97 MeV to be compared with the rms of the generated distribution of 0.75 MeV. Much larger is the deformation of the $^8Be_{g.s.}$ emission, with a detected

rms of 0.29 MeV instead of the generated $3 \cdot 10^{-4}$ MeV. In the case of the first excited state of ^{6}Li the rms after the filter is 0.19 MeV instead of the unfiltered 0.01 MeV, again similarly to other experimental devices [62].
Following this Monte-Carlo simulation, the tabulated level widths in Eq.(6.16) were increased to account for the estimated efficiencies. The Coulomb background parameters E_C and α of Eq. 6.14 are free parameters of the fit. The same is true for the nuclear parameters V_f and T_{eff} of Eq. 6.16, which would represent a physical volume and a physical temperature only in the idealized situation of a single decay step of a perfectly equilibrated source in the absence of any collective flow nor experimental deformation.

6.4 Primary fragments

Examples of typical correlation functions and resulting fits via Eq. 6.16 are shown in the top panels of Figs. 6.11, 6.10. We also show in Fig. 6.12 the correlation function for the $\alpha - \alpha$ pairs, emitted by the unstable ^{8}Be. Primary yields are calculated by multiplying the nuclear contribution R_{nuc} (Eq. 6.16) of the correlation function for the uncorrelated yield $\Sigma Y_1(\vec{p_1})Y_2(\vec{p_2})$ of Eq. 6.2. The experimentally reconstructed primary population is shown with open symbols for some selected nuclei in the bottom panels of Fig.s 6.11 and 6.12, together with the contributions from the different parent excited levels entering in Eq. 6.16, shown as lines. The total primary population of a given isotope at the last-but-one evaporation step $Y(A,Z)$ is calculated by integrating over the relative energy the primary yields given by the bottom part of Figs. 6.11 and 6.12.

The primary yields obtained through this procedure for the unstable ^{8}Be have been already reported in Fig. 6.4. Interesting enough, some excited levels which energetically lie above the lowest threshold for particle emission in the daughter nucleus contribute to the data. To give an example, most of the correlated yield associated to the $\alpha + ^{6}Li$ correlation function presented in Fig. 6.10 is associated to excited levels of ^{10}B around $E^* = 6.6$, lying about 300 keV above the threshold for the ^{6}Li decay in $^{4}He + d$

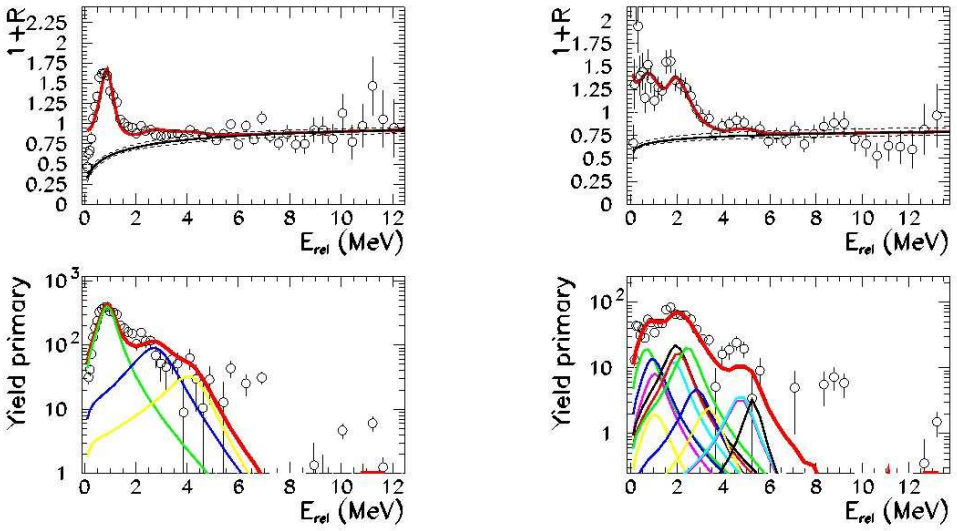

Figure 6.10: Upper part: representative relative kinetic energy correlation functions (symbols) of different isotopes measured in peripheral ^{32}S +^{58} Ni collisions and fit through Eq.6.16 (line). The obtained background is also indicated together with its uncertainty. Lower part: experimental population of primary parents (open symbols) and their excited states (thin lines) together with their sum (thick line). From left to right: $d-\alpha$ correlations and corresponding excited states of ^{6}Li, α –^{6} Li correlations and corresponding excited states of ^{10}B.

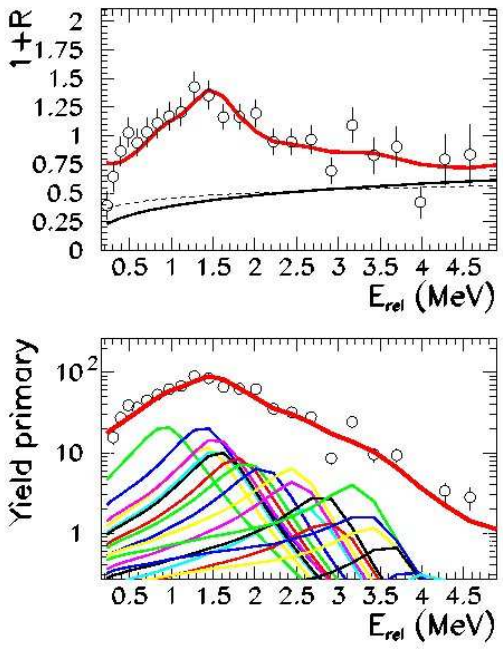

Figure 6.11: Upper part: representative relative kinetic energy correlation functions (symbols) of $p - {}^{13}C$ pair measured in peripheral ${}^{32}S + {}^{58}Ni$ collisions and fit through Eq.6.16 (line). The obtained background is also indicated together with its uncertainty. Lower part: experimental population of primary parents (open symbols) and their excited states (thin lines) together with their sum (thick line).

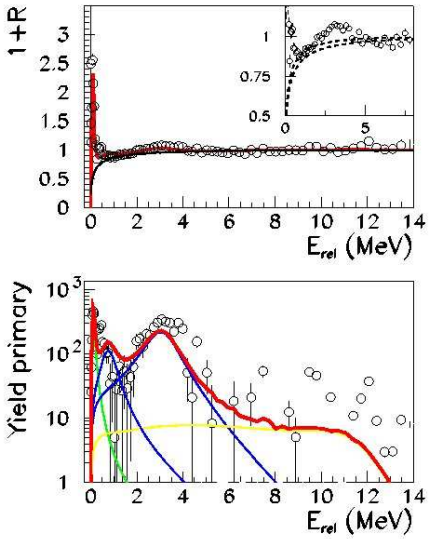

Figure 6.12: Upper part: relative kinetic energy correlation function (symbols) of $\alpha-$pairs, measured in peripheral $^{32}S + ^{58}Ni$ collisions and fit through Eq.6.16 (line). The obtained background is also indicated together with its uncertainty. A more detailed view of the correlation function around 3 MeV is shown in the insert. Lower part: experimental population of the ^{8}Be parent (open symbols) and its excited states (thin lines) together with their sum (thick line).

and below the separation energy for the neutron emission for this daughter nucleus, which potentially can decay via $d-\alpha$ emission. Since the ^4He+d correlation function (shown in Fig. 6.10) was measured, it should be interesting for this case to perform a 3-body decay correlation $\alpha+\alpha+d$ to calculate the amount of primary fragments before their last step of the decay.

However, due to the limited statistics associated to the peripheral sample, we can not perform 3-body correlations nor show other cases of successive decays.

To show however that the $\alpha+^6 Li$ is is not a single case of possible successive decays, we analyzed the whole sample, obtained for the detected events without any selection on the collision mechanism. In Fig. 6.13 we show the correlation function $p+^{13} C$, already shown in Fig. 6.11 for peripheral events, just to show that an higher statistics allows to explore an higher range of excitation energy of the parent nuclei.

We show also the $p+^7 Li$ correlation function, corresponding to the decay of $^8Be^*$. The excitation energy of the parent $^8Be^*$ overcomes of about 2 MeV, with non negligible yield, the threshold for $\alpha + T$-emission of $^7Li^*$, which is below the separation energy for neutron emission. Also the correlation function for $T + \alpha$ is measurable, and it is shown in Fig.s 6.13,6.14.

These examples show that the emission is not necessarily associated to the lowest threshold, but it depends in a more complicated way on the history of the evaporation chain.

Coming back to peripheral collisions, the different primary nuclei reconstructed via Eq. 6.16, their probability and average excitation energy are shown in Fig. 6.15. The probability of "'warm"' fragments of charge Z has been defined as:

$$P(Z_{c.n.}) = \frac{\sum_A Y(A,Z)}{\sum_A Y_{12}(A,Z)} \tag{6.17}$$

where $Y(A,Z)$ represents the yield of a primary fragment (A,Z) as extracted from correlation functions and Eq. 6.16. The denominator of Eq. 6.17 is given by the sum of the correlated yields of Eq. 6.2 over all the isotope pairs with sum of charges equal to Z.

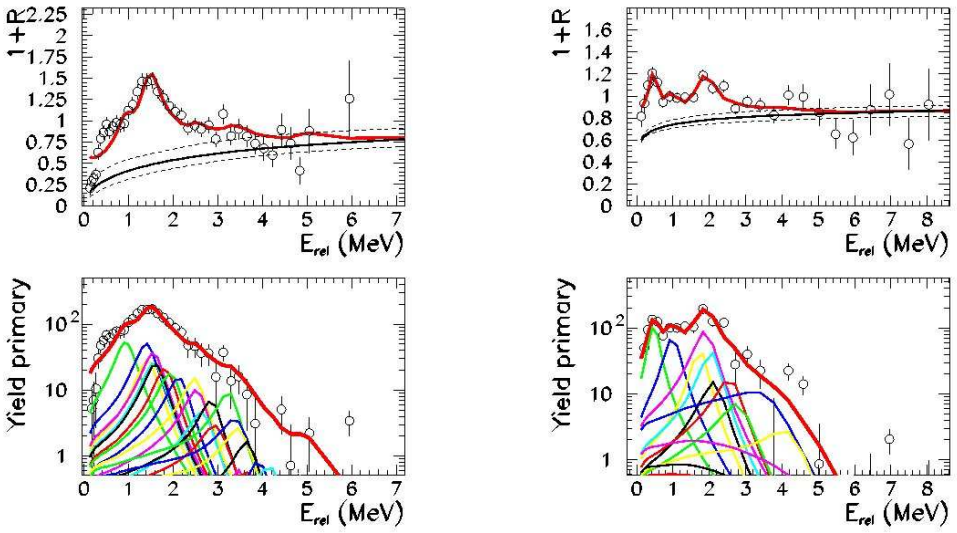

Figure 6.13: Upper part: relative kinetic energy correlation functions (symbols) of different isotopes measured in the whole sample of $^{32}S + ^{58}Ni$ collisions and fit through Eq. 6.16 (line). The obtained background is also indicated together with its uncertainty. Lower part: extracted population of the different parent excited states (thin lines) together with their sum (thick line). From left to right: $p - ^{13}C$ correlations and corresponding excited states of ^{14}N, $p - ^{7}Li$ correlations and corresponding excited states of ^{8}Be.

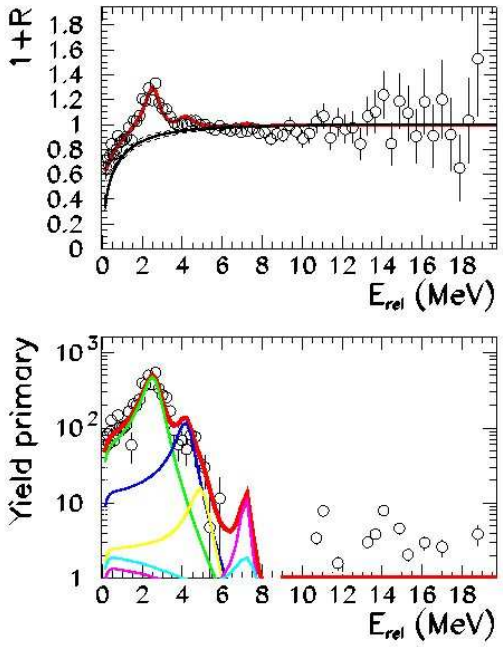

Figure 6.14: Upper part: relative kinetic energy correlation functions (symbols) of $T-\alpha$ pairs measured in the whole sample of $^{32}S+^{58}Ni$ collisions and fit through Eq. 6.16 (line). The obtained background is also indicated together with its uncertainty. Lower part: extracted population of the parent (^{7}Be) excited states (thin lines) together with their sum (thick line).

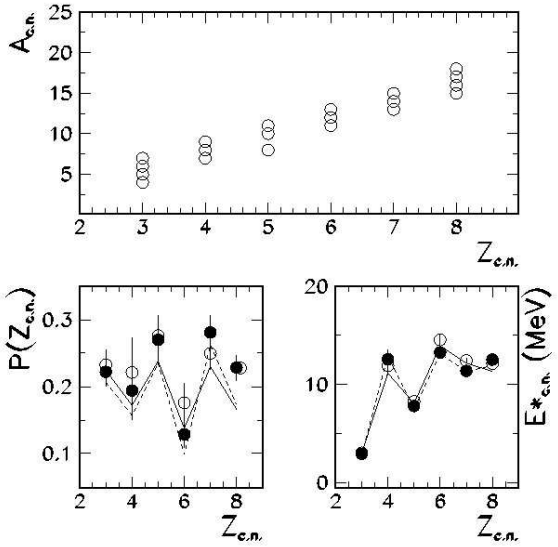

Figure 6.15: Upper part: isotopes reconstructed (in at least one of their lowest lying particle unstable excited states) by the correlation function technique in the two data sets. Lower part: extracted population of the different primary fragments (left) and their average excitation energy (right) for the peripheral $^{32}S + ^{58}Ni$ (full symbols) and $^{32}S + ^{64}Ni$ (circles) data set.

The reconstructed "warm" yields keep on showing the staggering, meaning that the evaporation chain plays a role, at least for the light fragments examined. Particularly striking is the fact that this staggering shows an opposite trend with respect to the experimental asymptotic distributions shown in Figs. 6.1, 6.2 and 6.3.

Dashed ($^{32}S + ^{58}Ni$) and continuous ($^{32}S + ^{64}Ni$) lines of Fig. 6.15 represent the yields given from tabulated levels, shown in the bottom panels of Fig. 6.11. The distance between symbols and lines, for each reaction, can be interpreted as a measure of the background present in the data. In Fig. 6.11 indeed some measured yields at the highest values of the relative energy do not correspond to tabulated levels and therefore they can not be fitted by Eq. 6.16.

In Fig. 6.16 we show the reconstructed "warm" yields before (top panel) and after (bottom panel) the integral efficiency correction for the measured correlation functions. Since the integral efficiency resulted quite high, as shown in Fig. 6.9, these corrections do not change the oscillating behavior observed in the left-bottom panel of Fig. 6.15.

A limitation of our analysis is the systematic absence of neutron-decaying states in our reconstruction of excited levels, due to the lack of neutron detection. One may then wonder if this systematic lack may be at the origin of the inverse staggering displayed in Fig. 6.15. To answer this question, from the same tables used to fit the measured correlation functions (Ref.s [63, 64]), we define the elemental yield for discrete levels decaying only by neutron emission (open symbols and dashed line of Fig. 6.17) and for levels decaying either by charged particle or neutron emission (stars, dotted line).

$$f(Z) = \sum_{N=Z-1}^{Z+2} \sum_{i} (2J_i + 1) \exp(-E_i^*/T_{eff}) \tag{6.18}$$

The first sum of eq. 6.18 covers the isotopic range corresponding to a non negligible measured yield for the given Z in the IMF range $3 \leq Z \leq 8$; the second sum runs over the known discrete levels of the given isotope of energy E_i^* and spin J_i which decay only by neutron emission or also by charged particle emission. T_{eff} is a temperature parameter which we have taken as $T_{eff} = 2.5$ MeV, coherent with the measured excitation energy of the peripheral sample, assuming a level density parameter about

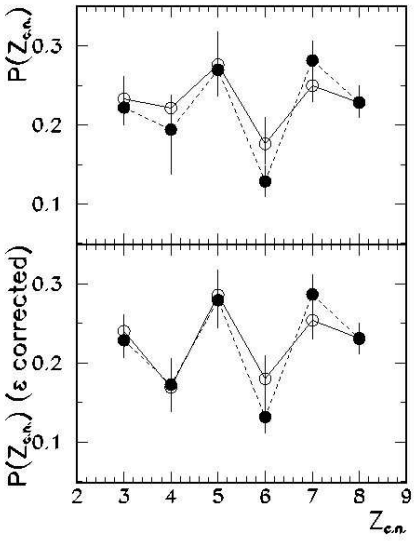

Figure 6.16: Upper part: population of the different primary fragments (already shown in the left-bottom panel of Fig. 6.15). Lower part: population of the different primary fragments corrected for the integral efficiency of each correlation function. Data for peripheral data for $^{32}S + ^{58}Ni$ reaction are drawn as full symbols, connected by dashed lines. Data for peripheral $^{32}S + ^{64}Ni$ reaction are drawn as circles, connected by full lines.

$a = A/6$ and in agreement with the average temperature measured from excited states thermometers for this same sample. In both calculations shown in Fig. 6.17, for all

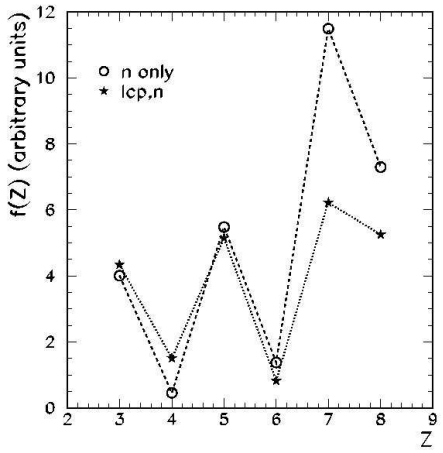

Figure 6.17: (Color online) Elemental yields (eq. 6.18) from discrete levels decaying only by neutron emission (open symbols, dashed line) or by charged particle and neutron emission (stars,dotted line).

values of the charge of the warm parent nucleus, the same staggering observed for reconstructed primary fragments (Fig. 6.15) is present, again opposite to the trend of measured cold isotopes of Fig. 6.5.

In addition a smaller contribution of neutron decaying levels for even parents with respect to the odd ones is apparent in Fig. 6.17, indicating that the trend of the experimental distribution at the last-but-one evaporation step of Fig. 6.15 is not qualitatively deformed by the lack of neutron detection.

We conclude that the origin of the staggering has to be searched for in the evaporation chain, and cannot be attributed to the pairing effect of nuclear masses alone.

Chapter 7

Data comparison with GEMINI model

Further insights on odd-even effects might be gained from statistical model calculations. Because of the limited excitation energy, our peripheral sample can be reasonably described as a standard Hauser-Feshbach or Weisskopf evaporation from an excited source of mass and charge close to the projectile (in this case we can use GEMINI model for simulate our data). GEMINI [65] is a Monte Carlo code which follows the decay of a compound nucleus by a series of sequential binary decays, therefore the model cannot well reproduce a simultaneous fragmentation of compound nucleus.

7.1 GEMINI

The first version of the statistical-model code GEMINI was written in 1986 to address complex-fragment emission in fusion reactions. It differed from most other statistical-modes codes at the time since it allowed not only light-particle evaporation and symmetric fission, but all possible binary-decay modes. GEMINI is a Monte Carlo code which follows the decay of a compound nucleus by a series of sequential binary decays until such decays are impossible due to energy conservation. As GEMINI was written to compare data from heavy-ion induced fusion reactions, the effects of large angular momenta were explicitly treated. For this reason the dichotomy between light-particle evaporation and other binary decays was still maintained. The best

way of treating light-particle evaporation at high angular momentum is via the Hauser-Feshbach formalism [66] . For heavy systems, GEMINI simulations generally over-predict the width of the fission mass and charge distributions. Although this may be a failure of the asymmetric fission barriers used in the calculations, it probably means a failure of the underlying model. Indeed the used formalism [67] predicts the mass-asymmetry distributions along the ridge of conditional saddle points. However, the final mass of the fission fragments is not frozen until the scission point is reached. For light nuclei, the saddle and scission points are almost degenerate so substantial modification during the saddle-to-scission motion is expected to be small. On the other hand for heavy systems, the saddle and scission configurations are quite different. Specifically for very heavy systems, the saddle point can no longer be approximated by two nascent fragments connected by a neck. The neck disappears and the saddle point is a deformed mononucleus making impossible to even define an asymmetry degree of freedom. In such cases, the mass asymmetry develops during the transition from saddle to scission. Therefore, the failure of GEMINI for these heavier systems was not unexpected. Due to these deficiencies of the original code for heavy nuclei, a new version of the code GEMINI has been written to address these problems. In this new version, extensive comparisons with heavy-ion induced fusion data have been used to optimize the default parameters of the model. Such data are useful for constraining statistical-model codes and the excitation energy and spin distributions of the compound nuclei can be well defined.

7.1.1 Evaporation formalism

In the Hauser-Feshbach formalism [66], the partial decay width of a compound nucleus of excitation energy E^* and spin J_{CN} for the evaporation of particle i is

$$\Gamma_i(E^*, J_{CN}) = \frac{1}{2\pi\rho_{CN}(E^*, J_{CN})} \int d\varepsilon \sum_{J_d=0}^{\infty} \sum_{J=|J_{CN}-J_d|}^{J_{CN}+J_d} \times \sum_{l=|J-s_i|}^{J+s_i} T_l(\varepsilon)\rho_d(E^* - B_i - \varepsilon, J_d) \quad (7.1)$$

where J_d is the spin of the daughter nucleus, S_i, J, and l, are the spin, total and orbital angular momenta of the evaporated particle, ε and B_i are is its kinetic and sep-

aration energies; T_l is its transmission coefficient or barrier penetration factor; ρ_d and ρ_{CN} are the level densities of the daughter and the compound nucleus, respectively. The summations include all angular momenta couplings between the initial and final states. Evaporation channels include $n, p, d, t,^3He, \alpha,^6He,^{6-8}Li$, and ^{7-10}Be fragments.

The nuclear level density is often approximated by the Fermi-gas form [34] derived for a spherical nucleus in the independent-particle model with constant single-particle level densities,

$$\rho_{FG}(E^*, J_{CN}) = \frac{(2J+1)}{24\sqrt{2}a^{\frac{1}{4}}U^{\frac{5}{4}}\sigma^3} exp(S), S = 2\sqrt{aU}, \tag{7.2}$$

where S is the nuclear entropy and the level-density parameter is

$$a = \frac{\pi^2}{6}\left[g^n(\varepsilon_F^n) + g^p(\varepsilon_F^p)\right]. \tag{7.3}$$

Here $g^n(\varepsilon_F^n)$ and $g^p(\varepsilon_F^p)$ are the neutron and proton single-particle level densities at their respective Fermi energies and

$$U = E^* - E_{rot}(J), E_{rot} + \frac{J(J+1)\hbar^2}{2I_{rig}}, \sigma^2 = I_{rig}T. \tag{7.4}$$

The quantity I_{rig} is the moment of inertia of a rigid body with the same density distribution as the nucleus and T is the nuclear temperature:

$$\frac{1}{T} = \frac{dS}{dU}. \tag{7.5}$$

The quantity U can be interpreted as a thermal excitation, after the rotational energy of the nucleus is removed. At large angular momenta, macroscopic models of the nucleus such as the rotating liquid-drop model (RLDM) [68] and Sierk's Yukawa-plus-exponential finite-range calculations [69] predict that the nuclear shape distorts to accommodate the centrifugal forces.

Many implementations of the statistical model, including GEMINI, generalize Eq. 7.4 by the replacing $E_{rot}(J)$, the rotational energy of a spherical nucleus of fixed moment of inertia, with $E_{yrast}(J)$, the deformation plus-rotational energy predicted by these

macroscopic models where the deformation increased with spin. In GEMINI, the Sierk predictions of $E_{yrast}(J)$ are used for all but the lightest compound nuclei.

7.1.2 fission and complex fragment decay

Fission was first incorporated into the statistical model by Bohr and Wheeler using the transition-state formalism first introduced to calculate chemical reaction rates.

The Bohr-Wheeler transition-state decay width for symmetric fission [70] is:

$$\Gamma_{BW} = \frac{1}{2\pi\rho_{CN}(E^*, S_{CN})} \int d\varepsilon \left[E^* - B_f(S_{CN} - \varepsilon)\right] \tag{7.6}$$

where ρ_{sad} is the level-density at the saddle-point, $Bf(S_{CN})$ is the spin-dependent saddle-point energy (fission barrier + ground-state rotational energy) and ε is the kinetic energy in the fission degree of freedom. The 2-dimension extension of this by ref. [67] is:

$$\Gamma_y dy = \frac{1}{2\pi\rho_{CN}(E^*, S_{CN})} \int\int \frac{dy dp_y}{h} d\varepsilon \rho_{sad} \left[E^* - B(y, S_{CN}) - \frac{p_y^2}{2m_y}\varepsilon\right] \tag{7.7}$$

where y is the mass asymmetry ($y = A_1 - A_2/A_1 + A_2$), p_y is its conjugate momentum, m_y is the inertia associated with motion in the y coordinate, and $B(y, S_{CN})$ are the energies of the condition saddle-points. The barriers are conditional in the sense they represent a saddle-point configuration when the specified mass asymmetry is imposed. In the potential-energy surface, these conditional saddle points represent a ridge which must be crossed in order to get to the scission configuration. Simplification to this formula can be made from the expansion

$$\rho(E^* - x) \cong \rho(E^*) exp(-\frac{x}{T}) \tag{7.8}$$

where the nuclear temperature is determined as

$$\frac{1}{T} = \frac{dln\rho(E^*)}{dE^*} \tag{7.9}$$

With this expansion, the above equation can be reduced to:

$$\Gamma_y dy = \frac{1}{2\pi\rho_{CN}(E^*, S_{CN})} \frac{\sqrt{2\pi T m_y}}{h} \int d\varepsilon \rho_{sad} \left[E^* - B(y, S_{CN}) - \varepsilon\right] \tag{7.10}$$

With this formalism, in addition to the conditional barriers, one also requires knowledge of the inertia m_y. Later in Ref. [67] has been suggested

$$\Gamma_Z = \frac{1}{2\pi\rho_{CN}(E^*, S_{CN})} \int d\varepsilon \rho_{sad} \left[E^* - B_Z(S_{CN}) - \varepsilon\right] \tag{7.11}$$

where Z is the proton number of one of the nascent fragments. Basically the term $\frac{\sqrt{2\pi T m_y}}{h}$ has been eliminated and the problem has been discretized. In GEMINI this was further extended by allowing for distinct mass and charge splits:

$$\Gamma_{Z,A} = \frac{1}{2\pi\rho_{CN}(E^*, S_{CN})} \int d\varepsilon \rho_{sad} \left[E^* - B_{Z,A}(S_{CN}) - \varepsilon\right] \tag{7.12}$$

The conditional barriers now have both the mass and charge asymmetries imposed and are estimated as

$$B_{Z,A}(S_{CN}) = B_A^{Sierk}(S_{CN}) + \Delta M + \Delta E_{Coul} - \delta W - \delta P \tag{7.13}$$

where δW and δP are the ground-state shell and paring corrections to the liquid drop barrier.The quantity B_A^{Sierk} is the interpolated Sierk barrier for the specified mass asymmetry. In the Sierk's Finite-Range calculations, the two nascent fragments have the same Z/A ratio. The correction ΔM now accounts for the different Z/A values of the two fragments, i.e.

$$\Delta M = M(Z, A) + M(Z_{CN} - Z, A_{CN} - A) - M\left(Z_{CN}\frac{A}{A_{CN}}, A\right) - M\left(Z_{CN}\frac{A_{CN} - A}{A_{CN}}\right) \tag{7.14}$$

where M(Z,A) is the spherical Finite-Range Model mass. In addition there is a Coulomb correction

$$\Delta E_{Coul} = E_{Coul}(Z, A, Z_{CN} - Z, A_{CN} - A) - E_{Coul}(Z_{CN}\frac{A}{A_{CN}}, A, Z_{CN}\frac{A_{CN} - A}{A_{CN}}, A_{CN} - A) \tag{7.15}$$

where $E_{Coul}(Z_1, A_1, Z_2, A_2)$ is the Coulomb energy between two fragments (Z_1, A_1) and (Z_2, A_2) estimated as two spheres separated by 2 fm with a radius parameter r_0 of 1.225

fm. The total width requires summations over both the Z and A values of the lightest fragment. In GEMINI, for both light systems and for asymmetric divisions of heavy systems, the formalism of Ref. [67] is kept. All binary divisions are included having asymmetries greater than the value at which the conditional barrier is a minimum, which is spin dependent. For the more symmetric divisions in heavy nuclei, the Bohr-Wheeler formalism is used to predict the total symmetric fission yield in GEMINI. The fission barrier is taken from Sierk's Finite-Range Model value after correcting for the ground-state shell and pairing correction, i.e.,

$$B_f = B_f^{Sierk}(S) - \delta W - \delta P. \tag{7.16}$$

Once the saddle-point is crossed, the system loses excitation energy due to light-particle evaporation during the slow saddle-to-scission motion. To estimate the magnitude of this effect, the time required for this motion was assumed to be $t = \eta(B_{sad} - B_{sciss})$ where Bsad and Bsciss are the symmetric saddle and scission point energies and η is the friction. The scission point energy is determined as $B_{sciss} = Ek_{tot} - Q_f$ where Ek_{tot} is the total kinetic energy released in fission and Q_f is fission Q value. In the transition from saddle to scission, excitation energy increases due to dissipation and at the same decreases due to evaporation. The total change in potential between saddle and scission $B_{sad} - B_{sciss}$ is assumed to be dissipated into excitation energy at the scission point. As Bsciss is spin independent, the Weisskopf-Ewing formalism is used for evaporation at this stage to calculate the decay widths.

7.2 Simulation and data

In our peripheral sample, the emitting source is not well defined in the experimental data because different impact parameters are summed up, neutrons are not measured and the statistics is too poor to make precise selections in the source characteristics. This means that data have to be seen as a superposition of different masses, isospins, angular momenta and excitation energies. Because of this limitation we have not tried

a quantitative comparison between model and data. The purpose of the calculation being simply to enlighten the physical mechanism leading to the presence (absence) of odd-even effects in the different thermodynamic conditions, we have simply fixed in the GEMINI [65] evaporation model a source with Gaussian distributed parameters centered on $< E^* >$=1 A MeV, $< Z >$=16, $< A >$= 32, and have considered a triangular distribution of angular momentum between $J_{min} = 0\hbar$ and $J_{max} = 16\hbar$, as given by the systematics of fusion cross-section. Increasing (decreasing) the value of J_{max} has the only affect of increasing (decreasing) the overall yield of IMF between $Z = 3$ and $Z = 9$ without affecting the behavior of the isotopic chains.

The results for the different isotopic chains as well as the inclusive distributions are reported in Fig. 7.1. We can see that the overall shape of the theoretical distribution is in relatively good agreement with the experimental data, confirming the statistical character of the collisions.

Clear staggering effects are seen in the residue region,especially in the N=Z isotopic chain, where unfortunately we do not have isotopic discrimination in the experiment.

Since in the model calculation N=Z+1 nuclei are the most abundant isotopes in the residue region and their distribution is essentially smooth, the inclusive theoretical distribution does not show any noticeable odd-even effects in this region, contrary to the experimental evidence. Concerning the IMF region, where the isotopic information is accessible experimentally, a good qualitative agreement is observed for N=Z-1 and N=Z but deviations can be seen for N=Z+1, which again is essentially flat in the calculation. In conclusion, our peripheral events appear consistent with the evaporative decay of an excited source close to the initial projectile nucleus. The staggering of the elemental distribution is qualitatively reproduced by the calculation, even if differences appear when the behavior is analyzed in different isotopic chain. A more quantitative comparison would need a better characterization of the experimental source characteristics needed as inputs of the GEMINI model, and the availability in the model of the information on the population of all the observed excited particle unstable states.

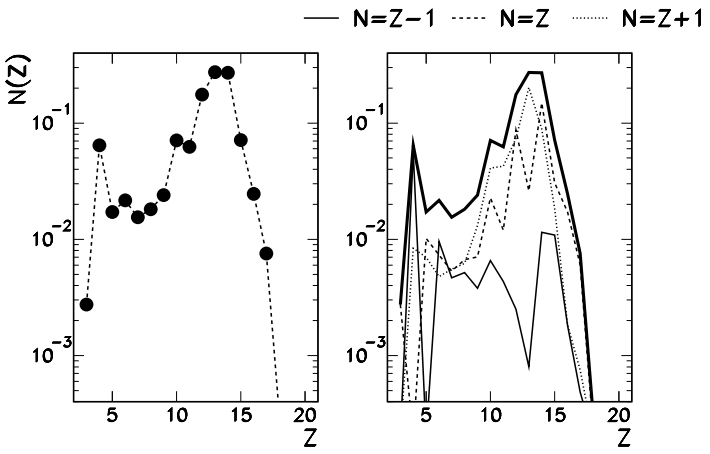

Figure 7.1: Elemental asymptotic distribution from the decay of an excited source with $< A >= 32, < Z >= 16, < E^* >= 1A\ MeV$ and a triangular distribution of angular momentum between $J = 0\hbar$ and $J = 16\hbar$, within the GEMINI evaporation model. left panel: inclusive charge distribution . right panel: distribution for different isotopic chains.

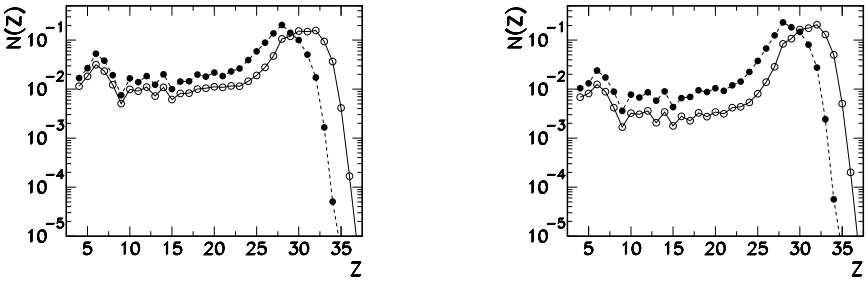

Figure 7.2: Elemental asymptotic distribution from the decay of an excited source with $< A >= 81, < Z >= 40, < E^* >= 3A\ MeV$, (full symbols,dashed lines) and $< A >= 87, < Z >= 40, < E^* >= 3A\ MeV$, (open symbols, full lines) within the GEMINI evaporation model. For both sources the angular momentum ranges from $J = 0\hbar$ to $J = J_{max}$ with a triangular distribution. Left: $J_{max} = 56\hbar$; right: $J_{max} = 40\hbar$

Now let us turn to the analysis of the central collisions. Since the experimental sample does not correspond to complete fusion of projectile and target, fluctuations arise from the mixing of event with different masses and energy transfer. For this reason, similarly to the case of binary collisions, we have not tried a quantitative comparison to experiment but considered the statistical decay of a Gaussian-distributed source, as predicted by the Hipse dynamical event generator [40], with average charge $< Z >= 40$ and two different masses 81 and 87 for the two reactions with excitation energy $< E^* >= 3$ A MeV. Since the angular momentum is not constrained by the data, we run Gemini code with the maximum value of L allowed for this source, i.e. $56\hbar$, with a triangular distribution.

Fig. 7.2 displays the inclusive charge distributions obtained from the GEMINI model for the two values of the mass of the source, to be compared with the data shown in Fig. 6.1.

As in the case of our central sample the source with the higher N/Z ratio (open symbols) leads to a heavier residue with respect to a n-poor source (full symbols). The

IMF production in the model is modified by the isospin of the source as in the data, being the two distributions different by a factor 2 in the range of charges 8-15, both in the model and in the data. Clear staggering effects can be seen in the calculation, similar to the case of the peripheral source. This confirms the expectation [43] that, in an evaporation based picture, odd-even effects do not depend on the excitation energy and are essentially determined by the last evaporation step(s). At a more quantitative level, these effects appear much more important than in the experimental sample. As we have discussed before, this may be due to the different shape of the distribution, since the theoretical predictions are more flat in the IMF region than the measured ones.

Moreover, the experimental fragment production (Fig. 6.1), for the same range of IMF charge, is about a factor 4 less than in the model distributions. We can recover the experimental IMF production, by limiting the maximum angular momentum in Gemini at 40$\hbar$, as it shown in Fig. 7.2 (right panel). The variation of the angular momentum however does not change the overall shape of the distribution, nor the importance of the odd-even effects.

As we have already discussed, the intermediate mass fragment region in the experimental sample is also populated by multifragmentation-like events where at least three fragments are emitted in each collision events. These events are characterized by large values of the "flow angle" (see Figs. 5.3), suggesting a negligible angular momentum and they represent a fraction of about 5% of well measured central events.

This specific event class is compared in Fig. 7.3 to the GEMINI calculations. The average asymmetry between the three coincident fragments is qualitatively reproduced, but the percentage of three-fragment events is about 2% in the calculation, more than a factor 2 too small with respect to the lowest experimental estimate based on data uncorrected for efficiency.

If we perform calculations with a maximum angular momentum 40$\hbar$, which re-

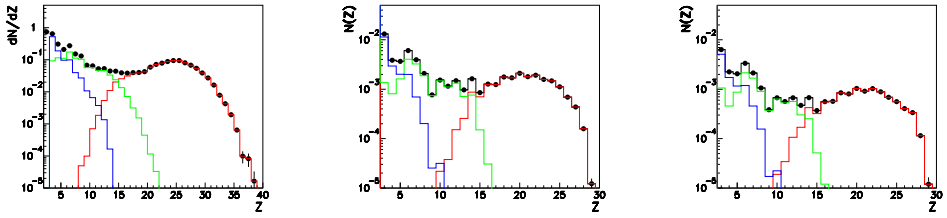

Figure 7.3: Charge distributions of events corresponding to at least three fragments ($Z \geq 3$), normalized to the total number of central events. The distribution of the largest fragment, second largest and third largest are reported as red, green, blue histograms respectively. Left: Measured central events for the reaction $^{32}S + ^{58}Ni$. Center: Gemini events for an excited source with $< A >= 81, < Z >= 40, < E^* >= 3A\ MeV$ and $J = 0 - 56\hbar$ Right: same as center, but $J_{max} = 40\hbar$.

produces the experimental IMF production in the range of charges 8-15, the fraction of three IMF events decreases down to 0.5%, an order of magnitude too small with respect to the uncorrected data.

Further insights in the decay mechanism can be obtained by looking at kinematics observables. As an example, Fig. 7.4 gives the distribution of the cosinus of the relative angle formed by the two largest fragments ($cos(\theta_{12})$, for events corresponding to at least three fragments ($Z \geq 3$).

In both cases the higher probability is at $cos(\theta_{12}) = -1$, which corresponds to two fragments back to back emitted, conserving the centre of mass momentum, accompanied by a third fragment with small mass and momentum. However, the experimental distribution slowly decreases towards $cos(\theta_{12}) = 1$, while for Gemini events the decrease is much steeper, and this difference is preserved if GEMINI events are filtered through a software replica of the apparatus. This means that in the data, different charge (and momentum) partitions are present, not accounted for by binary decays.

These discrepancies may be understood from the opening of the simultaneous multifragmentation channel, which is not accounted for in the GEMINI model.

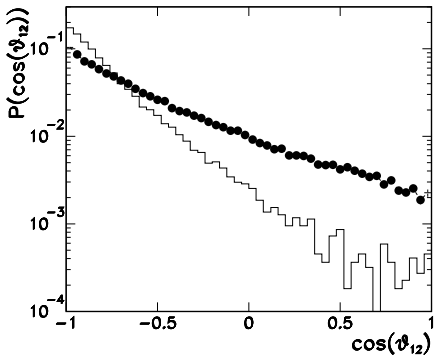

Figure 7.4: Experimental (dashed line) and Gemini (solid line) distribution of the cosinus of the angle formed by the centre of mass momenta of the two largest fragments, for events corresponding to at least three fragments ($Z \geq 3$). Both distributions have been normalized to unit area. For Gemini calculations the same events shown in Fig.7.3 (right panel) have been used.

However, the existing multifragmentation models[71, 72] very successful in reproducing detailately static as well as dynamic characteristics of fragment production for excited sources with excitation energies comparable to the present sample[73], treat nuclear clusters as liquid drops without any shell or pairing effect in their mass, nor contain the discrete particle unstable spectrum in all stages of the compound nucleus decay, the justification being that these models are supposed to be realistic only above the multifragmentation threshold, where structure effects are washed out. As a consequence, model distributions are smooth by construction and no insight about the presence/absence of odd-even effects can be gained out of these calculations.

In any case the failure of the standard evaporation picture at the threshold of multifragmentation suggests that the emission mechanism plays an important role for the light fragment yield, and/or that their decay is not governed by Q-values only. This is consistent with the experimental results from the correlation functions in the previous chapter, which showed that particle-unstable resonances play an important role in the light nuclei decay.

Conclusions

In this thesis we have reported on an experimental study of staggering in $^{32}S+^{58}Ni$ and $^{32}S+^{64}Ni$ collisions at 14.5 MeV/u, performed with the TANDEM-ALPI acceleration system at the Legnaro National Laboratory. The data collection was assured by the GARFIELD apparatus coupled to a high resolution annular detector for correlation measurements, the Ring Counter. Thanks to the important angular coverage and the low detection thresholds, we have been able to select two main classes of dissipative events for each reaction, corresponding to the statistical decay of an excited quasi-projectile, and of an incomplete fusion source respectively. Important odd-even effects are seen in the intermediate mass fragments yields as well as in the residue yields produced in the peripheral collisions, while these effects appear much less important in the central collision sample.

This different behavior indicates that several ingredients contribute to produce such effects, and there is no unique simple explanation. In particular, we have both experimental and theoretical indications that odd-even staggerings depend on the whole evaporation chain and not only on the energy balance of the last evaporation step.

As a consequence, the quantitative understanding of staggering can potentially give information on pairing and symmetry effects in the level density. To confirm (or infirm) this statement, a detailed comparison with statistical models will be needed. To this aim, an improvement of existing evaporation codes is important concerning the treatment of the discrete particle unstable spectrum. Our analysis shows that these states have to be included because they dominate the last evaporation step of light fragments. Another necessary improvement concerns the coupling between multifragmentation

and the subsequent evaporation of excited primary fragments, where a consistent and realistic treatment of the fragment energy functional should be employed, including pairing effects, realistic level densities and the discrete particle unstable spectrum in both stages of the compound nucleus decay.

On the experimental side, we have proposed in this work a model-independent technique to reconstruct the fragment yield at finite excitation energy corresponding to the last-but-one evaporation step. Because of different detection limitations, this reconstruction is however only partial. In order to allow with this technique to finally assess the origin of staggering in the different de-excitation mechanisms in a model-independent way, different improvements are in order.

A better granularity is needed to resolve the different resonance states in the correlation functions; experimental upgrades of the detection apparatus are in progress.

An increased statistics is needed to make a complete correlation function analysis for a data set where the source (Z, E^*) is reconstructed precisely; this in turn demands an impact parameter selection and good statistics for each impact parameter. In principle neutron detection would also be highly desirable to precisely trigger on the N/Z of the source. Alternatively this information can be deduced from the models if these latter are sufficiently constrained.

Since the branching ratios of the different decays for particle unstable levels of light fragments are typically known, a sufficiently complete measurement of a given isotope through correlation functions will allow to get also some quantitative information on the population of n-decaying levels. This will in the long run not only allow us to understand the origin of odd-even effects, but also to reconstruct primary fragment and thus access the thermodynamic information at the time of fragment formation, which is of particular interest in the multifragmentation regime.

Bibliography

[1] N. Bohr. Nature, 137:344, 1936.

[2] D. A. Bromley. Treatise on Heavy-Ion Science. Plenum Press, New York, 1984.

[3] R. H. Siemssen. Nucl. Phys. A, 400:245, 1983.

[4] G. Breit, E. Wigner, Capture of slow neutron, Phys. Rev. 49 (1936) 519.

[5] P. Langevin. C.R.Acad.Sci., 146:530, 1908.

[6] C.W. Gardiner. Handbook of Stochastic Methods. Springer, Berlin, 1990.

[7] R. Bass. Nuclear Reactions with Heavy Ions. Springer-Verlag, 1980.

[8] H. A. Bethe. Revs. Mod. Phys., 2:71, 1937.

[9] V. F.Weisskopf et al. Phys. Rev., 57:472 and 935, 1940.

[10] L.Wolfenstein et al. Phys. Rev., 82:690, 1951.

[11] W. Hauser et al. Phys. Rev., 87:366, 1952.

[12] D.Durand, E.Surand, B.Tamain. “Nuclear Dynamics in the nucleonic regime”, ed. IoP, London, 2001.

[13] Bohr A and Mottelson B 1975 Nuclear Structure vol II (New York: Benjamin).

[14] K.S. Krane. ”Introductory Nuclear Physics”, J. Wiley.

[15] F. Gramegna et al., Nucl. Instr. and Meth A389 (1997) 474-478.

[16] F. Gramegna, *The GARFIELD proposal*, Legnaro (1993), non pubblicato.

[17] A. Lanchais, *"GARFIELD: un apparato per misure di reazioni tra ioni pesanti ad energie intermedie"*, tesi di Laurea, Università degli Studi di Bologna, Corso di Laurea in Fisica.

[18] S. Albergo et al., Il Nuovo Cimento Vol. 89 A N.1 (1985).

[19] M. Chiari, A. Lanchais, F. Tonetto, L. Travaglini, Nucl. Instr. and Meth. A484: 111-117 (2002).

[20] A. Moroni et al., Nucl. Instr. and Meth A 556 (2006) 516-526.

[21] L. Bardelli et al., Nucl. Phys. A 746 (2004) 272c-276c.

[22] P.F.Mastinu, P.M.Milazzo, M.Bruno, M.D'Agostino, L.Manduci, Nucl. Instr. and Meth.A338(1994)419;

[23] G. Pasquali et al., Nucl. Instr. and Meth A 570 (2007) 126-132.

[24] M. D'Agostino, "Thermodynamical aspects in heavy ion reaction", LNL Internal Report (2004) pag.39
http : *//www.lnl.infn.it/* ~ *annrep/read_ar/*2004*/index_*2004*.html*

[25] Morelli et al. Nucl. Instr. and Meth. 620 (2010) 305.

[26] G. F. Knoll. Radiation detection and measurement. Wiley, 1989.

[27] L. Tassan-Got, arXiv:nucl-ex/0103004, Nucl. Phys. B (2002).

[28] N. LeNeindre,etal.,Nucl.Instr.and Meth.A490(2002)251.

[29] /http://indra.in2p3.fr/KaliVedaDoc.

[30] L. Bardelli, A ROOT-based data-monitor software for the GARFIELD experiment, LNL Annual Report (2009)

[31] F.Benrachi,etal.,Nucl.Instr.and Meth.A281(1989)137.

[32] R.Mankel,Pattern Recognition and Event Reconstruction in Particle Physics Experiments, arXiv:physics/0402039v1,2004.

[33] V. Avdeichikov et al., Nucl. Instr. and Meth A 501 (2003) 505-513.

[34] V. Avdeichikov et al., Nucl. Instr. and Meth A 466 (2001) 427-435.

[35] http://root.cern.ch/

[36] J. Cugnon and D. L'Ĥote, Nucl. Phys. A397 (1983) 519.

[37] N.Marie et al. Phys. Lett. B 391(1997) 15.

[38] M. D'Agostino *et al.*, Phys. Lett. 368 (1996) 259.

[39] L. Moretto and G. Wozniak, Annu. Rev. Nucl. Part. Sci. 43, 379 (1993); Proceedings of the XXVII International Workshop on Gross Properties on Nuclei and Nuclear Excitations, Hirshegg, 1999, edited by H. Feldmeier (GSI, Darmstadt, 1999).

[40] D. Lacroix *et al.* Phys. Rev. C69 (2004) 054604.

[41] W. Norenberg, Heavy-Ion Collisions (North-Holland, Amsterdam, 1980), Vol. 2.

[42] G. Casini et al., Phys. Rev. Lett. 71 (1993) 2567; J. Toke et. al., Phys. Rev. Lett. 75 (1995) 2920; S. Piantelli et. al., Phys. Rev. Lett. 88 (2002) 052701.

[43] M. V. Ricciardi et al., Nucl.Phys. A733 (2004) 299; arXiv-1007.0386v1.

[44] G. Cardella (Limiting Collaboration), private communication.

[45] L. B. Yang et al., Phys. Rev. C60 (1999) 041602 and references quoted there in.

[46] F.Gramegna *et al.* FIZIKA B 12 (2003) 1, 39.

[47] E.Geraci *et al.* Nucl. Phys. A732 (2004) 173

[48] M. B. Tsang, Eur.Phys.J.A30 (2006) 129-139 and Erratum-ibid.A32 (2007) 243.

[49] F. Saint-Laurent and the INDRA Collaboration, Nucl.Phys.A583(1995)481.

[50] Sl. Cavallaro *et al.*, Phys. Rev. C 57 (1998) 731.

[51] E. Bonnet, J.P. Wieleczko *et al.* arXiv:0808.2885, Int.J.Mod.Phys.E17:2359-2362,2009.

[52] R. Hanbury Brown and R. Q. Twiss, Philos. Mag. 45, 663 (1954); Nature (London) 177, 27 (1956); 178, 1046 (1956).

[53] S.E. Koonin, Phys. Lett. B70, 43 (1977).

[54] Z. Chen et al., Phys. Rev. C36, 2297 (1987).

[55] T. Murakami, T.K. Nayak, W.G. Lynch, K. Swartz, Z. Chen, D.J. Fields, C.K. Gelbke, Y.D. Kim, M.R. Maier, J. Pochodzalla, M.B. Tsang, H.M. Xu, F. Zhu, Nucl. Instr. Meth. Phys. Res. A275, 112 (1989).

[56] J. Pochodzalla *et al.*, Phys. Rev. C35 (1987) 1695.

[57] S.Pratt, T. Csrgo, J. Zimnyi, Phys. Rev. C42, 2646 (1990).

[58] D.H. Boal, C.K. Gelbke, B.K. Jennings, Rev. Mod. Phys. 62, 553 (1990).

[59] W.A. Friedman, Phys. Rev. C42, 667 (1990).

[60] W. P. Tan *et al.* Phys. Rev. C69 (2004) 061304(R).

[61] T. K. Nayak, T. Murakami, W. G. Lynch, K. Swartz, D. J. Fields, C. K. Gelbke, Y. D. Kim, J. Pochodzalla, M. B. Tsang, H. M. Xu, F. Zhu, and K. Kwiatkowski, Phys. Rev. C 45, 132 (1992).

[62] M. Assenard and the INDRA collaboration, SUBATECH 97-15, LPPC97-11.

[63] F.Gulminelli and D.Durand, Nucl.Phys.A 615 (1997) 117.

[64] //www.nndc.bnl.gov/nudat2/

[65] R. J. Charity, Phys. Rev. C 82 (2010) 014610.

[66] W. Hauser and H. Feshbach, Phys. Rev 87, 366 (1952).

[67] L.G. Moretto, Nucl. Phys. A247, 221 (1975).

[68] S. Cohen, F. Plasil, and W. J. Swiatecki, Ann. Phys. (NY) 82,557 (1974).

[69] A. J. Sierk, Phys. Rev. C 33, 2039 (1986).

[70] L.G. Moretto, Nucl. Phys. A247, 221 (1975).

[71] J. P. Bondorf, A. S. Botvina, A. S. Iljinov, I. N. Mishustin, K. Sneppen, Phys. Rep. 257 (1995) 133.

[72] Al. H. Raduta and Ad. R. Raduta, Phys. Rev. C55 (1997) 1344; *ibid.* Phys. Rev. C65 (2002) 054610.

[73] M.D'Agostino *et al.*, Nucl.Phys.A 724 (2003) 455.